

Two-Dimensional Potential Energy Surfaces of
Binding CO/NO with Coinage Metals

Inaugural-Dissertation

to obtain the academic degree

Doctor Rerum Naturalium (Dr. rer. nat.)

submitted to

the Department of Biology, Chemistry and Pharmacy of

Freie Universität Berlin

by

Yasmeen Jamal Qawasmeh

from

Hebron, Palestine

2020

This work was prepared under supervision of
Prof. Dr. Beate Paulus and Prof. Dr. Ludger Wöste
(Freie Universität Berlin)
from April 2014 until August 2019.

1. Referee: Prof. Dr. Beate Paulus.
2. Referee: Prof. Dr. Ludger Wöste.

Date of the defence: 05.05.2020

Selbstständigkeitserklärung

Hiermit erkläre ich, dass ich die vorliegende Arbeit selbständig und nur unter Verwendung der angegebenen Literatur und Hilfsmittel angefertigt habe. Zudem versichere ich, dass diese Arbeit in keinem früheren Promotionsverfahren eingereicht und dort angenommen oder für ungenügend befunden wurde.

Berlin, 26. March 2020

Dedication

To my son
Kareem Najar.

To my husband
Tariq Najar.

To my family.

Acknowledgements

Foremost, I would like to express my appreciation and gratitude to my supervisor, Prof.Dr. Beate Paulus for offering me the opportunity to pursue my PhD in her group. I would also like to express my gratitude to Prof. Dr.Ludger Wöste, who kindly accepted the task of being the second referee.

I'm very grateful for the financial and scientific support by the Deutscher Akademischer Austausch Dienst (DAAD) and Dahlem Research School (DRS). I want to thank the technical support of the Zentral Einrichtung für Daten Verarbeitung (ZEDAT) for providing fast and uncomplicated technical support as well as the high performance computing resources.

I would like to thank my dearest friends Zeinab Kaawar, Maysoon Saleh and Ghada Hussein. They offered me valuable advices, patiently listened to my problems and encouraged me when I was depressed. Together, we have shared many unforgettable moments, in and outside the university.

Most of all, I am very grateful to my small family: to my husband Tariq who has always been and will always be an important part of my life. My thesis could not have been successful without his support and understanding during my whole doctoral trip. To my dear son, Kareem, who bear long days stays away from me, I say: "You are the most precious gift God gave me."

Last but not the least, it is hard to express in words my gratitude towards my parents. They were and still are the source of my success in life. The best way to thank them and repay their unconditional love and trust is to keep doing my best in all I do.

Abstract

Two-dimensional potential energy surfaces of charged and neutral MXO (X: C, N and M: Au, Ag, Cu) and neutral M_2XO complexes were calculated. Our results are based on the CCSD(T)/AVTZ level of theory with effective core potentials for the transition metals. The calculations show that the PES of MXO^+ have two minima, one at the linear X-down, the other at linear O-down structure, while the neutral complexes have only one minimum, X-down, but in a triangular shape with an angle depending on the metal atom. The negative charged complexes have a dispersive minimum when the metal anion nearly perpendicular to the geometrical center of the XO molecule and distance greater than 3.5 Å .

Additionally we have calculated the interaction energy of M_2XO complexes with different orientations and found that the linear X-down complexes are the most stable orientation. Also the binding of the CO molecule to the diatomic M_2 is stronger than to the M atom. On the contrary, the binding of the NO molecule to the diatomic M_2 is weaker than the M atom. The strength of the binding energies are ranked based on the type of the metal, for all type of charge and type of X atoms, as $Au > Cu > Ag$. About the isoelectric pairs: MCO, MNO^+ and MCO^- , MNO, there is no correlation between the number of electrons and the shape of the PES.

The counterpoise-corrected interaction energy increases as the charge of the complex increases. The positive charged complexes have blue shift in X-O stretching frequency while the neutral and negative charged complexes have red shift.

With these highly accurate PESs, it is possible to fit force fields for the system under investigation and to perform an anharmonic vibrational analysis.

Kurzzusammenfassung

Zweidimensionale Potentialenergieflächen (PES) von geladenen und neutralen MXO (X: C, N und M: Au, Ag, Cu) und neutrale M_2XO -Komplexe wurden berechnet. Unsere Ergebnisse basieren auf auf CCSD(T)/AVTZ Rechnungen mit effektiven Kernpotentialen für die Übergangsmetalle. Die Berechnungen zeigen, dass die PES von MXO^+ zwei Minima haben, eines bei der linearen MXO-Struktur, das andere bei der linearen MOX-Struktur, während die neutralen Komplexe nur ein Minimum haben, eine dreieckige MXO-Struktur, wobei der Winkel vom Metallatom abhängt. Die negativ geladenen Komplexe weisen ein dispersives Minimum auf, wenn das Metall-Anion fast senkrecht zum geometrischen Zentrum des XO-Moleküls steht und der Abstand größer als 3,5 Å ist.

Zusätzlich haben wir die Wechselwirkungsenergie von M_2XO -Komplexen mit verschiedenen Orientierungen berechnet und herausgefunden, dass die linearen X-down-Komplexe die stabilste Modifikation sind. Darüber hinaus ist die Bindung des CO-Moleküls an das zweiatomige M_2 stärker als an das M-Atom. Im Gegensatz dazu, ist die Bindung des NO-Moleküls an das zweiatomige M_2 schwächer als an das M-Atom. Unabhängig von Ladung und Element X steigt die Bindungsenergie von Ag über Cu zu Au. Zu den isoelektrischen Paaren MCO und MNO^+ sowie MCO^- and MNO wurde keine Korrelation zwischen der Anzahl an Elektronen und der Form der PES gefunden. Die counterpoise-korrigierte Wechselwirkungsenergie nimmt mit der Ladung des Komplexes zu. Die positiv geladenen Komplexe weisen eine Blauverschiebung der X-O-Streckfrequenz auf, während die neutral und negativ geladenen Komplexe eine Rotverschiebung zeigen.

Mit diesen hochgenauen PES ist es möglich, Kraftfelder für das zu untersuchende System zu optimieren und zum Beispiel eine anharmonische Schwingungsanalyse durchzuführen.

Contents

1	Introduction	1
2	Theory and methodology	9
2.1	Born-Oppenheimer Approximation	10
2.2	Hartree-Fock Approximation	11
2.3	Post-Hartree-Fock methods	15
2.3.1	Configuration Interaction	16
2.3.2	Perturbation Theory	18
2.3.2.1	Møller-Plesset Perturbation Theory	21
2.3.3	Coupled-Cluster Theory	23
2.4	Computational details	34
2.4.1	Basis set superposition error and Counterpoise Correction	35
3	Electronic properties of monomers	37
3.1	Carbon monoxide	38
3.2	Nitrogen monoxide	40
3.3	Coinage metals atom	42
3.4	Coinage metal dimer	44
4	Two dimensions potential energy surfaces of coinage metals carbonyl complexes	47
4.1	2D-PESs of $MCO^{0,\pm}$	49
4.2	Electronic structure of coinage metals carbonyl	62
4.3	Potential energy surface of M_2CO	66
5	Two dimensions potential energy surfaces of coinage metals nitrosyl complexes	71
5.1	2D-PESs of MNO complexes	72
5.2	2D-PESs of MNO^+ complexes	86
5.3	2D-PESs of MNO^- complex	98
5.4	Potential energy surface of M_2NO	107
6	Conclusion	111
	Appendix	117

List of Figures

3.1.1	Energy level diagram for canonical valence molecular orbitals of carbon monoxide molecule ($^1\Sigma^+$) using RHF/AVTZ. The atomic orbitals of carbon and oxygen are calculated with CASSCF(4/4) and (6/4)/AVTZ, respectively.	39
3.1.2	The highest occupied molecular orbital (HOMO) of CO (3σ). The carbon atom on the left and the oxygen atom on the right, the isocontour is 0.025. The contribution of s and p atomic orbitals are: HOMO= $-0.62C_{2s} + 0.71C_{px} + 0.06O_{2s} - 0.38O_{px}$.	39
3.1.3	The highest occupied molecular orbital (HOMO) of NO ($2\pi^*$). The nitrogen atom on the left and the oxygen atom on the right, the isocontour is 0.025. The contribution of p atomic orbitals are: HOMO= $+0.88N_{px} - 0.69O_{px}$.	39
3.2.1	Energy level diagram for natural valence molecular orbitals of nitrogen monoxide molecule ($^2\Pi$) using CASSCF(5/4)/AVTZ.	41
3.4.1	The canonical valence molecular orbital diagram of $M_2(^1\Sigma)$ with M: Au, Ag, Cu. The shell number is represented by n = 5, 4, 3 for Au, Ag, Cu	46
4.0.1	M-CO geometry selected for the 2D-PES, the distance and the angle between the coinage metal atom and the CO center is represented by (d) and (α), respectively. At $\alpha = 90^\circ$ the complex has a linear geometry MCO and at $\alpha = -90^\circ$ the complex has a linear geometry MOC.	48
4.1.1	Counterpoise corrected binding energy surface of $Au(^2S) + CO(^1\Sigma^+) \rightarrow AuCO(^2A')$ as a function of the distance and the angle between Au atom and CO center as described in Fig. 4.0.1 using UCCSD(T)/Au=ECP60MDF-AVTZ, C=AVTZ, O=AVTZ. The dots represent the binding energy calculated at different geometries.	50
4.1.2	Counterpoise corrected binding energy surface of $Ag(^2S) + CO(^1\Sigma^+) \rightarrow AgCO(^2A')$ as a function of the distance and the angle between Ag atom and CO center as described in Fig. 4.0.1 using UCCSD(T)/Ag=ECP28MDF-AVTZ, C=AVTZ, O=AVTZ. The dots represent the binding energy calculated at different geometries.	51
4.1.3	Counterpoise corrected binding energy surface of $Cu(^2S) + CO(^1\Sigma^+) \rightarrow CuCO(^2A')$ as a function of the distance and the angle between Cu atom and CO center as described in Fig. 4.0.1 using UCCSD(T)/Cu=ECP10MDF-AVTZ, C=AVTZ, O=AVTZ. The dots represent the binding energy calculated at different geometries.	52

- 4.1.4 Counterpoise corrected binding energy surface of $\text{Au}^+(^1\text{S}) + \text{CO}(^1\Sigma^+) \longrightarrow \text{AuCO}^+(^1\text{A}')$ as a function of the distance and the angle between Au^+ ion and CO center as described in Fig. 4.0.1 using UCCSD(T)/Au=ECP60MDF-AVTZ, C=AVTZ, O=AVTZ. The dots represent the binding energy calculated at different geometries. 53
- 4.1.5 Counterpoise corrected binding energy surface of $\text{Ag}^+(^1\text{S}) + \text{CO}(^1\Sigma^+) \longrightarrow \text{AgCO}^+(^1\text{A}')$ as a function of the distance and the angle between Ag^+ ion and CO center as described in Fig. 4.0.1 using UCCSD(T)/Ag=ECP28MDF-AVTZ, C=AVTZ, O=AVTZ. The dots represent the binding energy calculated at different geometries. 54
- 4.1.6 Counterpoise corrected binding energy surface of $\text{Cu}^+(^1\text{S}) + \text{CO}(^1\Sigma^+) \longrightarrow \text{CuCO}^+(^1\text{A}')$ as a function of the distance and the angle between Cu^+ ion and CO center as described in Fig. 4.0.1 using UCCSD(T)/Cu=ECP10MDF-AVTZ, C=AVTZ, O=AVTZ. The dots represent the binding energy calculated at different geometries. 55
- 4.1.7 Counterpoise corrected binding energy surface of $\text{Au}^-(^1\text{S}) + \text{CO}(^1\Sigma^+) \longrightarrow \text{AuCO}^-(^1\text{A}')$ as a function of the distance and the angle between Au^- ion and CO center as described in Fig. 4.0.1 using UCCSD(T)/Au=ECP60MDF-AVTZ, C=AVTZ, O=AVTZ. The dots represent the binding energy calculated at different geometries. 56
- 4.1.8 Counterpoise corrected binding energy surface of $\text{Ag}^-(^1\text{S}) + \text{CO}(^1\Sigma^+) \longrightarrow \text{AgCO}^-(^1\text{A}')$ as a function of the distance and the angle between Ag^- ion and CO center as described in Fig. 4.0.1 using UCCSD(T)/Ag=ECP28MDF-AVTZ, C=AVTZ, O=AVTZ. The dots represent the binding energy calculated at different geometries. 57
- 4.1.9 Counterpoise corrected binding energy surface of $\text{Cu}^-(^1\text{S}) + \text{CO}(^1\Sigma^+) \longrightarrow \text{CuCO}^-(^1\text{A}')$ as a function of the distance and the angle between Cu^- ion and CO center as described in Fig. 4.0.1 using UCCSD(T)/Cu=ECP10MDF-AVTZ, C=AVTZ, O=AVTZ. The dots represent the binding energy calculated at different geometries. 58
- 4.2.1 Energy level diagram for canonical valence molecular orbitals of AuCO complex ($^2\text{A}'$) using RHF/AVTZ. The CO molecular orbital have the same labels as in Fig. 3.1.1. The molecular orbital occupation depending on C_s point group is: $(1a')^2(2a')^2(1a'')^2(3a')^2(2a'')^2(4a')^2(3a'')^2(5a')^2(6a')^2(7a')^1$. The highest occupied molecular orbital (HOMO) consists mainly from the 6s gold atomic orbital (The gold atom on the right and the CO unit on the left, the isocontour is 0.025). 64
- 4.3.1 Counterpoise corrected binding energy of $\text{M}_2(^1\Sigma) + \text{CO}(^1\Sigma^+) \longrightarrow \text{M}_2 - \text{CO}$, with M: Au, Ag, Cu as a function of the distance between C atom or O atom and coinage metals dimer as described in the Tab.4.3.1 using UCCSD(T)/ECP(10,28,60)MDF-AVTZ, C=AVTZ, O=AVTZ. The subfigures on the right are zoom in for M-C distance. 68
- 4.3.2 Counterpoise corrected binding energy surface of Au_2CO as a function of the distance between Au atom and CO center and the angle as described in the geometry at the upper part of the figure (when $a = 0^\circ$ the geometry is linear Au_2CO , $a = 90^\circ$ it is CO hat, $a = 180^\circ$ the geometry is linear Au_2OC) using UCCSD(T)/Au=ECP60MDF-AVTZ, C=AVTZ, O=AVTZ. The dots represent the binding energy calculated at different geometries. 70

5.1.1 Counterpoise corrected binding energy surface of $\text{Au}(^2\text{S}) + \text{NO}(^2\Pi) \rightarrow \text{AuNO}(^1\text{A}')$ as a function of the angle and the distance between Au atom and NO center as described in Fig. 4.0.1 using UCCSD(T)/Au=ECP60MDF-AVTZ, N=AVTZ, O=AVTZ. The dots represent the binding energy calculated at different geometries.	73
5.1.2 Counterpoise corrected binding energy surface of $\text{Au}(^2\text{S}) + \text{NO}(^2\Pi) \rightarrow \text{AuNO}(^3\text{A}')$ as a function of the angle and the distance between Au atom and NO center as described in Fig. 4.0.1 using UCCSD(T)/Au=ECP60MDF-AVTZ, N=AVTZ, O=AVTZ. The dots represent the binding energy calculated at different geometries.	74
5.1.3 Counterpoise corrected binding energy surface of $\text{Au}(^2\text{S}) + \text{NO}(^2\Pi) \rightarrow \text{AuNO}(^3\text{A}'')$ as a function of the angle and the distance between Au atom and NO center as described in Fig. 4.0.1 using UCCSD(T)/Au=ECP60MDF-AVTZ, N=AVTZ, O=AVTZ. The dots represent the binding energy calculated at different geometries.	75
5.1.4 Counterpoise corrected binding energy surface of $\text{Ag}(^2\text{S}) + \text{NO}(^2\Pi) \rightarrow \text{AgNO}(^1\text{A}')$ as a function of the angle and the distance between Ag atom and NO center as described in Fig. 4.0.1 using UCCSD(T)/Ag=ECP28MDF-AVTZ, N=AVTZ, O=AVTZ. The dots represent the binding energy calculated at different geometries.	76
5.1.5 Counterpoise corrected binding energy surface of $\text{Ag}(^2\text{S}) + \text{NO}(^2\Pi) \rightarrow \text{AgNO}(^3\text{A}')$ as a function of the angle and the distance between Ag atom and NO center as described in Fig. 4.0.1 using UCCSD(T)/Ag=ECP28MDF-AVTZ, N=AVTZ, O=AVTZ. The dots represent the binding energy calculated at different geometries.	77
5.1.6 Counterpoise corrected binding energy surface of $\text{Ag}(^2\text{S}) + \text{NO}(^2\Pi) \rightarrow \text{AgNO}(^3\text{A}'')$ as a function of the angle and the distance between Ag atom and NO center as described in Fig. 4.0.1 using UCCSD(T)/Ag=ECP28MDF-AVTZ, N=AVTZ, O=AVTZ. The dots represent the binding energy calculated at different geometries.	78
5.1.7 Counterpoise corrected binding energy surface of $\text{Cu}(^2\text{S}) + \text{NO}(^2\Pi) \rightarrow \text{CuNO}(^1\text{A}')$ as a function of the angle and the distance between Cu atom and NO center as described in Fig. 4.0.1 using UCCSD(T)/Cu=ECP10MDF-AVTZ, N=AVTZ, O=AVTZ. The dots represent the binding energy calculated at different geometries.	79
5.1.8 Counterpoise corrected dissociation energy surface of $\text{Cu}(^3\text{P}) + \text{NO}(^2\Pi) \rightarrow \text{CuNO}(^3\text{A}')$ as a function of the distance between Cu atom and NO center and the angle as described in Fig. 4.0.1 using UCCSD(T)/Cu=ECP10MDF-AVTZ, N=AVTZ, O=AVTZ. The dots represent the dissociation energy calculated at different geometries.	80
5.1.9 Counterpoise corrected binding energy surface of $\text{Cu}(^2\text{S}) + \text{NO}(^2\Pi) \rightarrow \text{CuNO}(^3\text{A}'')$ as a function of the angle and the distance between Cu atom and NO center as described in Fig. 4.0.1 using UCCSD(T)/Cu=ECP10MDF-AVTZ, N=AVTZ, O=AVTZ. The dots represent the binding energy calculated at different geometries.	81

- 5.1.1 Energy level diagram for canonical molecular orbitals of AuNO complex ($^1A'$) using RHF/AVTZ. The NO molecular orbitals have the same labels as in Fig. 3.2.1. The molecular orbital occupation depending on C_s point group is: $(1a')^2(1a'')^2(2a')^2(2a'')^2(3a')^2(3a'')^2(4a')^2(5a')^2(6a')^2$. The molecular orbital diagram of $^3A''$ state has two unpaired electrons instead of two electrons in $2\pi_x^* + 6s$ orbital, see the red colored orbitals and the pictures, they are the HOMO and HOMO-1 of $^3A''$. Hence, the molecular orbitals occupation of $^3A''$: $(1a')^2(1a'')^2(2a')^2(2a'')^2(3a')^2(3a'')^2(4a')^2(5a')^2(6a'')^1(6a')^1$. (the gold atom on the right and the NO molecule on the left, the isocontour is 0.025.) 85
- 5.2.1 Counterpoise corrected binding energy surface of $Au^+(^1S) + NO(^2\Pi) \rightarrow AuNO^+(^2A')$ as a function of the angle and the distance between Au atom and NO center as described Fig. 4.0.1 using UCCSD(T)/Au=ECP60DF-AVTZ, N=AVTZ, O=AVTZ. The dots represent the binding energy calculated at different geometries. 88
- 5.2.2 Counterpoise corrected binding energy surface of $Au^+(^1S) + NO(^2\Pi) \rightarrow AuNO^+(^2A'')$ as a function of the angle and the distance between Au atom and NO center as described in Fig. 4.0.1 using UCCSD(T)/Au=ECP60DF-AVTZ, N=AVTZ, O=AVTZ. The dots represent the binding energy calculated at different geometries. 89
- 5.2.3 Counterpoise corrected binding energy surface of $Ag^+(^1S) + NO(^2\Pi) \rightarrow AgNO^+(^2A')$ as a function of the angle and the distance between Ag atom and NO center as described in Fig. 4.0.1 using UCCSD(T)/Ag=ECP28MDF-AVTZ, N=AVTZ, O=AVTZ. The dots represent the binding energy calculated at different geometries. 90
- 5.2.4 Counterpoise corrected binding energy surface of $Ag^+(^1S) + NO(^2\Pi) \rightarrow AgNO^+(^2A'')$ as a function of the angle and the distance between Ag atom and NO center as described in Fig. 4.0.1 using UCCSD(T)/Ag=ECP28MDF-AVTZ, N=AVTZ, O=AVTZ. The dots represent the binding energy calculated at different geometries. 91
- 5.2.5 Counterpoise corrected binding energy surface of $Cu^+(^1S) + NO(^2\Pi) \rightarrow CuNO^+(^2A')$ as a function of the distance between Cu atom and NO center and angle as described in Fig. 4.0.1 using UCCSD(T)/Cu=ECP10MDF-AVTZ, N=AVTZ, O=AVTZ. The dots represent the binding energy calculated at different geometries. 92
- 5.2.6 Counterpoise corrected binding energy surface of $Cu^+(^1S) + NO(^2\Pi) \rightarrow CuNO^+(^2A'')$ as a function of the distance between Cu atom and NO center and angle as described in Fig. 4.0.1 using UCCSD(T)/Cu=ECP10MDF-AVTZ, N=AVTZ, O=AVTZ. The dots represent the binding energy calculated at different geometries. 93
- 5.3.1 Counterpoise corrected binding energy surface of $Au^-(^1S) + NO(^2\Pi) \rightarrow AuNO^-(^2A')$ as a function of the angle and the distance between Au atom and NO center as described in Fig. 4.0.1 using UCCSD(T)/Au=ECP60DF-AVTZ, N=AVTZ, O=AVTZ. The dots represent the binding energy calculated at different geometries. 99

5.3.2 Counterpoise corrected binding energy surface of $\text{Au}^{-}(^1\text{S}) + \text{NO}(^2\Pi) \longrightarrow \text{AuNO}^{-}(^2\text{A}'')$ as a function of the angle and the distance between Au atom and NO center as described in Fig. 4.0.1 using UCCSD(T)/Au=ECP60DF-AVTZ, N=AVTZ, O=AVTZ. The dots represent the binding energy calculated at different geometries.	100
5.3.3 Counterpoise corrected binding energy surface of $\text{Ag}^{-}(^1\text{S}) + \text{NO}(^2\Pi) \longrightarrow \text{AgNO}^{-}(^2\text{A}')$ as a function of the angle and the distance between Ag atom and NO center as described in Fig. 4.0.1 using UCCSD(T)/Ag=ECP28MDF-AVTZ, N=AVTZ, O=AVTZ. The dots represent the binding energy calculated at different geometries.	101
5.3.4 Counterpoise corrected binding energy surface of $\text{Ag}^{-}(^1\text{S}) + \text{NO}(^2\Pi) \longrightarrow \text{AgNO}^{-}(^2\text{A}'')$ as a function of the angle and the distance between Ag atom and NO center as described in Fig. 4.0.1 using UCCSD(T)/Ag=ECP28MDF-AVTZ, N=AVTZ, O=AVTZ. The dots represent the binding energy calculated at different geometries.	102
5.3.5 Counterpoise corrected binding energy surface of $\text{Cu}^{-}(^1\text{S}) + \text{NO}(^2\Pi) \longrightarrow \text{CuNO}^{-}(^2\text{A}')$ as a function of the distance between Cu atom and NO center and angle as described in Fig. 4.0.1 using UCCSD(T)/Cu=ECP10MDF-AVTZ, N=AVTZ, O=AVTZ. The dots represent the binding energy calculated at different geometries.	103
5.3.6 Counterpoise corrected binding energy surface of $\text{Cu}^{-}(^1\text{S}) + \text{NO}(^2\Pi) \longrightarrow \text{CuNO}^{-}(^2\text{A}'')$ as a function of the distance between Cu atom and NO center and angle as described in Fig. 4.0.1 using UCCSD(T)/Cu=ECP10MDF-AVTZ, N=AVTZ, O=AVTZ. The dots represent the binding energy calculated at different geometries.	104
5.4.1 Counterpoise corrected binding energy of $\text{M}_2(^1\Sigma) + \text{NO}(^2\Pi) \longrightarrow \text{M}_2 - \text{NO}$, with M: Au, Ag, Cu as a function of the distance between N atom or O atom and coinage metals dimer as described in the Fig. 4.3.1 using UCCSD(T)/ECP(10,28,60)MDF-AVTZ, N=AVTZ, O=AVTZ. The subfigures on the right are zoom in for M-N distance.	108
5.4.2 2-dimensions Counterpoise corrected binding energy surface of Au_2NO as a function of the distance between Au atom and NO center and the angle as described in Fig. 4.3.2 using UCCSD(T)/Au=ECP60MDF-AVTZ, N=AVTZ, O=AVTZ. The dots represent the binding energy calculated at different geometries.	110

List of Tables

3.3.1	The ground and the excited states of neutral atom, cation and anion of coinage metals and the their corresponding excitation energy calculated by UCCSD(T)/ECP(10,28,60)MDF-AVTZ. The experimental values correspond to the mean values of total angular momentum (J) over all spin-orbital components of the state [211].	42
3.3.2	Ionization potential (IP) and electron affinity (EA) of copper, silver, gold atoms and CO, NO molecules calculated by CCSD(T)/ECP _n MDF-AVTZ, where n being the number of core electrons that are replaced by a pseudopotential, 10 for Cu, 28 for Ag and 60 for Au.	44
3.4.1	The bond length of copper, silver and gold dimer calculated by CCSD(T)/ECP _n MDF-AVTZ, where n is the number of core electrons which are replaced by pseudopotential, 10 for Cu, 28 for Ag and 60 for Au.	45
3.4.2	The energy of s and d atomic orbitals for copper, silver and gold atoms and the HOMO and the LUMO of their dimers calculated by RHF/ECP _n MDF-AVTZ, where n is the number of core electrons which are replaced by pseudopotential, 10 for Cu, 28 for Ag and 60 for Au.	45
4.2.1	The optimized bond parameters of MCO ^{0,±} and MOC ⁺ with M: Au, Ag, Cu. The r _{M-O} and ∠MNO are different than the angle (α) and the distance (d) in Fig. 4.0.1. The basis set superposition error (BSSE), zero point energy (ZPE) and the counterpoise ZPE corrected binding energy using UCCSD(T)/ECP(60,28,10)MDF-AVTZ are given.	62
4.2.2	The vibrational frequencies of MCO ^{0,±} and MOC ⁺ with M: Au, Ag, Cu. The CO shift is calculated as a difference of C-O stretching frequency and the free CO frequency (2143.3 cm ⁻¹) using UCCSD(T)/ECP(60,28,10)MDF-AVTZ.	63
4.3.1	Different configurations of M ₂ – CO and M ₂ – OC, where M: Au, Ag, Cu.	66
4.3.2	Counterpoise corrected binding energy of M ₂ – CO and M ₂ – OC, where M: Au, Ag and Cu for different configurations and the corresponding distance between the metal and carbon or oxygen atoms based on the geometry described in Tab.4.3.1 calculated by UCCSD(T)/ECP(60, 28, 10)MDF-AVTZ. The CO-hat and parallel configurations are the same for M ₂ – CO and M ₂ – OC.	69

5.1.1	The optimized bond parameters of MNO with M: Au, Ag, Cu. The r_{M-N} and $\angle MNO$ are different than the angle (α) and the distance (d) in Fig. 4.0.1. The basis set superposition error(BSSE), zero point energy (ZPE) and the counterpoise ZPE corrected binding energy using UCCSD(T)/ECP(60,28,10)MDF-AVTZ.	82
5.1.2	The vibrational frequencies of MNO with M: Au, Ag, Cu. The NO shift is calculated as a difference of N-O stretching frequency and the free NO frequency (1889.1 cm^{-1}) using UCCSD(T)/ECP(60,28,10)MDF-AVTZ. .	83
5.2.1	The optimized parameters of MNO^+ and MON^+ with M: Au, Ag, Cu. The BSSE and ZPE errors. The counterpoise and ZPE corrected binding energy using UCCSD(T)/ECP(60,28,10)MDF-AVTZ, N=AVTZ, O=AVTZ. . . .	94
5.2.2	The vibrational frequencies of MNO^+ and MON^+ with M: Au, Ag, Cu. The NO shift is calculated as a difference of N-O stretching frequency and the free NO frequency (1889.1 cm^{-1}) using UCCSD(T)/ECP(60,28,10)MDF-AVTZ.	95
5.3.1	The optimized bond parameters of MNO^- with M: Au, Ag, Cu. The r_{M-N} and $\angle MNO$ are different than the angle (α) and the distance (d) in Fig. 4.0.1. The basis set superposition error(BSSE), zero point energy (ZPE) and the counterpoise ZPE corrected binding energy using UCCSD(T)/ECP(60,28,10)MDF-AVTZ.	105
5.3.2	The vibrational frequencies of MNO^- with M: Au, Ag, Cu. The NO shift is calculated as a difference of N-O stretching frequency and the free NO frequency (1889.1 cm^{-1}) using UCCSD(T)/ECP(60,28,10)MDF-AVTZ. .	105
5.4.1	Counterpoise corrected binding energy of $M_2 - NO$ and $M_2 - ON$, where M: Au, Ag and Cu for different configurations and the corresponding distance between the metal and nitrogen or oxygen atoms based on the geometry described in Tab. 4.3.1 calculated by UCCSD(T)/ECP(60, 28, 10)MDF-AVTZ. The CO-hat and parallel configurations are the same for $M_2 - NO$ and $M_2 - ON$	109
6.0.1	Mulliken population analysis for the neutral and charged coinage metal monocarbonyl $MCO^{\pm,0}$ complexes using HF/Au=ECP60MDF-AVTZ, C=AVTZ, O=AVTZ.	118
6.0.2	Mulliken population analysis for the neutral and positive charged coinage metal mononitrosyl MNO, MNO^+ complexes using HF/Au=ECP60MDF-AVTZ, N=AVTZ, O=AVTZ.	119
6.0.3	Mulliken population analysis for the negative charged coinage metal mononitrosyl MNO^- complexes using HF/Au=ECP60MDF-AVTZ, N=AVTZ, O=AVTZ.	120

Introduction

Carbon monoxide (CO) and nitrogen monoxide (NO) are toxic and harmful air pollutants. They affect passively on human beings and vegetation and indirectly increase global warming. They are mainly produced from vehicles exhaust and because of the significantly increasing number of vehicles on the roads, their concentrations reach an alarming level especially in large cities. Thus, to control vehicles exhaust pollution, it is recommended to use pollution-reducing units called catalytic converters [1, 2].

The catalytic converter is a tool that converts the harmful pollutants such as, CO, NO and unburned hydrocarbons (HC) into less harmful emissions like CO₂ and N₂ before they leave the car's exhaust system. It consists out of a large metal box that have active catalytic material inside and two pipes coming out of it. The first pipe is connected to the car's engine and brings in hot, polluted fumes that are produced from fuel burns. The second pipe is connected to the tailpipe (exhaust). When the gases from the engine fumes blow over the catalyst, chemical reactions take place on its surface, breaking apart the pollutant gases and converting them into other gases that are safe enough to blow harmlessly out into the air [3–8]. The effectivity of the catalytic converter depends mainly on the type of the catalyst [9–11].

The catalyst is a substances that accelerate the chemical reactions without appearing in the end products [12, 13]. Therefore, the chemical reactions occur faster in the presence of a catalyst since the catalyst provides an alternative reaction pathway with a lower activation energy than the non-catalyzed mechanism. Catalysts are used in multidisciplinary science and have extensive applications in the food [14–17], pharmaceutical [18–23], and crude oil

industries[24–26] and reducing water and air pollution [27–34].

Catalytic reactions are divided into two main categories, homogeneous and heterogeneous. In a homogeneous reaction, the catalyst is in the same phase as the reactants, whereas in a heterogeneous reaction, the catalyst is in a different phase from the reactants. Traditionally, the homogeneous catalysts are very selective but not very active and not very stable, while heterogeneous catalysts are active and stable at high temperatures but not very selective [35, 36].

What happens inside the catalytic converter is a heterogeneous catalytic reactions. In general, there are three different chemical reactions going on at the same time which are catalyzed by two different catalysts. The first catalyst tackles CO and the unburned hydrocarbons using chemical reaction called oxidation (adding an oxygen). It converts CO into CO₂ and the unburned hydrocarbons into CO₂ and water. The second catalyst tackles the NO by an opposite chemical process called reduction (removing oxygen), it breaks up the NO into nitrogen and oxygen atoms. After two oxidation and one reduction reactions, the exhaust is ideally a steam of nitrogen molecules (N₂), oxygen molecules (O₂), carbon dioxide (CO₂) and water (H₂O).

The promising catalysts for these reactions are nanosized materials. There are many studies concerned about catalyzing CO oxidation and NO reduction by various types of nanocatalysts consisting from base metals (Cu, Mn, Cr, Ni, Fe)[27, 37–44], noble metals (Pt, Pd, Rh, Au, Ag)[45–63] and metal oxides (Cu₂O, ZnO, CeO₂)[40, 64–67]. The present study investigates the catalytic role of the coinage metals atom (Au, Ag, Cu) in the CO oxidation and the NO reduction.

A number of experimental investigations and first-principles calculations have been performed to study the interaction of gold, silver and copper with small molecules CO, NO and O₂ by studying the adsorption of gas molecules either on free and supported metal surfaces or free and supported nanocluster. Kim et al [68] demonstrated that two types of low-coordinated sites (steps and kinks) dominate the adsorption of CO at temperatures above 100 K for the whole range of gold substrates ranging from stepped single-crystal surfaces to small supported Au particles. In addition to the experiments, they carried out theoretical studies of CO adsorption on Au(332) surface using DFT method, the calculations show that CO desorption states above 100 K may be located at step-edges but

not on terrace sites. Furthermore, Kim et al [69] investigate CO adsorption and reaction on Au(211) stepped single-crystal surfaces, they found that CO was weakly adsorbed but was more strongly bound at step sites than at terrace sites.

Haruta and coworkers described the CO oxidation over supported gold clusters at normal and low temperatures in a series of articles [70–78], they found that the catalytic performances of gold depend on the supports, the size of the cluster, and the preparation methods [79]. For instance, gold supported on metal oxides of 3d transition metals of group VIII (Fe, Co, Ni) are much more active for CO oxidation other than on SiO₂ and Al₂O₃ [80]. In addition, CO oxidation reaches its maximum on Au/TiO₂ when the diameter of Au islands is 3.5 nm (corresponding to a few hundred atoms, approximately) [81], while on the MgO (001) surface it is observed in the 8–20 atoms size range [82–84].

Moreover, other scientists have investigated the reactivity of free gold clusters, Au_n, and its dependence on both the charge state and the size of the clusters [85–88]. For instance, Cox et al. [85] observed that small gold cations ($n < 15$) are reactive towards H₂ and CH₄, whereas only even n anionic clusters are reactive to O₂. Lee and Ervin investigated the reactions of CO and O₂ with small anionic clusters [86]. They observed that CO molecules are more reactive toward larger clusters ($n > 4$) and there is no even/odd alternation as for O₂. In addition, Wallace and Whetten studied the pressure-dependent adsorption activity of the CO and O₂ molecules on Au_n⁻ ($n = 4 - 19$). They found that the adsorption activity of CO or O₂ is enhanced when the cluster already possesses the other molecule (cooperative coadsorption) and the coadsorption of CO and O₂ on Au₆⁻ leads to a loss of CO₂ molecule.

Simultaneously to the above-mentioned experiments, a number of theoretical studies of CO interaction with free and supported gold clusters were investigated using density functional theory (DFT) [78, 83, 89–95]. For example, Sanchez et al [83] studied the reactivity of gold clusters supported on magnesia (Au/MgO) and they found Au₈ cluster is the smallest catalytically active size for CO oxidation. In addition, Senapati et al [89] calculated the binding of the CO molecule with free neutral and charged Au_n ($n \leq 6$) clusters. They found that the binding energy for the cations decreases as the cluster grows, for the neutral complexes it increases with cluster size n until $n = 4$ and drops at $n = 5$. For the anions, it increases with n as well, but reaches a local maximum at $n = 5$.

Compared to the extensive literature on gold catalysis toward CO oxidation, studies on silver catalytic activity are relatively rare. Experimental studies have indicated that silver catalyze CO oxidation at low temperatures in different states such as free and supported Ag surfaces, powdered Ag and free and supported Ag nanoclusters [86, 96–103]. For example, Burghaus and Conrad [96] and Barth and Zambelli [97] found that CO is oxidized by the adsorbed O_2 on Ag(110) surface in temperature range 100–300K and the formation rate of CO_2 depends strongly on the reaction temperature. Yu et al [99] prepared ultrasmall Ag nanoparticles supported on SiO_2 and studied the effect of their size on the CO oxidation. It was found a strong size dependent reaction and the Ag particle size in a range of 3–5 nm was favorable for CO oxidation. In addition, Tian et al [103] prepared Ag/SBA-15 catalyst which are uniform Ag nanoparticles with 6.0 nm diameter dispersed on SBA-15 mesoporous silica materials. This catalyst oxidize CO at low temperature if it is prepared with specific reducing reagent.

Furthermore, Bernhardt et al [98, 104] measured and calculated the binding energy of CO and O_2 molecules on silver and binary silver-gold anionic clusters consisting from five atoms. They found that silver cluster anions are unreacted toward CO molecule while two oxygen molecules adsorb on odd size anionic silver cluster and $Ag_nO_4^-$ complexes are proposed to be an intermediate in CO oxidation reaction over silver cluster. After that, Tang et al [101] increased the size cluster to 55 atoms and studied the effect of the charge on the catalytic performance, they found that all of the anionic, neutral, and cationic Ag_{55} clusters were able to promote CO oxidation at low temperatures.

In analogy to gold and silver, experimental and theoretical studies were done to investigate the role of the copper in CO oxidation [40, 86, 100, 105–115]. For example, Eren et al [115] studied the CO oxidation reaction over copper surface (111), they found that Cu(111) is a good catalyst at ambient pressure and room temperature. Sun et al [116] and Harrison et al [106] prepared the supported CuO and Cu(II) nanoparticles on CeO_2 surface. Sun et al [116] found that CuO nanoparticles oxidate CO at low temperature and Harrison et al [106] found that supported Cu(II) nanoparticles convert CO 100% into CO_2 at 343 K. In addition, Lee and Ervin investigated the reaction of CO toward copper cluster anions ($n \leq 13$) [86] while Leuchtner et al [105] investigated the reaction of CO toward copper cluster cations ($n \leq 14$). Both found that larger clusters ($n > 4$) are more

reactive than small clusters, and there is no even/odd alternation in rates or reaction.

Regarding the theoretical investigation on CO oxidation catalyzed by a copper surfaces and nanoclusters, both Yu [112] and Nygren and Siegbahn [111] found that the adsorption of CO on copper surface (001) and on cluster is chemisorption. In addition, Tang and Zhang [109] studied the mechanism of CO oxidation by copper nanocluster consisting of 55 atoms by spin-unrestricted DFT method. They found that Langmuir–Hinshelwood mechanism is more accepted than Eley–Rideal mechanism only if the entropy effect is included.

Furthermore, coinage metals catalyze NO reduction into N_2 or oxidation into NO_2 . For instance, there are many experimental and theoretical studies devoted to study the reaction of NO with gold in different states [53, 117–137]. For example, Vinod et al [117] observed that NO adsorbs on Au(310) stepped surface and then decomposes into NO_2 and oxygen atoms at 80 K, whereas the (111) and (110) surfaces are inactive in these bond breaking processes. Hussain et al [118] calculated the adsorption energies of NO on the previous surfaces and they show that the adsorption energy of NO increases considerably with increasing the degree of coordinative unsaturation of the gold atoms to which NO binds, which is consistent with the view that defects, steps and kinks on the surface determine the activity of gold catalysts. Moreover, McClure et al [53] studied the adsorption and the reaction of NO on Au(111) surface covered by oxygen atom under ultrahigh vacuum condition, it was shown that NO_2 was produced. Torres et al [119] characterize theoretically the previous surface reaction by performing DFT periodic slab model calculations. They found pre-adsorbed O atoms (at low coverage) enhance slightly the NO adsorption energy. The $(NO + O)/Au(111)$ species are shown to form the $NO_2/Au(111)$ product essentially without an activation barrier, releasing the heat of 170 kJ/mol.

Regarding the interaction of NO with free gold cluster, Ding et al [125] calculated the adsorption energies of NO on anionic, cationic and neutral clusters ($n \leq 6$) using DFT, they found an even-odd oscillation behavior of the adsorption energy of $AuNO_n^-$ and that the cationic cluster have bigger adsorption energies than the anionic and the neutral cluster. Olvera et al [132] calculated the adsorption energies of NO on neutral, cation and anion atoms using multireference configuration interaction (MRCI) methods and they

found that NO binds with the neutral and charged atoms and it forms covalent bond with the neutral atom and dative bond with the charged atoms.

About the interaction of silver with NO, there are many experimental and theoretical studies describing the adsorption of NO on free and supported silver clusters [138–146]. For instance, both Satokawa [140] and Breen et al [141] examine the conversion of NO to N₂ and NO₂ over supported silver cluster Ag/Al₂O₃. They found that the addition of hydrogen to the reaction has a remarkable effect in promoting NO reduction and oxidation. Hagen et al [146] investigated the reactivity of small silver cluster anions Ag_{2–5}[–] toward NO and mixtures of NO with CO. They found a strongly cluster size dependent reaction behavior, where reactive fragmentation dominates for clusters with four or fewer atoms and only Ag₅[–] is able to form reaction products without dissociation of the metal cluster. Ma et al [142] studied the reactions of NO toward larger charged silver clusters Ag_n[±] (n = 7 – 69) at low temperatures. They found evidence for NO adsorption, the formation of (NO)₂ and the reduction of NO on different cluster sizes.

Concerning the theoretical studies, Grönbeck et al [145] explore structural, electronic, and vibrational properties of NO, NO₂, NO₃ adsorption on small silver clusters, Ag_n (n = 1 – 8) using DFT method. They marked odd/even alternation in adsorption energies with a stronger bonding to odd clusters and the adsorption energies follow the trend E_a(NO) < E_a(NO₂) < E_a(NO₃) for all cluster size. After that, Torbatian et al [144] used the full-potential density functional theory as well as the pseudo-potential time-dependent DFT calculations to study adsorption of the toxic CO, NO, and HCN molecules on the Ag₈ cluster. They found that adsorption of these molecules changes the stable structure of Ag₈.

Finally, there are many theoretical and experimental studies describe the interaction of copper with NO [147–162]. For instance, Wendelken [158] examined the adsorption of NO on two different surfaces of copper, Cu(100) and Cu(110) as a function of exposure and temperature with initially clean surfaces. He found that the behavior of NO depends on the surface. On Cu(110), the adsorbed NO dissociates above 113 K, leaving O(ad) and N(ad) on the surface, while on Cu(100), some of the initially adsorbed NO is dissociated at 85 K leaving O(ad) while the N(ad) combines with arriving NO molecules to form N₂O(ad). In addition, Dumas et al [154] studied the interaction of NO on Cu(111),

they found that the interaction depends on the coverage and on the temperature of the substrate. For $T < 170\text{K}$, NO molecules are found to be adsorbed on one single site, then after completion of the NO monolayer, the adsorbed NO molecules react to form adsorbed N_2O molecules. Yen and Ho [150] studied the adsorption and the dissociation of NO and N_2O molecules on Cu(111) by DFT, they found that the dissociation of N_2O is an exothermic process and the dissociation of NO affected with the presence of N atom and O atom on the surface where the O atom raise the adsorption energy and N atom decrease it .

Holmgren et al [160] investigated the reactivity of Cu_n ($n = 15 - 80$) towards NO at room temperature and liquid-nitrogen temperature. They found similar behavior at both temperatures, where the reactivity of Cu_n with NO is very low overall for ($n = 15 - 41$) and higher for larger cluster. Hirabayashi and Ichihashi [159] studied the adsorption and reaction of NO onto charged clusters Cu_n^\pm and $\text{Cu}_n\text{O}_m^\pm$ ($n = 3 - 19$, $m \leq 9$) experimentally and theoretically, they found that the reactivity of Cu_n^\pm toward NO is very low overall, but some specific $\text{Cu}_n\text{O}_m^\pm$ ions are highly reactive. In addition, they found that the NO adsorption probability of an anionic copper cluster is significantly enhanced by the preadsorption of two oxygen atoms.

Although there are already many studies in the literature about the interaction of coinage metals with NO and CO, not much details are known about the exact binding of CO and NO to the coinage metals atoms. In addition, there are no studies calculated or measured the vibrational spectroscopic constants for the monocarbonyl coinage metals and mononitrosyl coinage metals. The first step to determine those constants and to know the exact binding of CO and NO with coinage metals atoms is calculating the potential energy surface. Therefore, the main aim of my thesis is to calculate potential energy surface (PES) for neutral and charged $\text{MCO}^{0,\pm}$ and $\text{MNO}^{0,\pm}$ where M: Au, Ag, Cu. The PESs I have calculated depend on the distance and the angle between the geometrical center of CO or NO and the metal atom while the CO and NO distances are frozen. Then those potential energy surfaces are parametrized for molecular quantum dynamics calculation.

In facts, the catalysts should not bind with the reactants strongly. Therefore, in the catalytic reaction, weak interaction like van der Waals interactions are important. This

type of interaction is represented by dynamic correlation which is comparable to the dispersion correlation in DFT method. The dispersion corrections in DFT is not suitable for all binding situations. The dynamic correlation can be calculated with post-Hartree Fock methods of which the coupled cluster method with singles, doubles and perturbative triples (CCSD(T)) is the most accurate method for single reference cases. This method also have the advantage of giving a more satisfactory account of open shell systems while it is not trivial to get a defined spin state of the system within DFT. This is important when alternative spin states are close in energy. However, the scaling with electron number (N) is poor in CCSD(T), with computer time proportional to N^7 . This limits make the CCSD(T) applicable for the system with small number of electrons. Therefore, I used effective core potential for the coinage atoms to reduce number of electrons and then make the calculations faster.

Here I calculated two dimensional potential energy surface (2D-PESs) that describe the adsorption of CO and NO molecules on anionic, cationic and neutral coinage metals atoms using CCSD(T). I presents the details of the computational scheme in chapter two. In chapter three, I investigate the electronic structure of the ground states of the neutral and the ions of the coinage metals. In addition, I investigate the electronic structure of the CO, NO molecules and of the coinage metal dimer. In chapter four, I investigate how the the CO molecule adsorbs on the coinage metals atoms by calculating the potential energy surface of binding the ground state of the CO molecule with the ground state of the coinage metals atoms and ions, the binding energies were calculated at different distances and angles. Then I find the optimized parameters of neutral and charged monocarbonyl complexes and their vibrational frequencies. After that, I find the PES of binding the CO with the coinage metal dimer to see the effect of increasing the number of metal atoms on the binding energy. In chapter five, I investigate the adsorption of the NO molecule on the coinage metals atoms, ions and dimers by following the same protocol in chapter four. Since the the NO molecule have open shell electronic structure, the adsorption of NO on the coinage atom and ions produces different spin states, hence, the number of the PESs for coinage metals nitrosyl is larger than the number of PESs of coinage metals carbonyl. Finally, I summarize the results in chapter six and make a comparison between the coinage metals, charge states and the behavior of the CO and the NO toward the coinage metals atoms.

Theory and methodology

In 1900, Max Planck developed a theory, the so-called blackbody radiation, to study the light emitted by heated solids. This theory is considered the beginning of quantum mechanics [163]. After about 25 years, Heisenberg, Born and Jordan [164] had developed a complete and consistent theory of quantum mechanics, called matrix mechanics. In 1926, Erwin Schrödinger introduced the concept of the wave function. It is a mathematical function that depends on both, time and space, in a wave-like manner, which carries within it all information about a particle or system. In addition, he introduced a linear partial differential equation that describes the time-evolution of the system's wave function, once the system's environment (potential) is non-relativistic or treated within the pseudopotential approach [165]. This equation is known as time dependent Schrödinger equation (TDSE):

$$i\hbar \frac{\partial \Phi(\vec{r}, t)}{\partial t} = \widehat{H}\Phi(\vec{r}, t), \quad (2.1)$$

where $\Phi(\vec{r}, t)$ is the wave function which depends on the time and the spatial coordinates of the system, \widehat{H} is the Hamiltonian operator and E is the total energy of the system. This equation is difficult to solve for the systems exceeding two particles without approximation. The first step to solve TDSE is to describe the investigated systems as stationary time-independent system by separating the time and the spatial dependency of the wave function, and only the spatial one is treated. This step leads to the time-independent Schrödinger equation (TISE):

$$\widehat{H}\Psi(\vec{r}) = E\Psi(\vec{r}). \quad (2.2)$$

The aim of this work is to find the molecular stationary wave function by solving Eq.2.2. The non-relativistic Hamiltonian for a molecule consisting of M nuclei and N electrons depends on the position vectors of the nuclei and the electrons \vec{R}_A and \vec{r}_i , respectively. It consists of five operators that are written in atomic units as :

$$\widehat{H}(\vec{R}, \vec{r}) = \underbrace{-\sum_{A=1}^M \frac{1}{2M_A} \nabla_A^2}_{\widehat{T}_{nuc}(\vec{R})} - \underbrace{\sum_{i=1}^N \frac{1}{2} \nabla_i^2}_{\widehat{T}_{elec}(\vec{r})} - \underbrace{\sum_{i=1}^N \sum_{A=1}^M \frac{Z_A}{r_{iA}}}_{\widehat{V}_{elec-nuc}(\vec{R}, \vec{r})} + \underbrace{\sum_{i=1}^N \sum_{j>i}^N \frac{1}{r_{ij}}}_{\widehat{V}_{elec-elec}(\vec{r})} + \underbrace{\sum_{A=1}^M \sum_{B>A}^M \frac{Z_A Z_B}{R_{AB}}}_{\widehat{V}_{nuc-nuc}(\vec{R})}, \quad (2.3)$$

Where M_A is the mass of the nucleus A in atomic units which equal to the ratio of the mass of the nucleus A to the mass of an electron. Z_A, Z_B are the atomic number of nucleus A, B , respectively. r_{iA}, r_{ij}, R_{AB} are the distances between the i th electron and A th nucleus, the i th and j th electron, and A th nucleus and B th nucleus, respectively.

The first two operators in Eq.2.3 represent the kinetic energy operators of the nuclei and the electrons. The third one represents the Coulomb attraction operator between the nuclei and the electrons. The fourth and the fifth operators represent the Coulomb repulsion operators between electrons and nuclei, respectively[166]. This equation can be solved numerically for H_2^+ [167], but for larger molecules approximations are necessary to find its total energy. The first approximation is the Born-Oppenheimer approximation.

2.1 Born-Oppenheimer Approximation

In 1927, Born and Oppenheimer introduced that electronic motion could be decoupled from nuclear motion, since the electronic mass is much smaller than the nuclear mass ($M_{\text{proton}}/m_e = 1836$). Therefore the electrons in the molecule considered to be moving in the field of fixed nuclei [168]. This can be expressed mathematically by writing the molecular wave function as a product of two functions; the nuclear wave function $\Omega_{nuc}(\vec{X})$ and the electronic wave function $\phi_{ele}(\vec{X}; \vec{x})$ that depends parametrically on the nuclear coordinates \vec{X} :

$$\Psi(\vec{X}, \vec{x}) = \Omega_{nuc}(\vec{X})\phi_{ele}(\vec{X}; \vec{x}). \quad (2.1)$$

where \vec{X} is short-hand notations for the spin $\vec{\Sigma}$ and position \vec{R} coordinates of all nuclei, while \vec{x} for the spin $\vec{\sigma}$ and position \vec{r} coordinates of all electrons, respectively.

$$\{\vec{r}, \vec{\sigma}\}, \{\vec{R}, \vec{\Sigma}\} = \vec{x}, \vec{X} \quad (2.2)$$

Insertion of this ansatz into Eq.2.2 and treating the R_A -dependence of ϕ_{ele} as a parameter, allows the separation of Eq.2.2 into an electronic Schrödinger equation that depends parameterically on nuclear coordinates :

$$(\hat{T}_{ele} + \hat{V}_{ele-nuc} + \hat{V}_{ele-ele})\phi_{ele}(\vec{X}; \vec{x}) = E_{ele}(\vec{X})\phi_{ele}(\vec{X}; \vec{x}), \quad (2.3)$$

and a nuclear Schrödinger equation:

$$(\hat{T}_{nuc} + \hat{V}_{nuc-nuc} + E_{ele}(\vec{X}))\Omega_{nuc}(\vec{X}) = E\Omega(\vec{X}_{nuc}). \quad (2.4)$$

Once the electronic problem is solved, the nuclear equation could be solved. The nuclear Schrödinger equation shows that the electronic energy and Coulomb interaction between the nuclei provides a potential for nuclear motion. Consequently, the nuclei in the Born-Oppenheimer approximation move on a potential energy surface obtained by solving the electronic Schrödinger equation. In addition, solving Eq.2.4 gives us the total energy of molecule, including electronic and vibrational energy which is the energy of Eq.2.2 with Born-Oppenheimer approximation.

For this work, only solving the electronic problem Eq.2.3 is interesting. So I drop the subscript "ele", H means the electronic Hamiltonian and ϕ means the electronic wave function for the further derivations.

2.2 Hartree-Fock Approximation

The first step in solving the electronic Schrödinger equation is to define the characteristic of the wave function. A many-electron wave function should take into account the indistinguishability of electrons, this means, the electronic density $|\phi|^2$ should be invariant to the exchange of the spin and space coordinate of the electrons. In addition, it must satisfy the Pauli exclusion principle. So it should be antisymmetric with respect to the

interchange of both spin and space coordinate of any two electrons and only one electron can occupy the spin orbital.

In 1929, John Slater [169] proposed a simple approximate expression for a wave function of a many-electron system, which has all the properties aforementioned, the so-called Slater determinant. The Slater determinant for N electrons is constructed from N occupied spin-orbitals $(\chi_a, \chi_b, \dots, \chi_N)$, which can be only occupied by one electron, without determining which electron is in which orbital as the following :

$$\phi_{SD}(\vec{x}) = \frac{1}{\sqrt{N!}} \begin{vmatrix} \chi_a(\vec{x}_1) & \chi_b(\vec{x}_1) & \cdots & \chi_N(\vec{x}_1) \\ \chi_a(\vec{x}_2) & \chi_b(\vec{x}_2) & \cdots & \chi_N(\vec{x}_2) \\ \vdots & \vdots & \ddots & \vdots \\ \chi_a(\vec{x}_N) & \chi_b(\vec{x}_N) & \cdots & \chi_N(\vec{x}_N) \end{vmatrix}, \quad (2.1)$$

where the factor $(\frac{1}{\sqrt{N!}})$ is the normalization factor. The rows are labeled by the electrons while the columns are labeled by the spin orbitals.

The Slater determinant satisfies the antisymmetric principle because interchanging the coordinate of any two electrons corresponds to interchanging two rows, which changes the sign of the Slater determinant. In addition, the Slater determinant is in accordance with Pauli exclusion principle since the determinant is zero if two electrons occupy the same spin orbital.

The Hartree-Fock method uses the variation principle to find the ground state electronic wave function [170]. The essence of this method is to use $\phi_{SD}(\vec{x})$ as a trial normalized wave function to calculate the expectation value of electronic Hamiltonian under the constraints that all the individual spin orbitals are orthonormal. Then vary the spin orbitals to find the minimum energy:

$$\mathbf{min} \underbrace{\langle \phi_{SD} | \widehat{H} | \phi_{SD} \rangle}_{\mathbf{E}\{\{\chi(\vec{x})\}\}}. \quad (2.2)$$

The set of spin orbitals that minimize the energy, construct the “best single determinant” or the ground state Hartree-Fock wave function Ψ_{HF} . In addition, the electronic energy

corresponds to ϕ_{HF} is the ground state energy E_{HF} :

$$E_{\text{HF}} = \langle \phi_{\text{HF}} | \hat{H} | \phi_{\text{HF}} \rangle. \quad (2.3)$$

The equations for finding the optimal spin orbitals are called the Hartree-Fock integro-differential equation:

$$\hat{f}(i)\chi_a(\vec{x}_i) = \varepsilon_a\chi_a(\vec{x}_i), \quad (2.4)$$

where \vec{f} is the Fock operator and ε_a is the orbital energy of spin orbital χ_a . The Fock operator consists of a one-electron operator $h(i)$ plus a Hartree-Fock potential operator $\nu^{\text{HF}}(i)$.

$$\hat{f}(i) = \hat{h}(i) + \hat{\nu}^{\text{HF}}(i). \quad (2.5)$$

The one-electron operator includes the attractive potential energy between all the nuclei and the i th electron plus its kinetic energy:

$$\hat{h}(i) = -\frac{1}{2}\nabla_i^2 - \sum_A \frac{Z_A}{r_{Ai}}. \quad (2.6)$$

The Hartree-Fock potential operator is an effective-one electron potential operator that gives the average potential experienced by the i th electron due to the presence of the other electrons. It consists of two operators, the Coulomb operator J_b and the exchange operator K_b :

$$\hat{\nu}^{\text{HF}}(\vec{x}) = \sum_b \hat{J}_b(\vec{x}) - \hat{K}_b(\vec{x}). \quad (2.7)$$

The Coulomb and exchange operators are defined by their effect when acting on the spin orbital χ_a as the following:

$$\hat{J}_b\chi_a(\vec{x}_i) = \int dx_j \frac{|\chi_b(\vec{x}_j)|^2}{r_i - r_j} \chi_a(\vec{x}_i), \quad (2.8)$$

$$\hat{K}_b\chi_a(\vec{x}_i) = \int dx_j \frac{\chi_b(\vec{x}_j)^* \chi_a(\vec{x}_j)}{r_i - r_j} \chi_b(\vec{x}_i). \quad (2.9)$$

The Coulomb operator is a local operator, since it gives the average local potential at a point in space (\vec{x}_i) due to the other electrons. The exchange operator is a non-local operator, because there does not exist a simple potential uniquely defined at a point in space (\vec{x}_i). The result of operating \hat{K}_b on $\chi_a(\vec{x}_i)$ depends on the value of χ_a throughout

all the space, not only at \vec{x}_i .

The Hartree-Fock equation is a Pseudo-eigenvalue equation because the Fock operator depends on the solution χ_a . Therefore, it can not be solved directly but only iteratively within the self consistent field (SCF) approach [171]. In brief, the principle of SCF method is making a starting guess for the set of N spin-orbitals $\{\chi(\vec{x})^0\}$ to construct the Fock operator. Then the set of N equations {Eq.2.4} is solved as an eigenvalue problem. Afterwards, the new orbitals $\{\chi(\vec{x})^1\}$ are used to construct a new Fock operator. The process is repeated until no significant change occurs in the total energy. Finally, the converged orbitals construct the ground state wave function and the ground state Hartree-Fock energy equal to:

$$E_{\text{HF}} = \sum_{a=1}^N \varepsilon_a - \frac{1}{2} \left(\sum_{a,b=1}^N \langle \chi_a | J_b | \chi_a \rangle + \langle \chi_a | K_b | \chi_a \rangle \right). \quad (2.10)$$

The Hartree-Fock method reduces the N -body wave function problem into N -coupled integro-differential equations or $N/2$ equations when spatial orbitals are used. Hartree-Fock equations are solved numerically for atoms and very small molecules [172], but it is impossible for larger systems.

In 1951, Roothaan [173] and Hall [174], independently proposed a different way for solving Hartree-Fock equations, by expanding the orbitals in a set of fixed basis functions:

$$\chi_a(\vec{x}) = \sum_{k=1}^K C_{ka} \varphi_k(\vec{x}), \quad (2.11)$$

where the basis functions φ and their number K have been chosen in advance and only the expansion coefficients C_{ka} are varied.

Introducing the linear combination of Eq.2.11 into Hartree-Fock equations Eq.2.4, then multiplying the result from left by $\varphi_l^*(\vec{x})$, and integrate over \vec{x} , yields a set of algebraic equations that solved by standard matrix techniques. These equations called the Roothaan-Hall equations:

$$\sum_{k=1}^K C_{ka} \int d\vec{x}_i \varphi_l^*(\vec{x}_i) \hat{f}(i) \varphi_k(\vec{x}_i) = \varepsilon_a \sum_{k=1}^K C_{ka} \int d\vec{x}_i \varphi_l^*(\vec{x}_i) \varphi_k(\vec{x}_i), \quad (2.12)$$

which can be written more compactly as a single matrix equation:

$$FC = SC\epsilon \quad (2.13)$$

where F, C, S, ϵ represent the Fock matrix, the expansion coefficient matrix, the overlap matrix and the diagonal orbital energy matrix, respectively.

The Fock matrix is $K \times K$ Hermitian matrix and its elements are given by:

$$F_{lk} = \langle \varphi_l | \hat{f}(\vec{x}) | \varphi_k \rangle = \int d\vec{x} \varphi_l^*(\vec{x}) \hat{f}(\vec{x}) \varphi_k(\vec{x}) \quad (2.14)$$

$$= \sum_l^K \sum_k^K \left(\int d\vec{x}_i \varphi_l^*(\vec{x}_i) \hat{h}(\vec{x}_i) \varphi_k(\vec{x}_i) + \sum_b^N \int d\vec{x}_i \varphi_l(\vec{x}_i) (J_b - K_b) \varphi_k(\vec{x}_i) \right). \quad (2.15)$$

The overlap matrix is a $K \times K$ Hermitian matrix and its element is given by :

$$S_{lk} = \langle \varphi_l | \varphi_k \rangle = \int d\vec{x}_i \varphi_l^*(\vec{x}_i) \varphi_k(\vec{x}_i) \quad (2.16)$$

The expansion coefficient matrix is $K \times K$ matrix which contains the coefficients of each spin orbital to the different basis functions.

The great advantage of Hartree-Fock-Roothaan-Hall approach is replacing the problem of determining the values of all occupied orbitals in all position-spin space points with determining only the expansion coefficient of the orbitals to the basis functions. Therefore, the iterative procedure is started by choosing the a starting guess for the coefficients C_{ka} , then construct the corresponding Fock matrix $F[C_{ka}^0]$, and solve the eigenvalue problem in Eq.2.13. In addition, it provide a systematic way to improve any calculation by increasing the number of the basis set functions. Finally, the Roothaan-Hall formulation can only offer an accurate solution to the Hartree-Fock equations because in actual calculation the basis set is finite. Additionally, the results are only reliable as long as the electronic wave function is approximated as single Slater determinant.

2.3 Post-Hartree-Fock methods

As seen in the previous section, the SCF theory produces the best single determinant wave function that treats the interactions between the electrons in an average way; in

such a manner, one electron moves in an average field of $n-1$ other electrons. Nevertheless, the electrons have instantaneous interactions among themselves. This means, their motion is correlated. Because of the correlated motion of the electrons, they keep apart from each other to reduce their mutual repulsion. Therefore, the energy corresponding to the exact correlated wave function for a molecule is lower than the Hartree-Fock energy even if the Hartree-Fock energy is obtained in the limit that the basis set approaches completeness. The energy difference between the exact non-relativistic electronic energy in Eq.2.3 and the Hartree-Fock energy at the complete basis set limit is called the correlation energy:

$$E_{\text{corr}} = E - E_{\text{HF}}, \quad (2.1)$$

The correlation energy has been the focal point of ab initio quantum physics and chemistry for about 60 years [175]. Because by calculating the correlation energy, the calculated properties such as bond lengths, angles, charge densities and dipole moments will be more accurate. The electron correlation is represented formally by allowing the electrons "to spend time" in the unoccupied spin orbitals so that the electrons are able to avoid each other. There are many schemes to calculate the correlation energy, that depend either on the Hartree-Fock ground state wave function or on the Fock operator. These methods are known as Post-Hartree-Fock methods such as the configuration interaction method, the coupled cluster method and Møller–Plesset perturbation theory.

2.3.1 Configuration Interaction

Configuration interaction (CI) is a systematic procedure for calculating the correlation energy. It is a variational method which means it provides an upper bound to the exact energy. The trial wave function used within the CI approach is represented as a linear combination of configuration state functions (CSFs). A configuration state function is a symmetry-adapted linear combination of Slater determinants, that have the same symmetry as the exact wave function:

$$|CI\rangle = C_0 |\psi_0\rangle + \left(\frac{1}{1!}\right)^2 \sum_{\substack{a \in \text{occ} \\ r \in \text{virt}}} C_a^r |\psi_a^r\rangle + \left(\frac{1}{2!}\right)^2 \sum_{\substack{ab \in \text{occ} \\ rs \in \text{virt}}} C_{ab}^{rs} |\psi_{ab}^{rs}\rangle + \left(\frac{1}{1!}\right)^2 \sum_{\substack{abc \in \text{occ} \\ rst \in \text{virt}}} C_{abc}^{rst} |\psi_{abc}^{rst}\rangle + \dots, \quad (2.2)$$

where the first term $|\psi_0\rangle$ represents the determinant formed from the N lowest energy spin orbitals that obtained from Hartree-Fock-Roothaan-Hall equation (ground state HF wave function). The second term represents the singly excited CSF, which differ from $|\psi_0\rangle$ in replacing one occupied spin orbital χ_a with the virtual spin orbital χ_r . The third term represents the doubly excited CSF, that constructed by replacing two occupied spin orbitals χ_a and χ_b with two virtual spin orbitals χ_r and χ_s . The third term represents the triply excited CSF, and so on. The expansion coefficients, $C_0, C_a^r, C_{ab}^{rs}, \dots$ are determined by using the linear variational principle. The factor $(\frac{1}{n!})^2$ in front of each CSF is to ensure that the excited determinants in each CSF is accounted once.

If the wave function is expanded with all possible CSFs of the appropriate symmetry (CI-space), up to the N-excited CSF, then the method is called full configuration interaction (FCI). However, it is convenient to rewrite the full CI wave function in a symbolic form as:

$$|CI\rangle = \sum_{i=0}^n \hat{C}_i |\text{HF}\rangle = \hat{C}_0 |\text{HF}\rangle + \hat{C}_1 |\text{HF}\rangle + \hat{C}_2 |\text{HF}\rangle + \hat{C}_3 |\text{HF}\rangle + \dots + \hat{C}_n |\text{HF}\rangle, \quad (2.3)$$

where $|\text{HF}\rangle$ represents Hartree-Fock wave function and \hat{C}_i represents the excitation operator that produces i th-excited Slater determinants. For example, \hat{C}_2 produces all possible doubly excited Slater determinants.

The FCI scheme solves the electronic Schrödinger equation exactly within the space spanned by the one-particle basis set. The FCI approach is computationally demanding, therefore various approximations are applied on the FCI wave function by truncating the CI-space. For instance, CID method is limited to doubly excited CSFs, and CISD method is limited to singly and doubly excitation CSFs.

The truncated CI methods, CID and CISD, greatly reduce the computational effort and give a reasonable approximation to the correlation energy, but they have a problem of size-inconsistency which simply means that the energy of two infinitely separated particles is not equal to the summation of the individual particle energy. The property of size consistency is very important to obtain correctly behaving dissociation curves. Because of that I did not use these methods to calculate the potential energy surfaces.

2.3.2 Perturbation Theory

Rayleigh-Schrödinger perturbation theory (RSPT)[176] is a systematic procedure for solving time-independent Schrödinger equation and consequently finding the correlation energy. It is not variational but is size-consistent at each level. The principle of this theory is to divide the total Hamiltonian of the system \widehat{H} into two parts, the first part is called a zeroth-order part, \widehat{H}_0 , which has known eigenfunctions and eigenvalues. The second part is a perturbation, \widehat{V} . In the following, I derive the energy expressions of RSPT following the procedure by Szabo and Ostlund [166].

In Rayleigh-Schrödinger perturbation theory, it is started with the Hamiltonian for the unperturbed system \widehat{H}_0 , that has a set of non-degenerate eigenfunctions $\{\psi_i^{(0)}\}$ which are orthogonal and form a complete space, and their corresponding eigenvalues are $E_i^{(0)}$:

$$\widehat{H}_0 |\psi_i^{(0)}\rangle = E_i^{(0)} |\psi_i^{(0)}\rangle, \quad (2.4)$$

the superscript ⁽⁰⁾, means unperturbed wave function and unperturbed energy (zero-order perturbation). In order to find an approximate eigenvalues and eigenfunctions of the total Hamiltonian (perturbed Hamiltonian):

$$\widehat{H} |\phi_i\rangle = \xi_i |\phi_i\rangle. \quad (2.5)$$

This is done by adding the perturbation \widehat{V} to H_0 :

$$\widehat{H} = \widehat{H}_0 + \lambda \widehat{V}, \quad (2.6)$$

where λ is an ordering parameter that controls the perturbation strength and it's value is between zero and one.

Next, the perturbed wave functions and the perturbed eigenvalues are expanded in power series in λ :

$$\xi_i = E_i^{(0)} + \lambda E_i^{(1)} + \lambda^2 E_i^{(2)} + \lambda^3 E_i^{(3)} + \dots, \quad (2.7)$$

$$|\phi_i\rangle = |\psi_i^{(0)}\rangle + \lambda |\psi_i^{(1)}\rangle + \lambda^2 |\psi_i^{(2)}\rangle + \lambda^3 |\psi_i^{(3)}\rangle + \dots, \quad (2.8)$$

Both wave functions, ψ_i^0 and ϕ_i , are assumed to satisfy the intermediate normalization:

$$\langle \psi_i^{(0)} | \psi_i^{(0)} \rangle = 1 = \langle \psi_i^{(0)} | \phi_i \rangle, \quad (2.9)$$

this leads to an orthogonality relation between the zero-order wave function and the higher order perturbed functions:

$$\langle \psi_i^{(0)} | \psi_i^{(n)} \rangle = 0 \quad n = 1, 2, 3, \dots \quad (2.10)$$

Afterwards, the energy expansion, wave function expansion and perturbed Hamiltonian are substituted into Eq.2.5:

$$\begin{aligned} & (\widehat{H}_0 + \lambda \widehat{V}) \left(|\psi_i^{(0)}\rangle + \lambda |\psi_i^{(1)}\rangle + \lambda^2 |\psi_i^{(2)}\rangle + \dots \right) = \\ & (E_i^{(0)} + \lambda E_i^{(1)} + \lambda^2 E_i^{(2)} + \dots) \left(|\psi_i^{(0)}\rangle + \lambda |\psi_i^{(1)}\rangle + \lambda^2 |\psi_i^{(2)}\rangle + \dots \right). \end{aligned} \quad (2.11)$$

Then the coefficients of λ^n on each side of the equation are set equal to each other. This leads to an infinite number of equations of the form:

$$\widehat{H}_0 |\psi_i^{(0)}\rangle = E_i^{(0)} |\psi_i^{(0)}\rangle \quad n = 0 \quad (2.12)$$

$$\widehat{H}_0 |\psi_i^{(1)}\rangle + \widehat{V} |\psi_i^{(0)}\rangle = E_i^{(0)} |\psi_i^{(1)}\rangle + E_i^{(1)} |\psi_i^{(0)}\rangle \quad n = 1 \quad (2.13)$$

$$\widehat{H}_0 |\psi_i^{(2)}\rangle + \widehat{V} |\psi_i^{(1)}\rangle = E_i^{(0)} |\psi_i^{(2)}\rangle + E_i^{(1)} |\psi_i^{(1)}\rangle + E_i^{(2)} |\psi_i^{(0)}\rangle \quad n = 2 \quad (2.14)$$

and so on. After multiplying these equations from left by $\langle \psi_i^{(0)} |$ and using the orthogonality relation (Eq.2.10), the expressions for the nth-order energies are obtained:

$$E_i^{(0)} = \langle \psi_i^{(0)} | H_0 | \psi_i^{(0)} \rangle \quad n = 0 \quad (2.15)$$

$$E_i^{(1)} = \langle \psi_i^{(0)} | V | \psi_i^{(0)} \rangle \quad n = 1 \quad (2.16)$$

$$E_i^{(2)} = \langle \psi_i^{(0)} | V | \psi_i^{(1)} \rangle \quad n = 2 \quad (2.17)$$

$$E_i^{(3)} = \langle \psi_i^{(0)} | V | \psi_i^{(2)} \rangle \quad n = 3 \quad (2.18)$$

$$E_i^{(n)} = \langle \psi_i^{(0)} | V | \psi_i^{(n-1)} \rangle \quad n = n \quad (2.19)$$

Clearly, the energy expansion of the perturbed system could be written in a compact way as a summation of the eigenvalues of H_0 and the matrix elements of the perturbation

between the eigenfunctions of H_0 :

$$\xi_i = E_i^{(0)} + \sum_{n=1}^{\infty} \lambda^n \langle \psi_i^{(0)} | V | \psi_i^{(n-1)} \rangle \quad (2.20)$$

However, if the H_0 is chosen wisely, then V is small and the expansion of the perturbation energy converges quickly.

To calculate the n^{th} order perturbation energy, the $|\psi_i^{(n-1)}\rangle$ must be known. This can be done in general by expanding the perturbed eigenfunction $|\psi_i^{(n)}\rangle$ in space of $\{\psi_i^{(0)}\}$. But because the $|\psi_i^{(0)}\rangle$ are orthogonal to $|\psi_i^{(n)}\rangle$ according to the orthogonality relation of Eq.2.10, then $|\psi_i^{(n)}\rangle$ is written as a linear combination of all other eigenfunctions of $\{\psi_i^{(0)}\}$:

$$|\psi_i^{(n)}\rangle = \sum_{l, l \neq i} C_{i,l}^{(n)} |\psi_l^{(0)}\rangle \quad (2.21)$$

where

$$C_{i,l}^{(n)} = \langle \psi_l^{(0)} | \psi_i^{(n)} \rangle \quad (2.22)$$

For instance, to find the expansion coefficients of the first order perturbed wave function $C_{i,l}^{(1)}$, one should insert the expansion of Eq.2.21 into Eq.2.13 and then multiply from left by $|\psi_l^{(0)}\rangle$, then the results is:

$$(E_i^{(0)} - E_l^{(0)}) \langle \psi_l^{(0)} | \psi_i^{(1)} \rangle = \langle \psi_l^{(0)} | \hat{V} | \psi_i^{(0)} \rangle \quad (2.23)$$

and so

$$C_{i,l}^{(1)} = \langle \psi_l^{(0)} | \psi_i^{(1)} \rangle = \frac{\langle \psi_l^{(0)} | \hat{V} | \psi_i^{(0)} \rangle}{(E_i^{(0)} - E_l^{(0)})}. \quad (2.24)$$

The expansion coefficients for the higher order perturbed wave functions are obtained in a similar way with increasingly complicated expressions. Once the perturbed wave function is found, the perturbed energies are calculated via Eq.2.19. Within this logical framework, the expressions for the perturbed energies are obtained for a general partitioning of the Hamiltonian.

Møller-Plesset Perturbation theory (MPPT)[177] is a particular formulation of many-body perturbation theory that finds the electron correlation energy as a perturbation on the Hartree-Fock solution.

2.3.2.1 Møller-Plesset Perturbation Theory

In 1934, Christian Møller and Milton S. Plesset [177] have applied RSPT on N-electron system to find the perturbation expansion for the correlation energy (MPPT). They used the Hartree-Fock Hamiltonian as the zero order Hamiltonian \widehat{H}_0 which is a sum of the one-electron Fock operator $\widehat{f}(i)$:

$$\widehat{H}_0 = \sum_i^N \widehat{f}(i) = \sum_i [\widehat{h}(i) + \widehat{v}^{\text{HF}}(i)] \quad (2.25)$$

The eigenfunction of \widehat{H}_0 is the Slater determinant $\psi_0^{(0)}$ formed from the set of the spin orbitals $\{\chi_a(\vec{x}_i)\}$, that are eigenfunctions of Fock-operator. The eigenvalue corresponds to each eigenfunction equals to the sum of the orbital energies included in the Slater determinant which could be either occupied or virtual:

$$\sum_i \widehat{f}(i) |\psi_0\rangle = \sum_{a \in \psi_0} \varepsilon_a |\psi_0\rangle. \quad (2.26)$$

The perturbation is defined as the difference between the exact electron-electron interaction and the Hartree-Fock potential:

$$V = \sum_{i < j} r_{ij}^{-1} - v^{\text{HF}}(i) = \sum_{i < j} r_{ij}^{-1} - \sum_b \widehat{J}_b(\vec{x}_i) - \widehat{K}_b(\vec{x}_i). \quad (2.27)$$

The zeroth order wave function of the Hartree-Fock Hamiltonian is simply the Hartree-Fock wave function $\psi_0^{(0)}$, and the corresponding zeroth order energy MP0 equal to the sum of the orbital energies $\{\varepsilon_a\}$ of the occupied orbitals .

$$\text{MP0} = E_0^{(0)} = \langle \psi_0^{(0)} | \sum_i \widehat{f}(i) | \psi_0^{(0)} \rangle = \sum_{a \in \text{occ}} \varepsilon_a \quad (2.28)$$

The first order perturbation energy $E_0^{(1)}$ is given by applying Eq.2.16:

$$E_0^{(1)} = \langle \psi_0^{(0)} | \left(\sum_{i < j} r_{ij}^{-1} - v^{\text{HF}}(i) \right) | \psi_0^{(0)} \rangle = -\frac{1}{2} \sum_b \widehat{J}_b(\vec{x}_i) - \widehat{K}_b(\vec{x}_i), \quad (2.29)$$

Then the total first order energy MP1 is :

$$\text{MP1} = \text{MP0} + E_0^{(1)} = \sum_a \varepsilon_a - \frac{1}{2} \sum_b \hat{J}_b(\vec{x}_i) - \hat{K}_b(\vec{x}_i), \quad (2.30)$$

which equals to the Hartree-Fock energy. Therefore, the total correlation energy is given by the sum over all orders starting from the second order:

$$E_{\text{corr}} = E_0^{(2)} + E_0^{(3)} + \dots \quad (2.31)$$

The second-order MPPT, or MP2 method approximates the electronic correlation energy to the second order:

$$E_{\text{corr}}^{\text{MP2}} = E_0^{(2)}, \quad (2.32)$$

then the MP2 energy is defined as:

$$\text{MP2} = \text{MP0} + E_0^{(1)} + E_0^{(2)} = E_0^{\text{HF}} + E_0^{(2)} = E_0^{\text{HF}} + E_{\text{corr}}^{\text{MP2}}, \quad (2.33)$$

the new information required to calculate the MP2 energy is only the first-order perturbed wave function $\psi_0^{(1)}$. It is expanded in space of the eigenfunctions of the Hartree-Fock Hamiltonian. But because of orthogonality constrain between $\psi_0^{(1)}$ and $\psi_0^{(0)}$ (Eq.2.10), and the Brillouin's theorem which states that there is no interaction between the Hartree-Fock ground state wave function and the singly excited determinants $\{\Psi_a^r\}$ [166], and the Slater-Condon rules [178],[179], the first order wave function expanded as:

$$\psi_0^{(1)} = \sum_{\substack{a>b \\ r>s}} C_{abrs}^{(1)} |\psi_{ab}^{rs}\rangle, \quad (2.34)$$

where the coefficients C_{ab}^{rs} are determined by the equation:

$$C_{abrs}^{(1)} = \langle \psi_0^{(1)} | \psi_{ab}^{rs} \rangle = \sum_{\substack{a>b \\ r>s}} \frac{\langle \psi_{ab}^{rs} | \psi_0^{(0)} \rangle}{\varepsilon_a + \varepsilon_b - \varepsilon_r - \varepsilon_s} \quad (2.35)$$

This wave function then placed in the second order energy expression to give:

$$E_0^{(2)} = \sum_{\substack{a>b \\ r>s}} \frac{[\langle \psi_0^{(0)} | \frac{1}{r_{12}} | \psi_{ab}^{rs} \rangle]^2}{\varepsilon_a + \varepsilon_b - \varepsilon_r - \varepsilon_s} \quad (2.36)$$

That means to calculate the MP2 correlation energy, only two electrons integrals and orbital energies are required. But, the energy calculation for MP3 and MP4 are more complex. MP2 recovers about 80-90 % of the correlation energy, while MP3 and MP4 recover about 90-95 %, 95-98 %, respectively. The MPn energy is not an upper bound to the exact energy, because MPPT because is not variational. However, to have more accurate results regarding the correlation energy, coupled cluster methods are used, which are explained in the next section.

2.3.3 Coupled-Cluster Theory

The coupled-cluster (CC) theory represents the most successful approach to accurate many-electron molecular wave functions. It is size-extensive and size-consistent and capable of recovering a large part of the correlation energy. additionally, the coupled-cluster wave function providing an accurate correction to the Hartree-Fock description. It describes the complicated correlated motion of interacting electrons by virtual excitation of electrons from occupied to unoccupied spin orbitals.

The coupled-cluster theory for molecular electronic calculations were developed by Sinanoglu [180], Nesbet [181], Čížek and Paldus [182–185] in the 1960s and by Bartlett and co-worker in the 1970s [186–188] and Pople and co-worker [189]. I present the CC theory by following the textbook "Molecular Electronic-Structure Theory" by Helgaker, Jørgensen and Olsen [190].

There are two approaches for constructing the coupled-cluster wave function, the product ansatz and the exponential ansatz. In the product ansatz, the coupled-cluster wave function is defined as a product of correlating operator $(1 + t_\mu \hat{\tau}_\mu)$ acting on the Hartree-Fock ground state $|\text{HF}\rangle$:

$$|\text{CC}\rangle = \left[\prod_{\mu} (1 + t_{\mu} \hat{\tau}_{\mu}) \right] |\text{HF}\rangle \quad (2.37)$$

$$= \left(1 + \sum_{\mu} t_{\mu} \hat{\tau}_{\mu} + \sum_{\mu > \nu} t_{\mu} \hat{\tau}_{\mu} t_{\nu} \hat{\tau}_{\nu} + \dots \right) |\text{HF}\rangle \quad (2.38)$$

$$= |\text{HF}\rangle + \sum_{\mu} t_{\mu} |\mu\rangle + \sum_{\mu > \nu} t_{\mu} t_{\nu} |\mu\nu\rangle + \dots \quad (2.39)$$

where $\hat{\tau}_{\mu}, \hat{\tau}_{\nu}$ are excitation operators of specified excitation level; both are single or

double or triple, etc, that generate excited Slater Determinants $|\mu\rangle, |\mu\nu\rangle$ and t_μ, t_ν are the associated amplitude which represents the probability of occurrence of the particular excitation. The restriction of $\mu > \nu$ applies because each excitation operator has to appear only once in the product in Eq.2.37 and the order of excitation operators is unimportant because they commute:

$$[\hat{\tau}_\mu, \hat{\tau}_\nu] = 0 \quad (2.40)$$

The excitation operators are defined as a product of annihilation (a_I) and creation (a_A^\dagger) operators, that annihilate the electrons from the occupied spin orbitals and create the electrons in virtual spin orbitals. For example, the single excitation operator annihilates an electron from the occupied spin orbital I and creates an electron in the virtual spin orbital A:

$$\hat{\tau}_I^A = a_A^\dagger a_I \quad (2.41)$$

and the double excitation operator annihilates two electrons from the occupied spin orbitals I and J and creates two electrons in the virtual spin orbitals A and B:

$$\hat{\tau}_{IJ}^{AB} = a_A^\dagger a_I a_B^\dagger a_J. \quad (2.42)$$

However, the excitation operators satisfy the relation:

$$\hat{\tau}_\mu^2 = 0, \quad (2.43)$$

since we can not remove an electron from a spin orbital, if it is not already there.

It is clear in Eq.2.39 that the excitation operator $\hat{\tau}_\mu$ generates the excited Slater determinant $|\mu\rangle$ with the associated amplitude t_μ which referred as connected cluster amplitude:

$$\hat{\tau}_\mu |\text{HF}\rangle = t_\mu |\mu\rangle. \quad (2.44)$$

In addition to the Slater determinant $|\mu\rangle$, the operator $\hat{\tau}_\mu$ generates a large number of determinants in collaboration with the other excitation operators, for instance:

$$\hat{\tau}_\mu \hat{\tau}_\nu |\text{HF}\rangle = \hat{\tau}_\nu \hat{\tau}_\mu |\text{HF}\rangle = t_\mu t_\nu |\mu\nu\rangle \quad (2.45)$$

The amplitude of such a composite excitation is the product of the amplitudes of the contributing excitations $t_\mu t_\nu$ which is referred as disconnected cluster amplitude.

The presence of product excitation in Eq.2.37 leads to generate the same excited Slater determinant with at least two mechanisms, by acting with one excitation operator or by acting with a composite of lower excitation operators. Therefore, the total amplitude equal to the sum of one connected cluster amplitude and other disconnected cluster amplitude. For example the determinate $|\mu\nu\rangle$ could be reached by the one excitation operator $\hat{\tau}_{\mu\nu}$ or by acting with two operators regardless of their order $\hat{\tau}_\mu, \hat{\tau}_\nu$. then their total amplitude equal to:

$$t_{\mu\nu}^{total} = t_{\mu\nu} + t_\mu t_\nu. \quad (2.46)$$

The optimization of the coupled cluster wave function is done either by variation principle or by solving the projected Schrödinger equation. The variational principle give rise to an intractable set of nonlinear equations for the amplitudes and thus a complicated energy. Therefore, the variational principle is abandoned and the projection formalism are used to find the energy and the amplitudes. The coupled-cluster energy is found by projecting the Schrödinger equation against the Hartree-Fock wave function:

$$E = \langle \text{HF} | \hat{H} | \text{CC} \rangle, \quad (2.47)$$

while the amplitudes is found by projecting the Schrödinger equation against the determinants with connected amplitudes:

$$\langle \mu | \hat{H} | \text{CC} \rangle = E \langle \mu | \text{CC} \rangle = E t_\mu. \quad (2.48)$$

Since the projected CC-equations are non-variational, the coupled cluster energy no longer represents the upper bound to the FCI energy.

Now , I will move to the exponential ansatz in which the CC wave function is written as an exponential of cluster operators \hat{T} acting on the normalized ground state Hartree-Fock wave function $|\text{HF}\rangle$:

$$|\text{CC}\rangle = e^{\hat{T}} |\text{HF}\rangle \quad (2.49)$$

which ensures the extensive property, i.e. the correct scaling with the number of electrons.

The cluster operator \hat{T} is a linear combination of excitation operators multiplied by the connected-cluster amplitude t_μ :

$$\hat{T} = \sum_{\mu} t_{\mu} \hat{\tau}_{\mu}. \quad (2.50)$$

However, the Taylor expansion of the operator $e^{\hat{T}}$ leads to the same expression as the expansion of the product function.

The excitation operator included in the cluster operator are not selected individually. Rather, a hierarchy of approximation is adopted by partitioning the cluster operator into a classes containing all single excitation, all double excitation, all triple excitation, and so on. Therefore, the cluster operator could be in other form:

$$\hat{T} = \hat{T}_1 + \hat{T}_2 + \dots + \hat{T}_n, \quad (2.51)$$

where \hat{T}_1 is the single excitation cluster operator, \hat{T}_2 is the double excitation cluster operator and n is the number of electrons in the molecule. The one and two cluster operators are defined as:

$$\hat{T}_1 = \sum_{A=n+1}^{\infty} \sum_{I=1}^n t_I^A a_A^\dagger a_I = \sum_{A=n+1}^{\infty} \sum_{I=1}^n t_I^A \hat{\tau}_I^A \quad (2.52)$$

$$\hat{T}_2 = \sum_{b=a+1}^{\infty} \sum_{a=n+1}^{\infty} \sum_{J=I+1}^n \sum_{I=1}^{n-1} t_{IJ}^{AB} a_A^\dagger a_I a_B^\dagger a_J = \sum_{b=a+1}^{\infty} \sum_{a=n+1}^{\infty} \sum_{J=I+1}^n \sum_{I=1}^{n-1} t_{IJ}^{AB} \hat{\tau}_{IJ}^{AB}. \quad (2.53)$$

As before, the indices I and J are used for the occupied Hartree-Fock spin orbitals and the indices A and B for the virtual spin orbitals. The cluster amplitudes t_{IJ}^{AB} are anti-symmetric with respect to permutations of both, A and B ,and I and J. However, the limits of the summation in the definition of \hat{T}_1 and \hat{T}_2 are chosen to include all possible excitations without duplication. The same definition holds for $\hat{T}_3, \dots, \hat{T}_n$. The operator \hat{T} terminates at \hat{T}_n because the maximum number of excitations have to be equal to the number of the electrons in $|\text{HF}\rangle$.

One should be careful to the definition of the cluster operators, $\hat{T}_1, \hat{T}_2, \dots, \hat{T}_n$ because if they operate on an excited determinant which have electrons in both occupied and virtual spin orbitals, the result is a sum of higher excited determinants because the cluster operators excite the electrons from the occupied spin orbitals in $|\text{HF}\rangle$ and not from the

virtual spin orbitals. For example, the results of $\hat{T}_1^2 |\text{HF}\rangle = \hat{T}_1(\hat{T}_1 |\text{HF}\rangle)$ is a double excited Slater determinants, and $\hat{T}_2^2 |\text{HF}\rangle$ contains only quadruple excited Slater determinants. (This definition makes the operators amplitudes different to the CI coefficients, because the amplitudes of some higher excitation are a product of lower excitations).

The CC theory becomes applicable after making two approximations. First, using a finite basis set instead of using a complete basis set. This produces a finite number of virtual spin orbitals which are used to form the excited Slater determinants. Second, including only a few of the cluster operators rather than including all the operators.

To compare coupled-cluster model with FCI model, one expand the operator e^T and then collect the term of the same excitation level.

$$e^{\hat{T}} |\text{HF}\rangle = \sum_i^N \hat{C}_i |\text{HF}\rangle \quad (2.54)$$

Then, the configuration operators \hat{C}_i are given in term of cluster operators:

$$\hat{C}_0 = 1 \quad (2.55)$$

$$\hat{C}_1 = \hat{T}_1 \quad (2.56)$$

$$\hat{C}_2 = \hat{T}_2 + \frac{\hat{T}_1^2}{2!} \quad (2.57)$$

$$\hat{C}_3 = \hat{T}_3 + \hat{T}_1\hat{T}_2 + \frac{\hat{T}_1^3}{3!} \quad (2.58)$$

$$\hat{C}_4 = \hat{T}_4 + \frac{\hat{T}_2^2}{2!} + \frac{\hat{T}_1^2\hat{T}_2}{2!} + \hat{T}_1\hat{T}_3 + \frac{\hat{T}_1^4}{4!} \quad (2.59)$$

$$\hat{C}_5 = \hat{T}_5 + \hat{T}_1\hat{T}_4 + \hat{T}_2\hat{T}_3 + \frac{\hat{T}_1^2\hat{T}_3}{2!} + \frac{\hat{T}_1^3\hat{T}_2}{3!} + \frac{\hat{T}_1\hat{T}_2^2}{2!} + \frac{\hat{T}_1^5}{5!} \quad (2.60)$$

These equations show that the excited configurations can be generated by different mechanisms. For example, the doubly excitation configurations can be reached by two mechanisms, by connected \hat{T}_2 term which describes the simultaneous interaction of two electrons and by two disconnected simultaneous singly excitations. The triply excited configurations are generated via three mechanisms, the connected \hat{T}_3 term which describes the simultaneous interaction of three electrons, by the disconnected combination of a double and a single excitation and by the three disconnected single excitations. The quadruple

and quintuple excited configurations can be reached via five and seven mechanisms, respectively.

The FCI and the full coupled-cluster wave functions contain the same number of parameters because there is one connected cluster amplitude for each determinant. However the FCI provides a linear set of parameters while the full coupled-cluster provides a non-linear set of parameters. The advantages of the non-linear parametrization become apparent only upon the truncation, since the truncated coupled-cluster wave function still have contributions from all determinants in the FCI wave function which are constructed by a combination of disconnected excitation. For example, the inclusion of only single and double cluster operators (CCSD), generates in addition to all singly and doubly excited determinants, as in CISD, higher excited determinants which reached by the products of single and double excitation. This ensures that the truncated coupled-cluster methods are size-extensive and size-consistent.

The projected coupled-cluster equations with the exponential ansatz are expressed slightly different than the product ansatz. First, multiply the Schrödinger equation from left by $e^{-\hat{T}}$ to obtain:

$$e^{-\hat{T}} \hat{H} e^{\hat{T}} |\text{HF}\rangle = E |\text{HF}\rangle \quad (2.61)$$

This equation is considered as a Schrödinger equation with an effective, non-Hermitian similarity-transformed Hamiltonian:

$$\hat{H}^T = e^{-\hat{T}} \hat{H} e^{\hat{T}} \quad (2.62)$$

Then, projecting the similarity-transformed Schrödinger equation against the Hartree-Fock determinant to get the energy:

$$\langle \text{HF} | e^{-\hat{T}} \hat{H} e^{\hat{T}} | \text{HF} \rangle = E \quad (2.63)$$

and projecting against the determinants with connected amplitudes to get the amplitudes

$$\langle \mu | e^{-\hat{T}} \hat{H} e^{\hat{T}} | \text{HF} \rangle = 0 \quad (2.64)$$

which are equivalent to Eq.2.47 and Eq.2.48. After that, the similarity-transformed

Hamiltonian is expressed using the Baker–Campbell–Hausdorff (BCP) expansion as a sequence of nested commutator which terminates after the five term:

$$e^{-\hat{T}}\hat{H}e^{\hat{T}} = \hat{H} + [\hat{H}, \hat{T}] + \frac{1}{2}[[\hat{H}, \hat{T}], \hat{T}] + \frac{1}{6}[[[\hat{H}, \hat{T}], \hat{T}], \hat{T}] + \frac{1}{24}[[[[\hat{H}, \hat{T}], \hat{T}], \hat{T}], \hat{T}] \quad (2.65)$$

The first CC calculations was coupled-cluster double (CCD) with a wave function $e^{\hat{T}_2} |\text{HF}\rangle$. Although it is limited to the expansion of the two-body cluster \hat{T}_2 ,

$$e^{\hat{T}} = 1 + \hat{T}_2 + \frac{\hat{T}_2^2}{2!} + \frac{\hat{T}_2^3}{3!} + \dots, \quad (2.66)$$

it contains the essential disconnected amplitude of quadruple excitation and the amplitudes of the higher even-ordered excitation, which are the dominant parts of the excitation for Hartree-Fock wave function.

Although the CCD method includes the dominants contribution for the correlation energy, it is necessary to include the single-particle clusters, \hat{T}_1 , and their products with themselves and with \hat{T}_2 . The full Coupled-cluster single and double excitation method (CCSD), has a wave function $|\text{CCSD}\rangle = e^{\hat{T}_1 + \hat{T}_2} |\text{HF}\rangle$ and the equation for single amplitude is:

$$\begin{aligned} \langle \mu_1 | \hat{H} | \text{HF} \rangle + \langle \mu_1 | [\hat{H}, \hat{T}_1] | \text{HF} \rangle + \langle \mu_1 | [\hat{H}, \hat{T}_2] | \text{HF} \rangle + \frac{1}{2} \langle \mu_1 | [[\hat{H}, \hat{T}_1], \hat{T}_1] | \text{HF} \rangle \\ + \langle \mu_1 | [[\hat{H}, \hat{T}_1], \hat{T}_2] | \text{HF} \rangle + \frac{1}{6} \langle \mu_1 | [[[\hat{H}, \hat{T}_1], \hat{T}_1], \hat{T}_1] | \text{HF} \rangle = 0 \end{aligned} \quad (2.67)$$

and the double amplitude equation is:

$$\begin{aligned} \langle \mu_2 | \hat{H} | \text{HF} \rangle + \langle \mu_2 | [\hat{H}, \hat{T}_1] | \text{HF} \rangle + \langle \mu_2 | [\hat{H}, \hat{T}_2] | \text{HF} \rangle + \frac{1}{2} \langle \mu_2 | [[\hat{H}, \hat{T}_1], \hat{T}_1] | \text{HF} \rangle \\ \langle \mu_2 | [[\hat{H}, \hat{T}_1], \hat{T}_2] | \text{HF} \rangle + \frac{1}{2} \langle \mu_2 | [[\hat{H}, \hat{T}_2], \hat{T}_2] | \text{HF} \rangle + \frac{1}{6} \langle \mu_2 | [[[\hat{H}, \hat{T}_1], \hat{T}_1], \hat{T}_1] | \text{HF} \rangle \\ + \frac{1}{2} \langle \mu_2 | [[[\hat{H}, \hat{T}_1], \hat{T}_1], \hat{T}_2] | \text{HF} \rangle + \frac{1}{24} \langle \mu_2 | [[[[\hat{H}, \hat{T}_1], \hat{T}_1], \hat{T}_1], \hat{T}_1] | \text{HF} \rangle = 0 \end{aligned} \quad (2.68)$$

However, the non-linear equations of the amplitude are solved self-consistently. The CCSD scheme includes the most important correlation processes; the pair correlation via \hat{T}_2 , and pair-pair interactions via \hat{T}_2^2 . The single excitation carries out the orbital relaxation effects which considered as a part of the non-dynamic correlation effects. The quadruple excited determinants are described in CCSD mostly via the process \hat{T}_2^2 because the truncation leads to a neglect of the less probable processes \hat{T}_4 and $\hat{T}_3\hat{T}_1$. The main error in CCSD

scheme arise from neglecting the connected triple cluster operators \hat{T}_3 and depending only on \hat{T}_1^3 and $\hat{T}_1\hat{T}_2$, that have a low weight to the energy contribution from the triple excitation.

To improve the CCSD method, the triple connected excitation is added by truncating the CC wave function at \hat{T}_3 level, then we obtain the full coupled-cluster singles doubles and triples (CCSDT) model [191, 192]. This model is very accurate because it describe the dynamical correlation but it is computationally demanding and can be applied only for small system.

However, Barlet and Pople and their co-workers [193–197] attempted to define an economical approximations to CCSDT by applying many-body perturbation theory MPPT for the triple term which reduces the computational cost and retains much of the accuracy. They create different approximations which are conventionally divided into two classes; iterative and non-iterative methods. The iterative methods are the same as the full CCSDT, the equations of the amplitude of \hat{T}_1 , \hat{T}_2 , and \hat{T}_3 are coupled and are solved in an iterative way, but the difference is that the \hat{T}_3 equation is truncated. For example CCSDT-1 [193, 194], CCSDT-2 [195], CCSDT-3 [195] and CCSDT-4 [196]. The second class is the non-iterative methods, such as CCSD + T(CCSD)[194] and CCSD(T) [197], in these methods, the amplitude equation of \hat{T}_3 is decoupled from the \hat{T}_1 and \hat{T}_2 , then the contributions of \hat{T}_3 are estimated from taking the terms introduced in the iterative method CCSDT -1, but evaluating them non-iteratively. Accordingly, \hat{T}_1 and \hat{T}_2 gives an initial approximation for \hat{T}_3 , but \hat{T}_3 not allowed to change \hat{T}_1 and \hat{T}_2 . Therefore, these methods are much more economical than their iterative counterparts.

This work depends mainly on the CCSD(T) method, therefore, I would like to write in detail about it. The key point to understand this method is the coupled-cluster perturbation theory (CCPT) which connects the coupled-cluster theory and the perturbation theory by expanding the full coupled cluster wave function (Eq.2.49), the coupled cluster energy (Eq.2.63) and the similarity transformed Schrödinger equation (Eq.2.61) in order of the perturbed potential \hat{V} , as will be seen later.

As in MP2 scheme, the electronic Hamiltonian is divided into Fock operator and the perturbation potential $\hat{H} = \hat{f} + \hat{V}$, and the electronic energy is expanded in orders of the

perturbation:

$$E = E^{(0)} + E^{(1)} + E^{(2)} + \dots = \sum_{n=0}^{\infty} E^{(n)} \quad (2.69)$$

but the perturbed wave function is expanded using the exponential cluster ansatz instead of linear ansatz:

$$|\psi^{(n)}\rangle = e^{\hat{T}} |\text{HF}\rangle, \quad (2.70)$$

where

$$\hat{T} = \hat{T}^{(1)} + \hat{T}^{(2)} + \hat{T}^{(3)} + \dots = \sum_{n=1}^{\infty} \hat{T}^{(n)} \quad (2.71)$$

where $\hat{T}^{(1)}$ is the first order cluster operator, $\hat{T}^{(2)}$ is the second order cluster operator, and so on. After substituting the electronic Hamiltonian and the perturbed wave function and energy into the Schrödinger equation, then multiplying from left with $[e^{-\hat{T}^{(n)}}]$, the similarity transformed Schrödinger equation is obtained:

$$\hat{H}^T |\text{HF}\rangle = E^{(n)} |\text{HF}\rangle \quad (2.72)$$

where

$$\hat{H}^T = e^{-\hat{T}^{(n)}} (\hat{f} + \hat{V}) e^{\hat{T}^{(n)}} = \hat{f}^T + \hat{V}^T, \quad (2.73)$$

The similarity transformed Fock operator \hat{f}^T equals to :

$$\hat{f}^T = e^{-\hat{T}^{(n)}} \hat{f} e^{\hat{T}^{(n)}} = \hat{f} + \sum_{n=1}^{\infty} \sum_{\mu} \varepsilon_{\mu} t_{\mu}^{(n)} \tau_{\mu} \quad (2.74)$$

where the expansion of the perturbed cluster amplitudes $t_{\mu}^{(n)}$ is :

$$t_{\mu}^{(n)} = t_{\mu}^{(0)} + t_{\mu}^{(1)} + t_{\mu}^{(2)} + \dots, \quad (2.75)$$

and an example of the energy ε_{μ} is:

$$\varepsilon_{ABIJ} = \varepsilon_A + \varepsilon_B - \varepsilon_I - \varepsilon_J. \quad (2.76)$$

Next, the terms of order (n) in the similarity transformed Schrödinger equation (Eq.2.72) are collected:

$$\hat{f} |\text{HF}\rangle = E^{(0)} |\text{HF}\rangle \quad (2.77)$$

$$\sum_{\mu} \varepsilon_{\mu} t_{\mu}^{(n)} \tau_{\mu} |\text{HF}\rangle + [\hat{V}^T]^{(n)} |\text{HF}\rangle = E^{(0)} |\text{HF}\rangle, \quad n > 0 \quad (2.78)$$

However, projecting Eq.2.72 against the $|\text{HF}\rangle$ gives the energy $E^{(n)}$ which equals to :

$$E^{(n)} = \langle \text{HF} | \hat{f}^T | \text{HF} \rangle + \langle \text{HF} | \hat{V}^T | \text{HF} \rangle = E_0 + \langle \text{HF} | \hat{V}^T | \text{HF} \rangle \quad (2.79)$$

where E_0 equal to the sum of orbital energies of all the occupied spin orbitals. Then projecting against the excited determinant with connected amplitudes give :

$$\varepsilon_{\mu} t_{\mu}^{(n)} = - \langle \mu | [\hat{V}^T]^{(n)} | \text{HF} \rangle \quad (2.80)$$

Next, the BCH expansion is applied to the $\hat{V}^T = e^{-\hat{T}} \hat{V} e^{\hat{T}}$ and the expansion of \hat{T} (Eq.2.71) is substituted to get the order of the amplitude for each excitation, for example:

$$\varepsilon_{\mu} t_{\mu}^{(1)} = - \langle \mu | \hat{V} | \text{HF} \rangle \quad (2.81)$$

$$\varepsilon_{\mu} t_{\mu}^{(2)} = - \langle \mu | [\hat{V}, \hat{T}^{(1)}] | \text{HF} \rangle \quad (2.82)$$

$$\varepsilon_{\mu} t_{\mu}^{(3)} = - \langle \mu | [\hat{V}, \hat{T}^{(2)}] | \text{HF} \rangle - \frac{1}{2} \langle \mu | [[\hat{V}, \hat{T}^{(1)}], \hat{T}^{(1)}] | \text{HF} \rangle \quad (2.83)$$

This mean the excitations at each order of perturbation are determined by the amplitude equation (Eq.2.80). For instance, only the double excitations contribute to the first order of perturbation. The single excitations do not contribute because of Brillouin theorem, and the higher-order excitations can not couple with the Hartree-Fock state by a two-electron operator. The singles and triples excitations start to appear at the second order of perturbation.

The knowledge of the perturbed cluster amplitudes leads to calculate the CCPT wave function according to Eq.2.70:

$$|\psi^{(0)}\rangle = |\text{HF}\rangle \quad (2.84)$$

$$|\psi^{(1)}\rangle = \hat{T}^{(1)} |\text{HF}\rangle = \hat{T}_2^{(1)} |\text{HF}\rangle \quad (2.85)$$

$$|\psi^{(2)}\rangle = (\hat{T}^{(2)} + \frac{1}{2} \hat{T}^{(1)} \hat{T}^{(1)}) |\text{HF}\rangle = (\hat{T}_1^{(2)} + \hat{T}_2^{(2)} + \hat{T}_3^{(2)} + \frac{1}{2} \hat{T}_2^{(1)} \hat{T}_2^{(1)}) |\text{HF}\rangle \quad (2.86)$$

$$\begin{aligned}
|\psi^{(3)}\rangle &= (\hat{T}^{(3)} + \hat{T}^{(2)}\hat{T}^{(1)} + \frac{1}{6}\hat{T}^{(1)}\hat{T}^{(1)}\hat{T}^{(1)}) |\text{HF}\rangle = \hat{T}_1^{(3)} |\text{HF}\rangle + \hat{T}_2^{(3)} |\text{HF}\rangle \\
&+ (\hat{T}_3^{(3)} + \hat{T}_1^{(2)}\hat{T}_2^{(1)}) |\text{HF}\rangle + (\hat{T}_4^{(3)} + \hat{T}_2^{(2)}\hat{T}_2^{(1)}) |\text{HF}\rangle + \hat{T}_3^{(2)}\hat{T}_2^{(1)} |\text{HF}\rangle \\
&+ \frac{1}{6}\hat{T}_2^{(1)}\hat{T}_2^{(1)}\hat{T}_2^{(1)} |\text{HF}\rangle
\end{aligned} \tag{2.87}$$

The first order wave function (Eq.2.85) contains only the connected doubles while the second order wave function (Eq.2.86) contains besides to the connected singles, doubles and triples, disconnected quadruples. The higher order wave function contains a large number of disconnected cluster amplitudes.

Now, the coupled-cluster energy corrections are evaluated according to the formula in Eq.2.78, after expanding the similarity-transformed perturbation potential in BCH series:

$$E^{(0)} = E_0 \tag{2.88}$$

$$E^{(1)} = \langle \text{HF} | \hat{V} | \text{HF} \rangle \tag{2.89}$$

$$E^{(2)} = \langle \text{HF} | [\hat{V}, T_2^{(1)}] | \text{HF} \rangle \tag{2.90}$$

$$E^{(3)} = \langle \text{HF} | [\hat{V}, T_2^{(2)}] | \text{HF} \rangle \tag{2.91}$$

$$E^{(4)} = \langle \text{HF} | [\hat{V}, T_2^{(3)}] | \text{HF} \rangle \tag{2.92}$$

$$E^{(5)} = \langle \text{HF} | [\hat{V}, T_2^{(4)}] | \text{HF} \rangle + \frac{1}{2} \langle \text{HF} | [[\hat{V}, T_1^{(2)}], \hat{T}_1^{(2)}] | \text{HF} \rangle \tag{2.93}$$

Then, the optimized energy expression is found using the Lagrange multiplier technique [198]. This method of optimization leads to energy expression E^{2n+1} :

$$\begin{aligned}
E^{(n)} &= E^{(0)}\delta_{n,0} + \langle \text{HF} | [\hat{V}^T]^{(0)} | \text{HF} \rangle + \sum_{\mu} \sum_{k=1}^{n-1} \varepsilon_{\mu} t_{\mu}^{(k)} \bar{t}_{\mu}^{(n-k)} + \\
&\sum_{\mu} \sum_{k=1}^{n-1} \bar{t}_{\mu}^{(k)} \langle \mu | [\hat{V}^T]^{(n-k)} | \text{HF} \rangle.
\end{aligned} \tag{2.94}$$

The method that combines the CC theory and the MBPT are called hybrid method, in which the contribution of the highest excitations are approximated to the lower order in the perturbation potential. Iterative hybrid methods are termed as CCN, for instance, CC2 is an approximation of CCSD, in that the double cluster operator is included to the first order only. CC3 is an approximation to CCSDT, in that the triple cluster operator is included to the second order only. These method generates improved wave function with

lower cost compared with non-hybrid CC methods. But, if the energy has to be calculated only, non-iterative hybrid CC method as CCSD(T) is more economical than CC3.

The CCSD(T) is the most successful non-iterative hybrid model, it is known an "gold standard" of electronic structure theory. In CCSD(T) an a perturbative (non-iterative) correction is added to the CCSD energy:

$$E^{\text{CCSD(T)}} = E^{\text{CCSD}} + \Delta E^{\text{CCSD(T)}}, \quad (2.95)$$

where $\Delta E^{\text{CCSD(T)}}$ includes two terms of the fifth order CCPT energy correction that contain triple connected amplitudes. In conclusion, the CCSD(T) energy is calculated by solving the full CCSD iteratively, then the single and double amplitudes are used to calculate the second order corrected wave function that is used to calculate the fourth and fifth order energy corrections that are added to the CCSD energy.

We apply CCSD(T) method which is a well balance method between accuracy and computaional cost. Hence, the calculated electronic energy includes a large amount of correlation energy and it is calculated within reasonable computational time. In addition, this method is size-extensive and size-consistance, thus it gives accurate binding energy.

2.4 Computational details

The calculation were carried out using post-Hartree-Fock ab initio method based on spin unrestricted coupled-cluster singles and doubles and a perturbative estimate of triple excitaions UCCSD(T) method as implemented in MOLPRO package [199]. The UCCSD(T) wave function depends on HF wave function which is calculated using Roothan-Hall equations. Hence, each atomic orbital is expanded in a finite set of basis functions.

In order to minimize the error resulting from the the use of finite basis set, Augmented correlation-consistent basis sets of Dunning and coworkers [200, 201] were tested, because they are designed for converging Post-Hartree-Fock calculations systematically to the complete basis set limit using empirical extrapolation techniques [202].Hence, augmented polarized valence triple zeta basis set(avtz) was chosen for carbon, oxygen and nitrogen [200].

In addition, effective core potentials (ECPs) are used to replace the inner (core) electrons of coinage atoms by an effective potential and treat only the valence electrons explicitly in the calculations, in order to treat the relativistic effects and to reduce the computational effort as well. The number of core electrons that replaced by ECP is 60, 28, 10 for gold, silver and copper [203], respectively, and the 19 valence electrons are represented by avtz basis set [204].

2.4.1 Basis set superposition error and Counterpoise Correction

The binding energy $\Delta E(AB)$ of complex consists from monomer A and B is found by subtracting the electronic energy of each monomer from the electronic energy of the complex AB:

$$\Delta E(AB) = E_{AB}^{AB}(AB) - E_A^A(A) - E_B^B(B), \quad (2.1)$$

where the superscripts denote the basis used, the subscripts denote the geometry, and the symbol in parentheses denotes the chemical system considered. Thus, $E_{AB}^{AB}(AB)$ represents the energy of the complex AB evaluated with the union of the basis sets on A and B, at the geometry of the complex. Likewise, both monomers A and B are each evaluated at their own geometries in their own basis sets.

When the monomers A and B are far apart, there is no overlap between their basis functions and each monomer uses only its own basis set to describe its electronic structure. But, as monomer A approaches monomer B, each monomer in the complex can “steal” basis functions from the other monomer, lowering the energy of the complex in a way that is not possible for the isolated monomers, thus leading to overbinding of the complex when one computes its binding energy. Such problem is ascribed to “basis set superposition error” (BSSE) [205, 206] and it is more pronounced for smaller basis sets.

Counterpoise correction (CP)[207] is prescription for eliminating the BSSE. The BSSE for each monomer is evaluated by subtracting the energy of monomer in its own basis functions from the energy of monomer in the complex basis functions:

$$E_{BSSE}(A) = E_A^{AB}(A) - E_A^A(A), \quad (2.2)$$

$$E_{BSSE}(B) = E_B^{AB}(B) - E_B^B(B), \quad (2.3)$$

The energy of the monomer in the complex basis functions must necessarily be lower (more stable) than the energy of the monomer in its own basis functions, so the BSSEs are negative. If the BSSEs of both monomers are subtracted from the binding energy defined in Eq.2.1, the terms $E_A^A(A)$, $E_B^B(B)$ cancel, yielding:

$$\Delta E^{CP}(AB) = E_{AB}^{AB}(AB) - E_A^{AB}(A) - E_B^{AB}(B) \quad (2.4)$$

Practically speaking, to estimate the energy of monomer A in the complex basis functions, one places all the basis functions of monomer B on the atomic centers of the monomer B while neglecting the electrons and the nuclear charges of the monomer B. The basis functions on the monomer B are thus referred to as “ghost functions”, or the atoms of the monomer B are referred to as “ghost atoms”. Likewise, the atoms of the monomer A are considered ghost atoms to estimate $E_B^{AB}(B)$. Hence, eliminating the BSSEs decreases the magnitude of binding energy.

In this study, I calculate the counterpoise corrected binding energies of the neutral and charged coinage atoms with CO, NO, respectively, to form monocarbonyl coinage metals complexes ($M - CO^{0,\pm}$) and mononitrosyl coinage metals complexes ($M - NO^{0,\pm}$), where M: Au, Ag, Cu. Thus, I consider the coinage metals atom as the first monomer and the CO or NO as the second monomer. Then I calculated the counterpoise corrected binding energy as define in Eq.2.4

Electronic properties of monomers

A potential energy surface (PES) is a plot of molecular energy as a function of molecular geometry. The molecular energy is divided into four categories; translational, rotational, vibrational and electronic energy. This study is interested in the PES of electronic energy that is calculated using the CCSD(T) method. The electronic energy depends on the type of atoms consisting the molecule and on the number of electrons included in the calculation. Therefore, to compare between different molecules regarding the stability and the effect of charge, one should calculate the PES of binding energy rather than the electronic energy.

The PESs I have calculated describe the binding of charged or neutral coinage metals with CO or NO to form monocarbonyl coinage metals $(M - CO)^{0,\pm}$ and mononitrosyl coinage metals $(M - XO)^{0,\pm}$ complexes with M being Au, Ag, Cu, as the following reaction:



Each point of the PES represents a counterpoise corrected binding energy (E_{CP})[207] which is calculated using the following formula:

$$E_{\text{CP}} = E((M - XO)^{0,\pm}) - E(M^{0,\pm}) - E(XO), \quad (3.2)$$

where the $E((M - XO)^{0,\pm})$ is the electronic energy of the complex, $E(M^{0,\pm})$ is the electronic energy of the metal atom or its ions, and $E(XO)$ is the electronic energy of CO or NO. Both energies, $E(M^{0,\pm})$ and $E(XO)$, were calculated for the same geometry as in the

complex with a basis set of both constituents to remove the basis set superposition error [208].

In order to calculate the binding energy of $E((M - CO)^{0,\pm})$ and $E((M - NO)^{0,\pm})$ complexes, it is very important to know what are the electronic ground states of the carbon monoxide (CO), nitrogen monoxide (NO) molecules and the coinage metal atoms.

3.1 Carbon monoxide

Carbon monoxide (CO) consists of one carbon atom (C) and one oxygen atom (O). The electron configuration of carbon and oxygen atoms are $1s^2 2s^2 2p^2$ and $1s^2 2s^2 2p^4$, respectively, both C and O atoms have 3P_g as a ground state. The molecular electronic states of CO resulting from the combination of the ground state of C and O according to Wigner-Witmer rules[209] are: $2 \times ^1\Sigma^+, ^1\Sigma^-, ^1\Pi, ^1\Delta, 2 \times ^3\Sigma^+, ^3\Sigma^-, ^3\Pi, ^3\Delta, 2 \times ^5\Sigma^+, ^5\Sigma^-, ^5\Pi, ^5\Delta$. The molecular ground state of CO based on the UCCSD(T)/AVTZ calculation is $^1\Sigma^+$ with a bond length equals to 1.136 Å and the vibrational frequency 2143.3 cm^{-1} in the harmonic approximation, which agree reasonably well with the corresponding experimental values 1.128 Å and 2169.8 cm^{-1} [210].

The canonical molecular orbitals diagram of the CO ground state is given in Fig.3.1.1. It is similar to the electron configuration of neutral C_2 molecule, but with 10 electrons; four valence electrons come from carbon and six valence electrons come from oxygen. In addition, the s-p mixing is clear since the 3σ orbital is higher in energy than the 1π orbital. Therefore, the electronic configuration of CO molecule ($^1\Sigma^+$) is $(1\sigma)^2(2\sigma^*)^2(1\pi)^4(3\sigma)^2$ which have a bond order of 3. This means that CO contains formally a triple bond; one σ bond and two π bonds.

The highest occupied molecular orbital (HOMO) of CO is 3σ orbital is shown in Fig.3.1.2. It is built from the sigma combination of two p atomic orbitals and the s orbitals. It is not totally symmetric; there is a larger lobe on the carbon atom than on the oxygen atom. Because the nuclear charge of carbon atom is less than of oxygen atom which make the atomic orbitals of carbon higher in energy than the oxygen's orbitals and closer to 3σ molecular orbital.

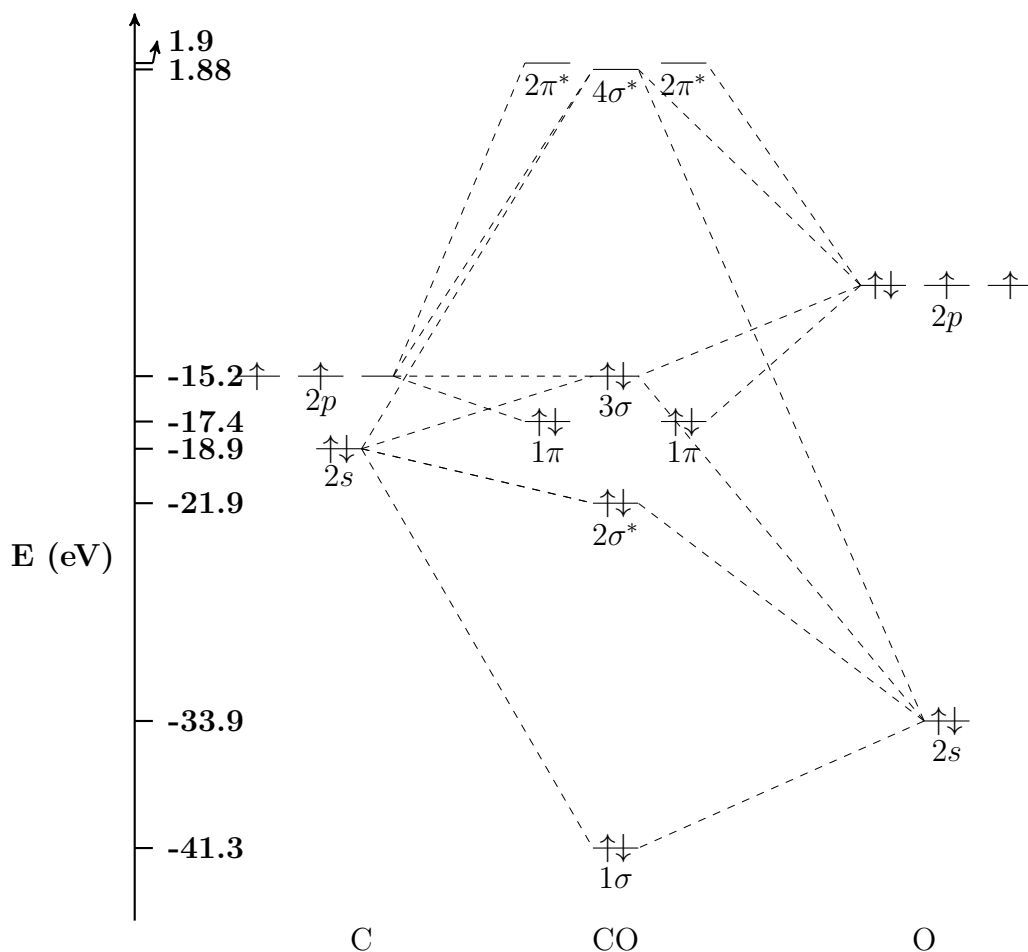


Figure 3.1.1: Energy level diagram for canonical valence molecular orbitals of carbon monoxide molecule ($^1\Sigma^+$) using RHF/AVTZ. The atomic orbitals of carbon and oxygen are calculated with CASSCF(4/4) and (6/4)/AVTZ, respectively.

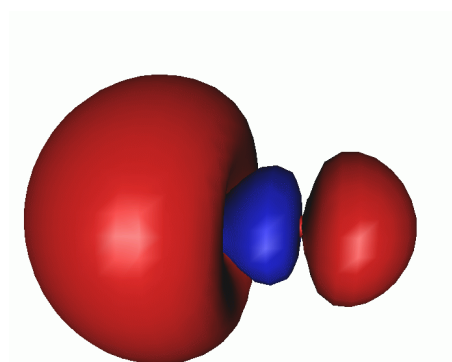


Figure 3.1.2: The highest occupied molecular orbital (HOMO) of CO (3σ). The carbon atom on the left and the oxygen atom on the right, the isocontour is 0.025. The contribution of s and p atomic orbitals are: $\text{HOMO} = -0.62C_{2s} + 0.71C_{p_x} + 0.06O_{2s} - 0.38O_{p_x}$.

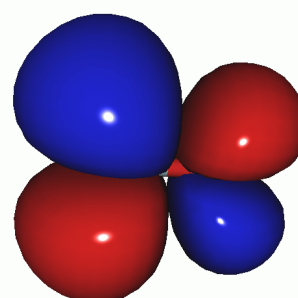


Figure 3.1.3: The highest occupied molecular orbital (HOMO) of NO ($2\pi^*$). The nitrogen atom on the left and the oxygen atom on the right, the isocontour is 0.025. The contribution of p atomic orbitals are: $\text{HOMO} = +0.88N_{p_x} - 0.69O_{p_x}$.

3.2 Nitrogen monoxide

Nitrogen monoxide (NO) or Nitrosyl radical consists from one nitrogen atom (N) and one oxygen atom (O). The electron configuration of nitrogen atom is $1s^2 2s^2 2p^3$ which have 4S_u ground state. The combination of the ground states of nitrogen and oxygen atoms leads to the following states $^2\Sigma^+$, $^2\Pi$, $^4\Sigma^+$, $^4\Pi$, $^6\Sigma^+$, $^6\Pi$. The molecular ground state of NO molecule based on the UCCSD(T)/AVTZ is $^2\Pi$ state with a bond length 1.157 Å and vibrational frequency 1889.08 cm^{-1} which agree reasonable well with the experimental values 1.151 Å and 1904.04 cm^{-1} [210].

The valence electrons configuration of NO molecular ground state is $(1\sigma)^2(2\sigma^*)^2(3\sigma)^2(1\pi)^4(2\pi^*)^1$, see Fig.3.2.1, resulting from CASSCF (5/ 4)/AVTZ method. The HOMO is an antibonding singly occupied orbital, see Fig.3.1.3, which leads to a bond order of 2.5, one sigma bond and 1.5 pi bond. The unpaired electron makes the NO molecule a free radical, which is unstable and tending to lose or gain an electron. Hence, the NO molecule is more reactive than the CO molecule.

Oxygen and nitrogen do not equally contribute to form the molecular orbitals of NO because of the difference in the nuclear charge. The nitrogen atomic orbitals are higher in energy than the oxygen atomic orbitals, see Fig.3.2.1, therefore, the nitrogen contributes more to antibonding orbitals, while the oxygen contributes more to bonding orbitals. This explains why the HOMO of NO has larger lobes on the nitrogen side. Therefore, the NO molecule tends to bind with other atoms from nitrogen side.

In conclusion, the important difference between CO and NO is the symmetry and the occupancy of the HOMO; the CO's HOMO is double occupied and has σ symmetry while the NO's HOMO is singly occupied and has a π symmetry.

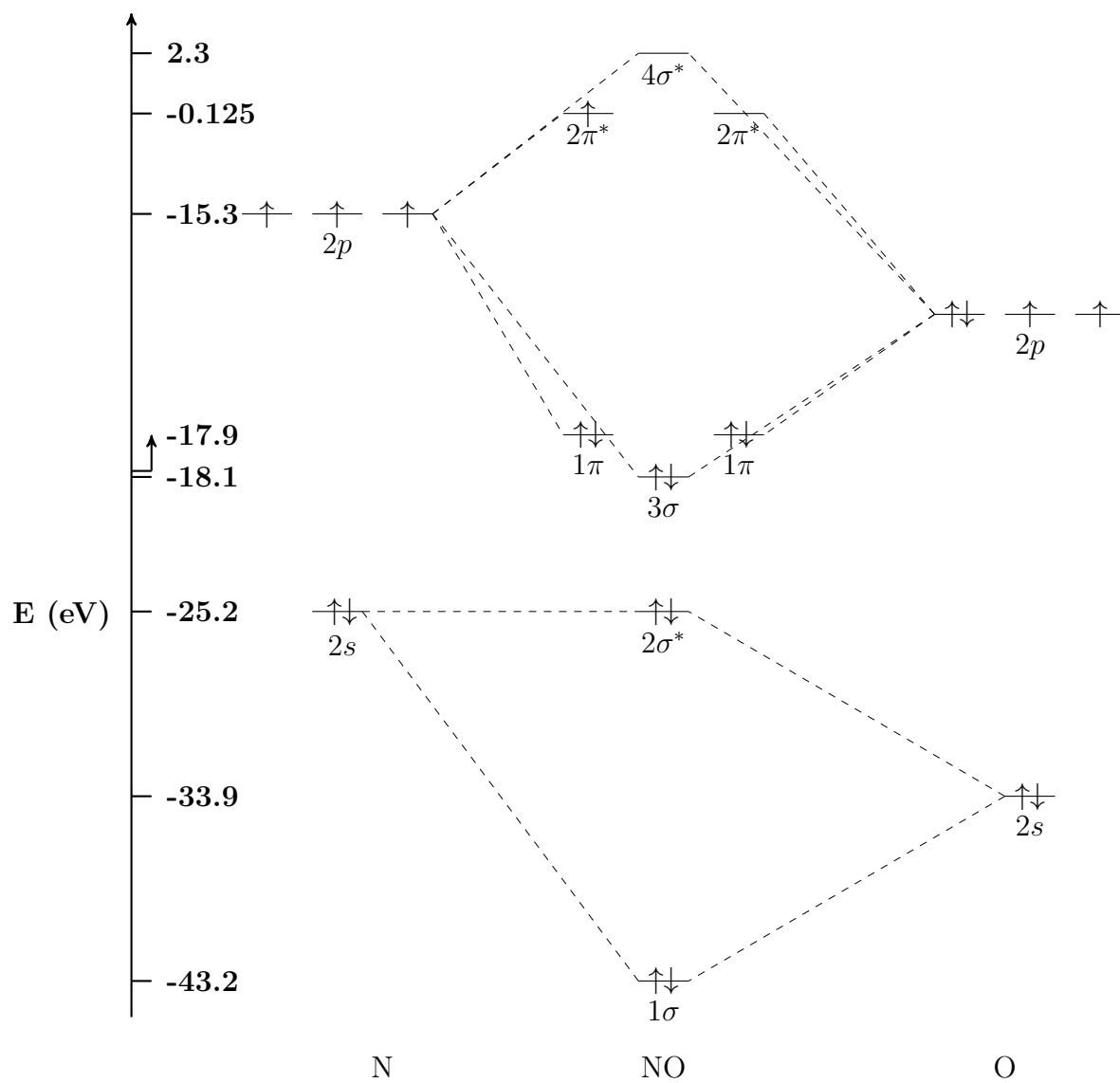


Figure 3.2.1: Energy level diagram for natural valence molecular orbitals of nitrogen monoxide molecule ($^2\Pi$) using CASSCF(5/4)/AVTZ.

3.3 Coinage metals atom

Copper (Cu), silver (Ag) and gold (Au) are known as coinage metals, due to their former usage in minting the coins. They are transition metals belonging to group 11 of the periodic table. They have same electron configuration pattern in the outermost shells. The three elements have 2S ground state with a full d subshell and singly occupied s subshell as it listed in the Tab.3.3.1. But the first and the second excited states are not the same; copper's and gold's first excited state is 2D , and the second excited state is 2P . While silver's first excited state and second excited state are 2P and 2D , respectively.

M	Atomic term	ΔE (eV)	ΔE_{exp} (eV)	Electrons configuration	M^\pm	Atomic term	ΔE (eV)	ΔE_{exp} (eV)	Electrons configuration
Cu	2S	0	0	[Ar]3d ¹⁰ 4s ¹	Cu ⁺	1S	0	0	[Ar]3d ¹⁰
	2D	1.3	1.5	[Ar]3d ⁹ 4s ²		3D	2.7	2.8	[Ar]3d ⁹ 4s ¹
	2P	3.8	3.8	[Ar]3d ¹⁰ 4p ¹		Ag ⁺	1S	0	0
Ag	2S	0	0	[Kr]4d ¹⁰ 5s ¹	3D		5.2	5.3	[Kr]4d ⁹ 5s ¹
	2P	3.7	3.7	[Kr]4d ¹⁰ 5p ¹	Au ⁺		1S	0	0
	2D	6.6	4.0	[Kr]4d ⁹ 5s ²		3D	2.6	2.5	[Xe]4f ¹⁴ 5d ⁹ 6s ¹
Au	2S	0	0	[Xe]4f ¹⁴ 5d ¹⁰ 6s ¹		Cu ⁻	1S	0	0
	2D	1.8	1.9	[Xe]4f ¹⁴ 5d ⁹ 6s ²	3P		1.7	-	[Ar]3d ¹⁰ 4s ¹ 4p ¹
	2P	4.9	4.9	[Xe]4f ¹⁴ 5d ¹⁰ 6p ¹	Ag ⁻		1S	0	0
Au ⁻						3P	1.7	-	[Kr]4d ¹⁰ 5s ¹ 5p ¹
						Au ⁻	1S	0	0
					3P		2.6	-	[Xe]4f ¹⁴ 5d ¹⁰ 6s ¹ 6p ¹

Table 3.3.1: The ground and the excited states of neutral atom, cation and anion of coinage metals and the their corresponding excitation energy calculated by UCCSD(T)/ECP(10,28,60)MDF-AVTZ. The experimental values correspond to the mean values of total angular momentum (J) over all spin-orbital components of the state [211].

The excitation energies for each element are calculated as the difference between the total electronic energy of the excited state and of the ground state. As shown in Tab.3.3.1, copper atom has the lowest excitation energies, followed by the gold atom then the silver.

Furthermore, the difference in the value of the first excitation energy between copper and gold is small in comparison with the difference in their atomic number. In addition, the energy needed to move an electron from the s subshell to the p subshell is nearly the same for copper and silver, and less than for gold. This is because relativistic effects are predominant in gold, which lower the energy of s and p AOs and increase the energy of the d AO [212].

The ground state and the first excited state for the cations of the coinage metals were calculated. Tab.3.3.1 shows clearly that the ground state of the three cations is 1S , in which the atom lost an electron from the s orbital. Moreover, the first excited state of the cation is 3D where the electron is lost from the d orbital. Furthermore, the copper and gold cations have nearly the same excitation energy which is lower than the Ag^+ cation.

The ground state of the anions and their first excited state were calculated, too. As it seen in Tab.3.3.1, the three elements have 1S ground state with full occupied s orbital. The first excited state is 3P , for which the electron is transferred to the p orbital. Finally, the values of the first excitation energy do not show the same trends as for the cations; while, the copper and silver have the same value and lower than the gold's anion.

In addition, the ionization potential (IE) and the electron affinity (EA) for coinage elements, CO and NO molecules were calculated, see Tab.3.3.2. The IE is defined as the minimum amount of energy that an isolated atom in the ground electronic state must absorb to expel an electron, resulting in a cation:



where M is any neutral atom and M^+ is its cation. In computational chemistry, the IP is calculated using the following formula:

$$IP = E(M^+) - E(M), \quad (3.2)$$

where $E(M^+)$ and $E(M)$ are the electronic ground state energy of the cation and neutral atom, respectively.

The electron affinity (EA) is basically the opposite of IP; it reflects the ability of an atom to accept an electron. It is defined as the energy change that occurs when an electron is

added to the atom, resulting in an anion:



Moreover, the electron affinity is calculated using the following formula:

$$EA = E(M^-) - E(M), \quad (3.4)$$

where $E(M^-)$ is the electronic ground state of the anion. As it seen in Tab.3.3.2, the coinage metals have negative EA and positive IP. This means that the coinage anions are more stable than the neutral atoms and the neutral atom are more stable than the cation ($E(M^-) < M < E(M^+)$). Regarding the CO and the NO molecules, they have positive IP and EA. This mean that the neutral molecules are more stable than the anions, and the anions are more stable than the cations ($E(\text{CO/NO}) < E(\text{CO/NO}^-) < E(\text{CO/NO}^+)$). According to this results, the $\text{MCO}^{0,\pm}$ and $\text{MNO}^{0,\pm}$ complexes will be formed by binding the neutral CO or NO with $M^{0,\pm}$.

Metal CO/NO	Cu		Ag		Au		CO		NO	
	cal	exp	cal	exp	cal	exp	cal	exp	cal	exp
IP (eV)	7.65	7.73 [213]	7.45	7.58 [214]	9.03	9.23 [215]	13.9	14.0 [216]	9.2	9.2 [217]
EA (eV)	-1.18	-1.23 [218]	-1.23	-1.30 [218]	-2.17	-2.31 [219]	1.5	1.3 [220]	0.011	0.026 [221]

Table 3.3.2: Ionization potential (IP) and electron affinity (EA) of copper, silver, gold atoms and CO, NO molecules calculated by CCSD(T)/ECPnMDF-AVTZ, where n being the number of core electrons that are replaced by a pseudopotential, 10 for Cu, 28 for Ag and 60 for Au.

3.4 Coinage metal dimer

The molecular ground state of any coinage metals dimer is $^1\Sigma$ which results from the combination of atomic ground state 2S . A comparison of calculated and experimental bond lengths is presented in Tab.3.4.1. As it is seen, there is good agreement between the

calculated and the experimental values of the bond length. The interatomic distance in gold dimer is shorter than the silver dimer because of the relativistic effect [212, 222].

Dimer	Cu ₂		Ag ₂		Au ₂	
	cal	exp	cal	exp	cal	exp
Bond length (Å)	2.221	2.220 [210]	2.545	2.531[223]	2.500	2.472 [210]

Table 3.4.1: The bond length of copper, silver and gold dimer calculated by CCSD(T)/ECP_nMDF-AVTZ, where n is the number of core electrons which are replaced by pseudopotential, 10 for Cu, 28 for Ag and 60 for Au.

The canonical valence molecular orbital diagrams of coinage metals dimers have the same pattern. It is shown in Fig.3.4.1. They differ only in the values of the energy levels. Tab.3.4.2 gives the energy of the s and the d atomic orbital and the HOMO and the LUMO of the dimers. The energy gap between the s and d atomic orbital of the gold is 4.4 eV which is less than the energy gap in copper and silver. This is a consequence of the relativistic effect according to which the s orbital contracts and the d orbital expands [212, 222]. In addition, the LUMO's energy of gold dimer is negative while it is positive for copper and silver, this means that the electron affinity of gold dimer is more than the silver and copper.

Metal	Copper	Silver	Gold
Energy of atomic orbital d (eV)	-13.0533	-13.8479	-12.3050
Energy of atomic orbital s (eV)	-6.6624	-6.4572	-7.8969
Energy of molecular orbital 3σ (eV)	-6.4543	-6.3310	-7.9588
Energy of molecular orbital 4σ* (eV)	0.0983	0.0253	-0.3201

Table 3.4.2: The energy of s and d atomic orbitals for copper, silver and gold atoms and the HOMO and the LUMO of their dimers calculated by RHF/ECP_nMDF-AVTZ, where n is the number of core electrons which are replaced by pseudopotential, 10 for Cu, 28 for Ag and 60 for Au.

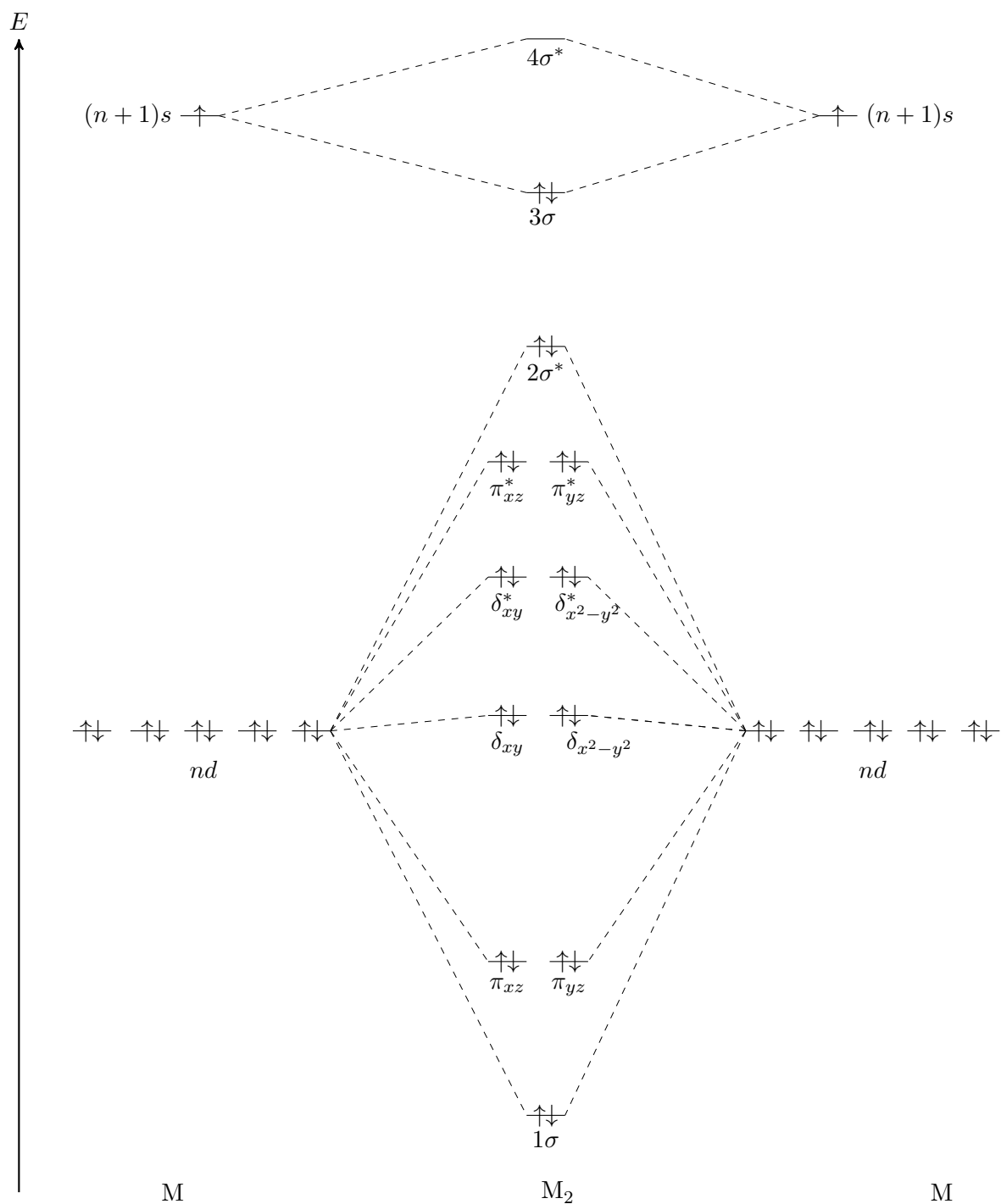


Figure 3.4.1: The canonical valence molecular orbital diagram of $M_2(^1\Sigma)$ with M : Au, Ag, Cu. The shell number is represented by $n = 5, 4, 3$ for Au, Ag, Cu

CHAPTER 4

Two dimensions potential energy surfaces of coinage metals carbonyl complexes

Coinage metals monocarbonyl complexes are compounds that contain one CO as a coordinated ligand (M-CO, M: Au, Ag, Cu). To understand how the CO adsorbs on the coinage metal atom, the potential energy surfaces (PESs) of the neutral and the charged coinage metals monocarbonyl complexes are calculated. The full PES for a complex consists from three atoms should be a function of three parameters (two bond lengths and one bond angle). According to Bistoni et al [224], the CO bond length in different carbonyl complexes differs by 0.001 Å to 0.01 Å from the free CO bond length. Hence, to make the calculations easier, the calculated PES is a function of two parameters only; the distance and the angle between the coinage metal atom and the geometrical center of CO bond, see Fig. 4.0.1, the CO bond length is fixed to its equilibrium bond length 1.136 Å, that is calculated by CCSD(T)/AVTZ. Hence, the PES is called two dimensional potential energy surface (2D-PES).

Each point of the 2D-PES represents the counterpoise corrected binding energy, E_{CP} . It is calculated at different distances and angles with respect to the dissociation limits which are the molecular ground state of the neutral CO molecule and the ground state of the neutral atom or its anion or cation, depending on the charge of the complex. Depending on the results of chapter three, the molecular ground state of the CO molecule is $^1\Sigma^+$, and each coinage metal atom, cation, anion have 2S , 1S , 1S atomic ground states, respectively.

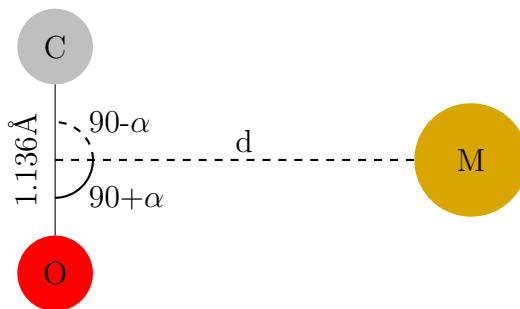


Figure 4.0.1: M-CO geometry selected for the 2D-PES, the distance and the angle between the coinage metal atom and the CO center is represented by (d) and (α) , respectively. At $\alpha = 90^\circ$ the complex has a linear geometry MCO and at $\alpha = -90^\circ$ the complex has a linear geometry MOC.

Hence the , E_{CP} , for the neutral and charged complexes are calculated, respectively, as:

$$E_{CP} = E(\text{MCO}) - E(\text{M}(^2\text{S})) - E(\text{CO}(^1\Sigma^+)), \quad \text{where } M : \text{Au, Ag, Cu}, \quad (4.1)$$

$$E_{CP} = E(\text{MCO})^\pm - E(\text{M}^\pm(^1\text{S})) - E(\text{CO}(^1\Sigma^+)), \quad \text{where } M : \text{Au, Ag, Cu}, \quad (4.2)$$

where all electronic energy terms in the Eqs. 4.1, 4.2 were calculated using the basis set of the complex to remove the BSSE.

The PES for the chemical reactions can be classified as attractive or repulsive according to the values of the binding energy in Eqs. 4.1, 4.2. If there is an attraction between the monomers (the CO molecule and the metal atom) as they approach each other, then they bind and produce a complex with an energy less than the sum of the free monomers energies. Hence, the binding energy has a negative value and the PES is called an attractive PES. In the other case, if the monomers repel each other when they approach each other, they do not bind and the energy of the system become more than the sum of the free monomers energies. Hence, the values of binding energy is positive and no complex is formed. Thus, the PES is classified as a repulsive PES.

The PES is a conceptual tool to analyze the molecular geometry. Once the points of the PES are calculated, a few of them are classified into stationary points or saddle points. The stationary points are the energy minima that correspond to physically stable chemical species. The saddle points are the highest energy points along the path from one minimum to another, they correspond to the transition states of the chemical species.

4.1 2D-PESs of $\text{MCO}^{0,\pm}$

Foremost, The 2D-PES is plotted as a contour plot, a way to map a three dimensional surface into a two dimensional plane, to see how the binding energy value changes as a function of two variables (x: distance, y: angle). I called the upper half of the PES plot with positive angles as a carbon region, because the metal is near to the carbon atom based on Fig. 4.0.1, and the lower half with negative angles as oxygen region since the metal is near to the oxygen atom. In addition, the region with red contour lines (negative binding energy) is described as an attractive region and the region with blue contour lines (positive binding energy) is described as a repulsive region.

The 2D-PES of the neutral complexes, AuCO, AgCO, CuCO are shown in Figs. 4.1.1, 4.1.2, 4.1.3, respectively. They have attractive and repulsive regions and one minimum. Regarding the 2D-PES of AuCO complex, the carbon region is almost attractive region and the oxygen region is totally repulsive region. It has only one minimum in the carbon region around the angle ($\alpha = 72^\circ$) and distance ($d = 2.5 \text{ \AA}$) with binding energy -320 meV. This mean that gold atom binds with CO from carbon side and form a bent AuCO complex.

The PES of AgCO is replusive for the distances less than 3.5 \AA then it starts to be attractive. It has very shallow minimum at longe distance $d = 4.5 \text{ \AA}$ and $\alpha = 35^\circ$ with binding energy -12 meV. Due to the far position of the minimum and the low value in binding energy, this shallow minimum is called dispersive minimum, because it indicates a very weak binding that results from the dispersion interaction.

The PES of CuCO indicates that the interaction of the copper atom with CO is similar to the interaction of the gold atom with CO but slightly weaker. Thus, the carbon region is almost attractive region and the oxygen region is repulsive region. The attractive region has a minimum at $\alpha = 70^\circ$ and $d = 2.4 \text{ \AA}$ with a binding energy -240 meV. This means that the copper atom binds with CO molecule from carbon side and form a bent CuCO complex.

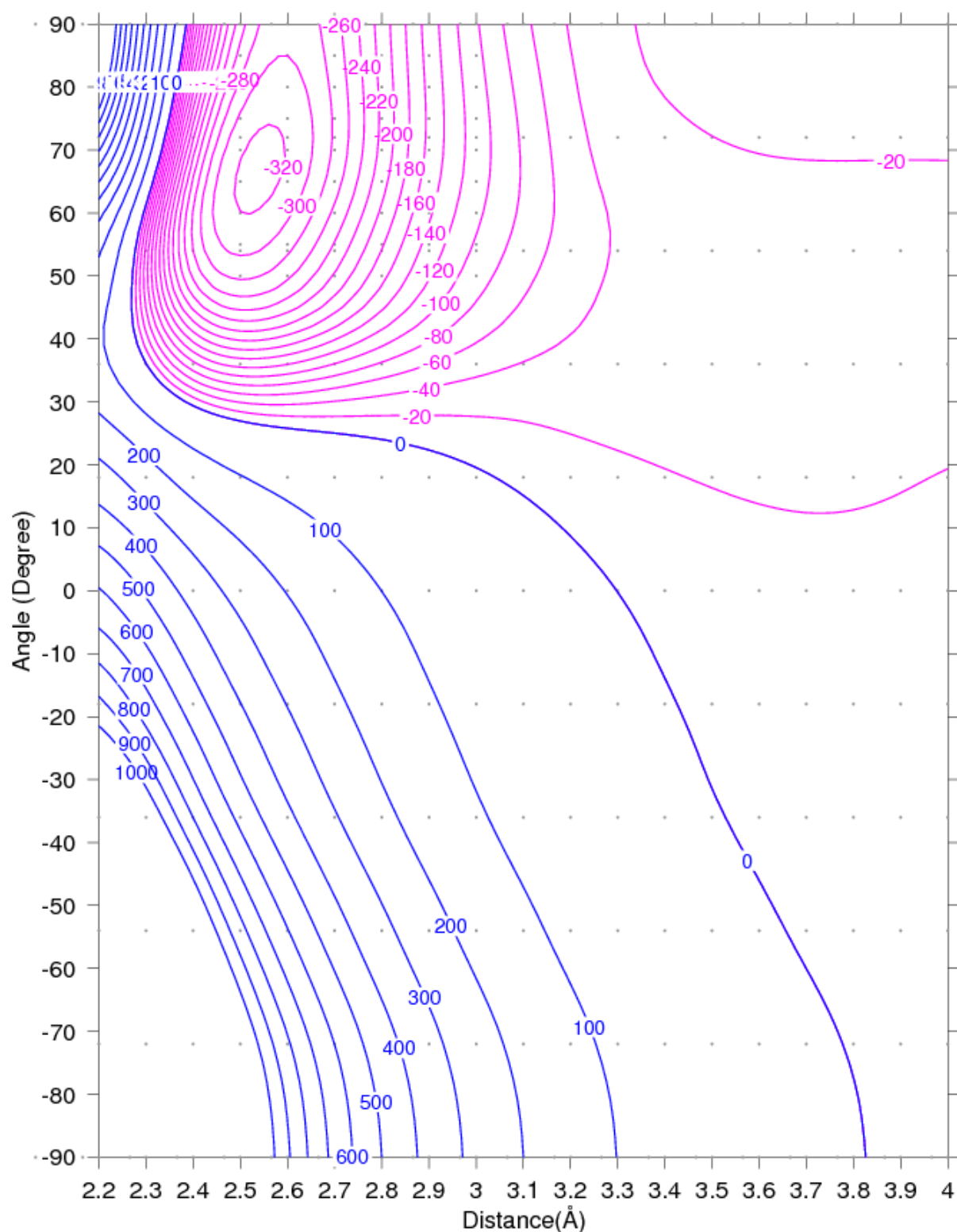


Figure 4.1.1: Counterpoise corrected binding energy surface of $\text{Au}(^2\text{S}) + \text{CO}(^1\Sigma^+) \rightarrow \text{AuCO}(^2\text{A}')$ as a function of the distance and the angle between Au atom and CO center as described in Fig. 4.0.1 using UCCSD(T)/Au=ECP60MDF-AVTZ, C=AVTZ, O=AVTZ. The dots represent the binding energy calculated at different geometries.

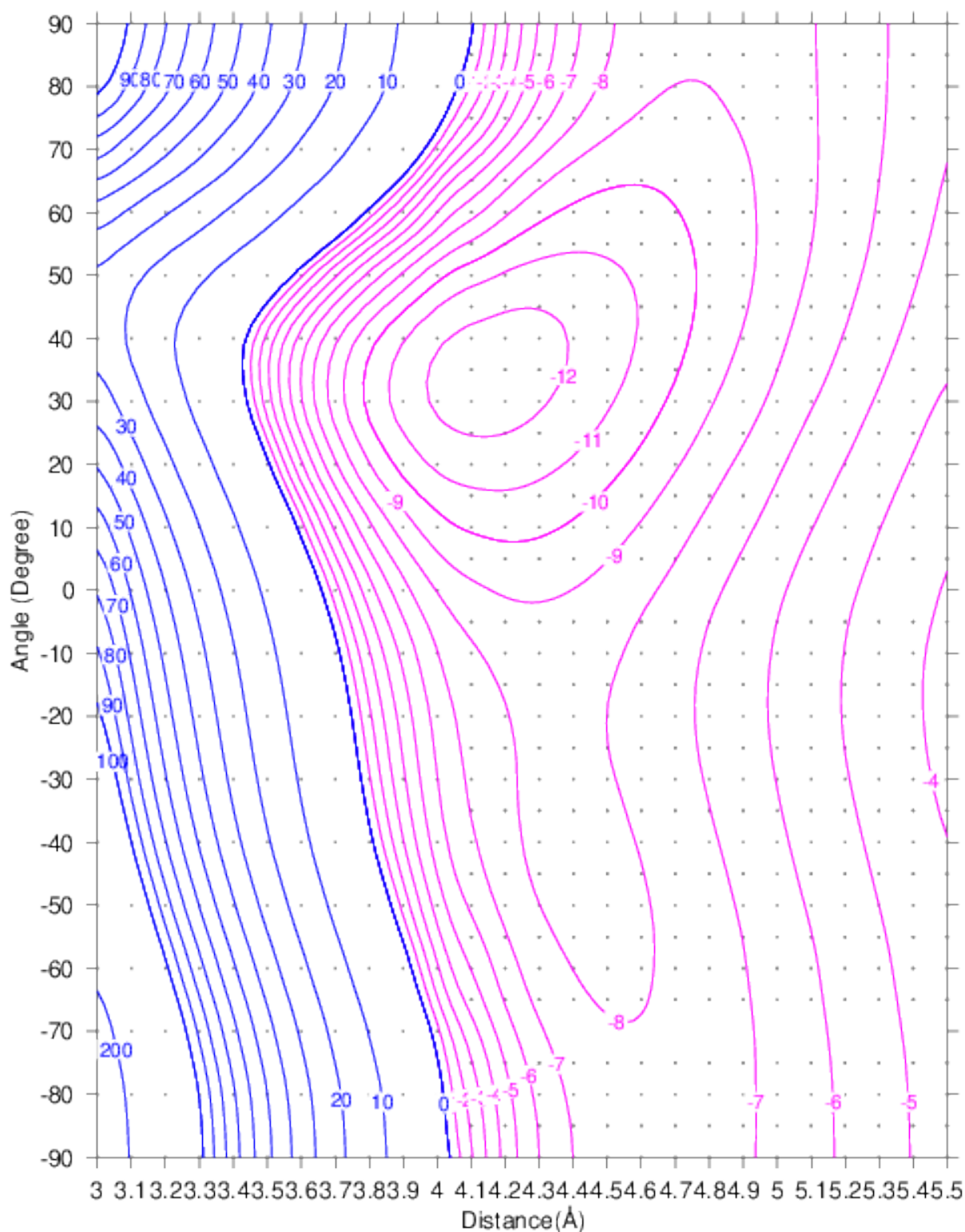


Figure 4.1.2: Counterpoise corrected binding energy surface of $\text{Ag}(^2S) + \text{CO}(^1\Sigma^+) \rightarrow \text{AgCO}(^2A')$ as a function of the distance and the angle between Ag atom and CO center as described in Fig. 4.0.1 using UCCSD(T)/Ag=ECP28MDF-AVTZ, C=AVTZ, O=AVTZ. The dots represent the binding energy calculated at different geometries.

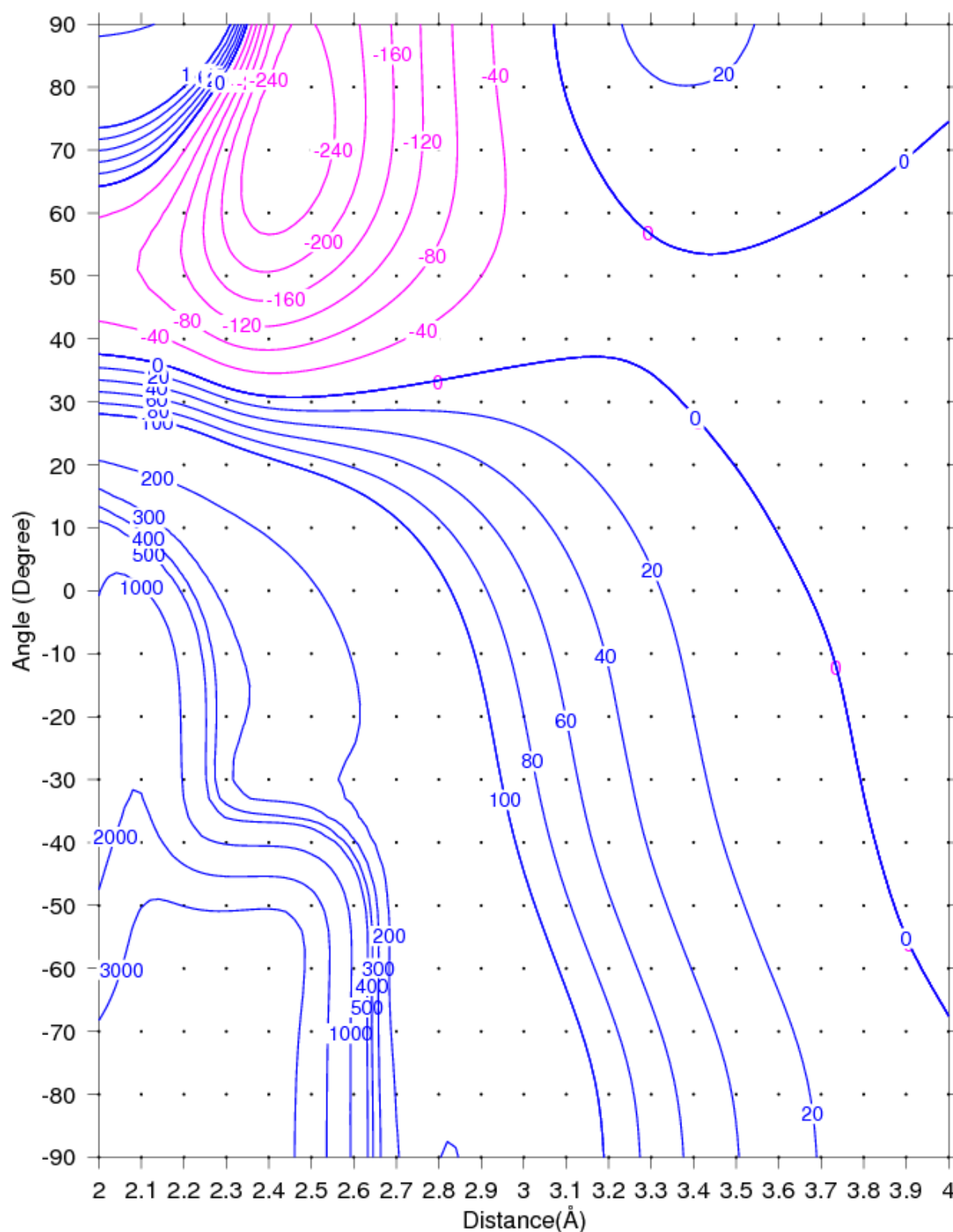


Figure 4.1.3: Counterpoise corrected binding energy surface of $\text{Cu}(^2\text{S}) + \text{CO}(^1\Sigma^+) \rightarrow \text{CuCO}(^2\text{A}')$ as a function of the distance and the angle between Cu atom and CO center as described in Fig. 4.0.1 using UCCSD(T)/Cu=ECP10MDF-AVTZ, C=AVTZ, O=AVTZ. The dots represent the binding energy calculated at different geometries.

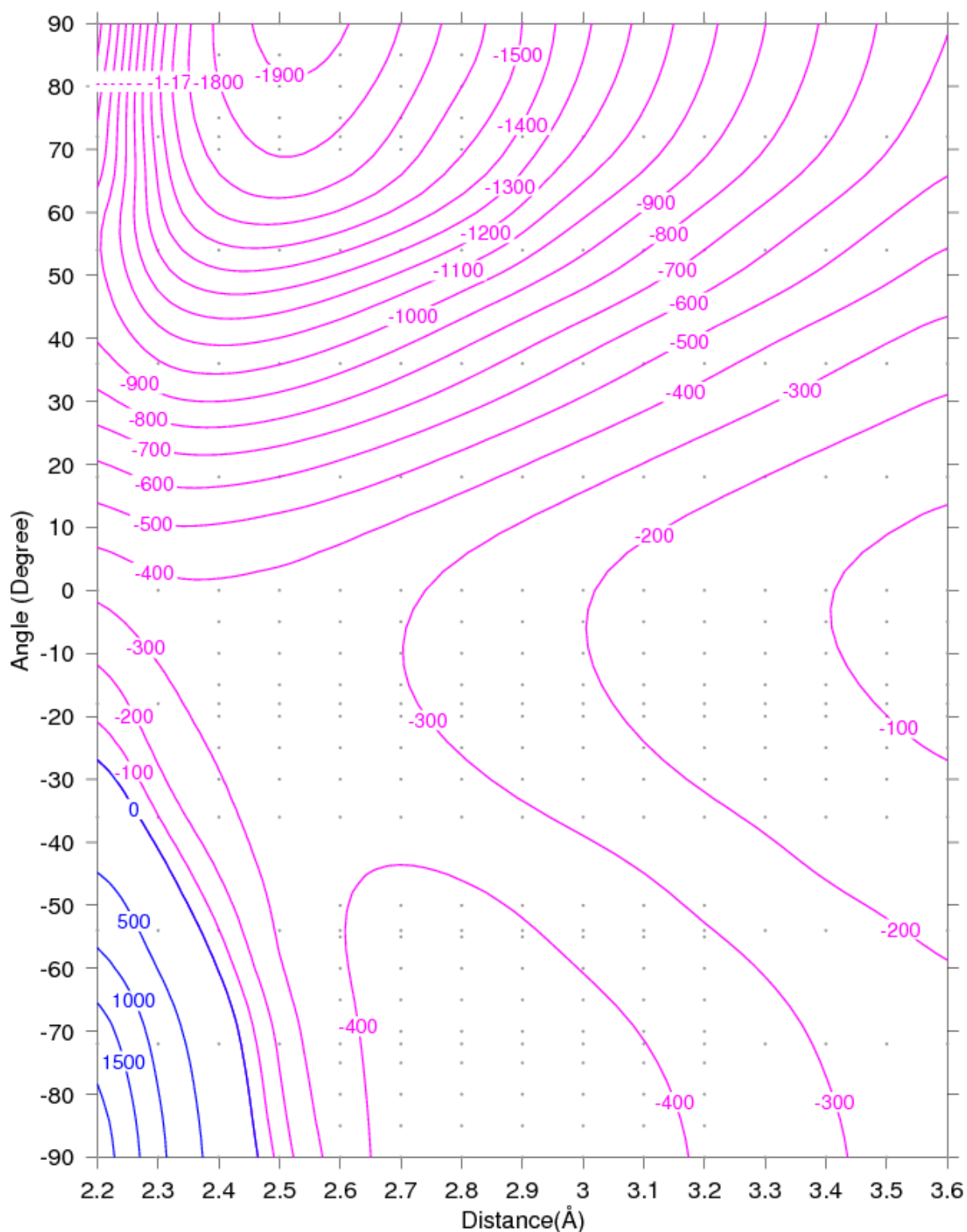


Figure 4.1.4: Counterpoise corrected binding energy surface of $\text{Au}^+(^1\text{S}) + \text{CO}(^1\Sigma^+) \rightarrow \text{AuCO}^+(^1\text{A}')$ as a function of the distance and the angle between Au^+ ion and CO center as described in Fig. 4.0.1 using UCCSD(T)/Au=ECP60MDF-AVTZ, C=AVTZ, O=AVTZ. The dots represent the binding energy calculated at different geometries.

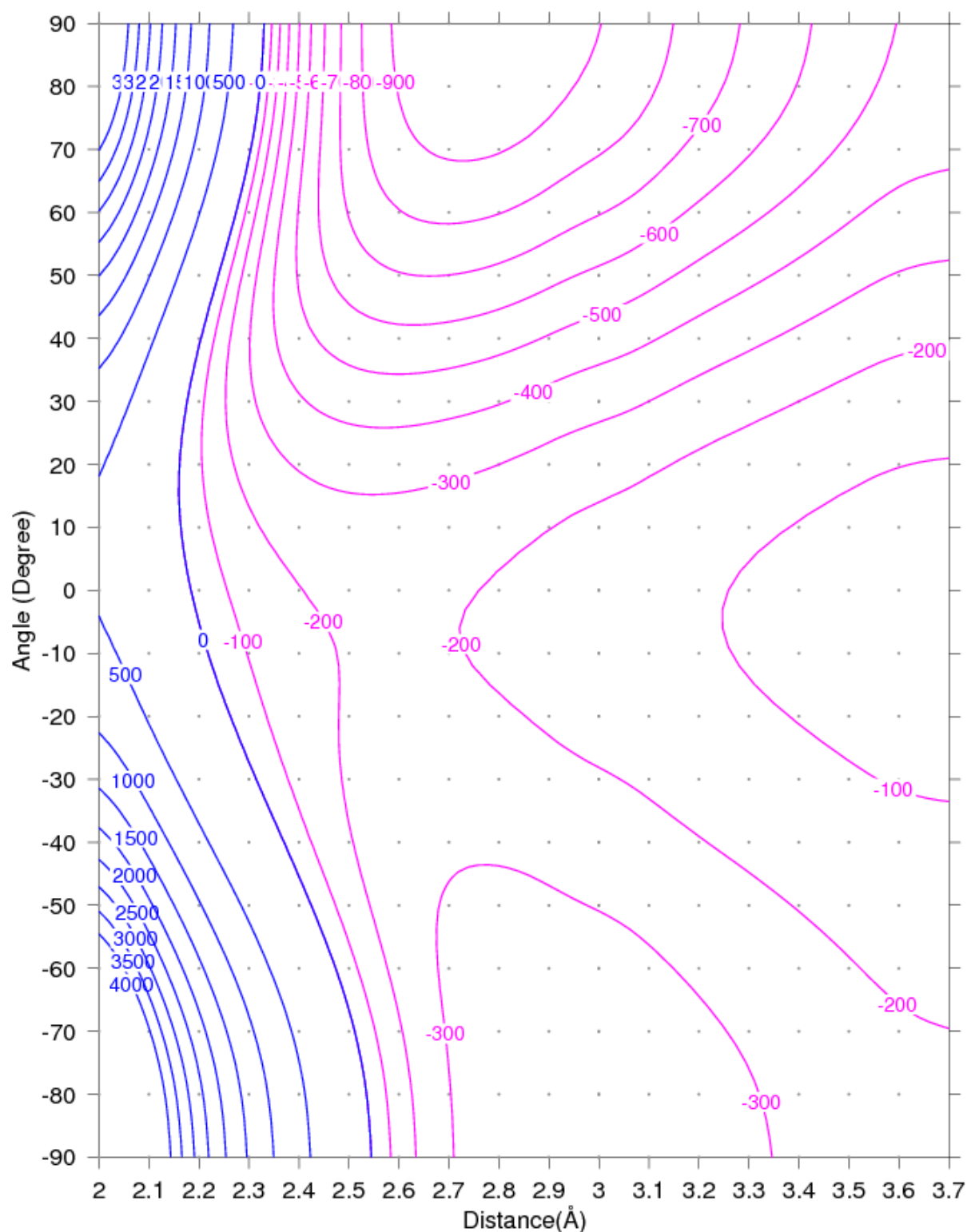


Figure 4.1.5: Counterpoise corrected binding energy surface of $\text{Ag}^+(^1S) + \text{CO}(^1\Sigma^+) \rightarrow \text{AgCO}^+(^1A')$ as a function of the distance and the angle between Ag^+ ion and CO center as described in Fig. 4.0.1 using $\text{UCCSD(T)/Ag=ECP28MDF-AVTZ}$, C=AVTZ , O=AVTZ . The dots represent the binding energy calculated at different geometries.

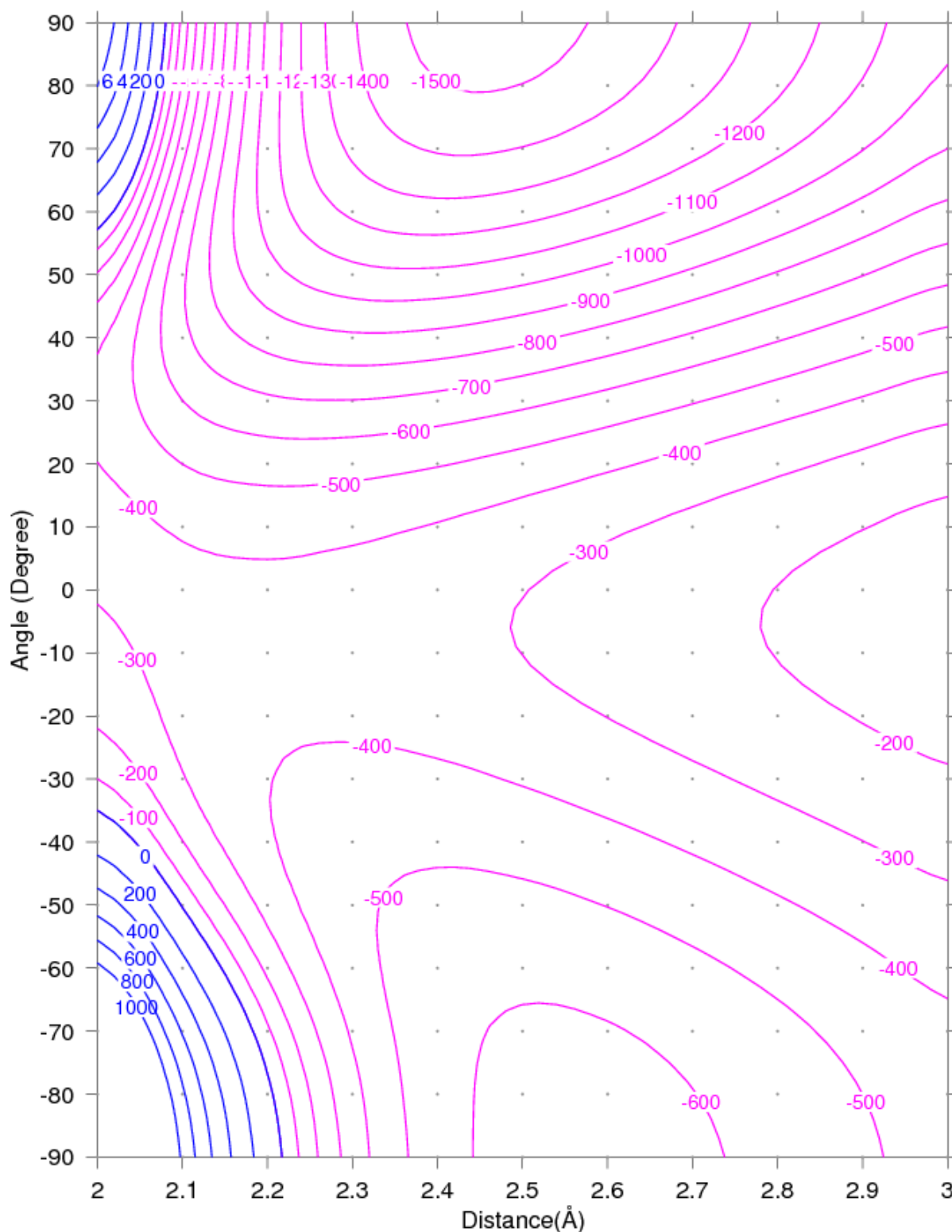


Figure 4.1.6: Counterpoise corrected binding energy surface of $\text{Cu}^+(^1S) + \text{CO}(^1\Sigma^+) \rightarrow \text{CuCO}^+(^1A')$ as a function of the distance and the angle between Cu^+ ion and CO center as described in Fig. 4.0.1 using UCCSD(T)/Cu=ECP10MDF-AVTZ, C=AVTZ, O=AVTZ. The dots represent the binding energy calculated at different geometries.

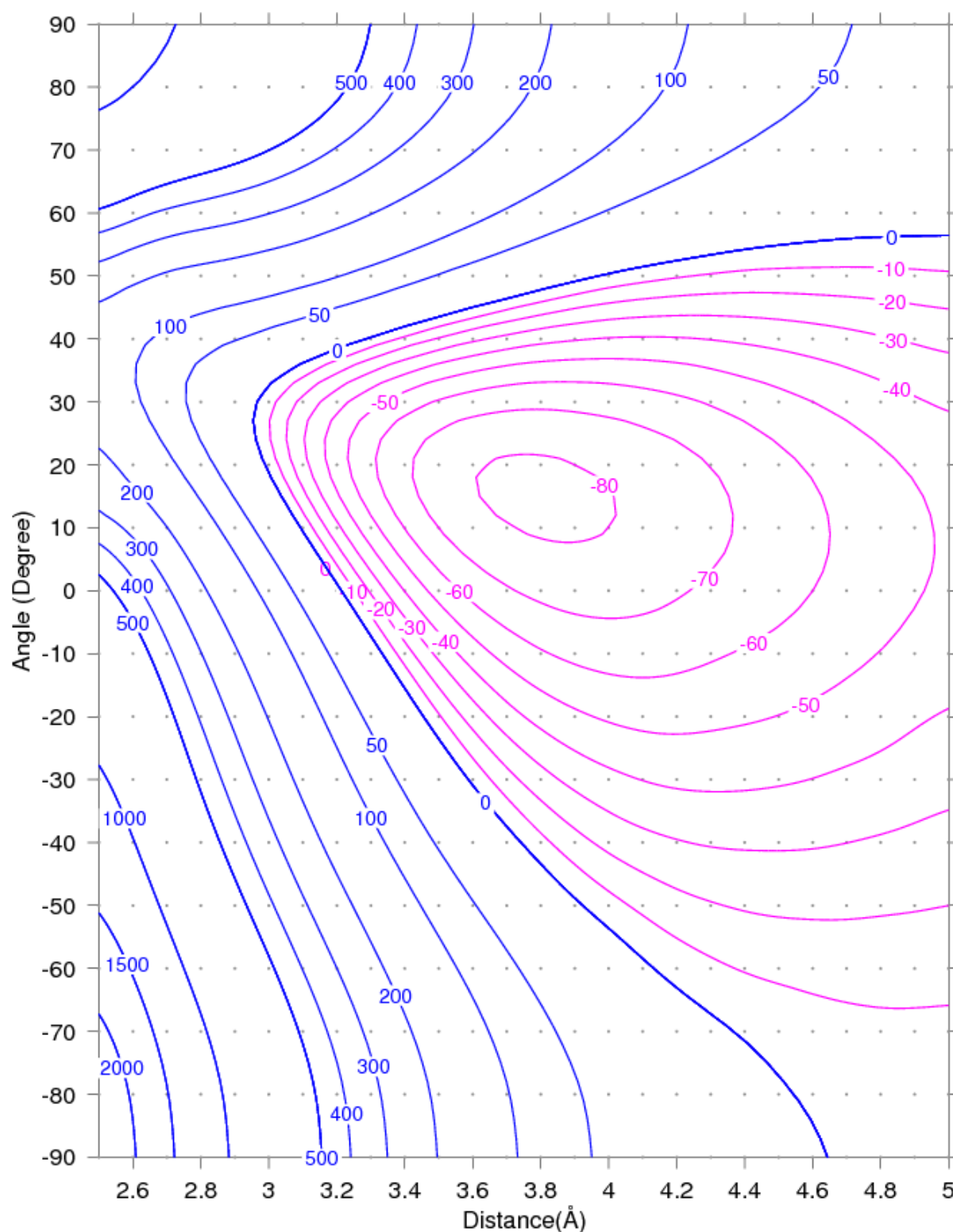


Figure 4.1.7: Counterpoise corrected binding energy surface of $\text{Au}^-(^1\text{S}) + \text{CO}(^1\Sigma^+) \rightarrow \text{AuCO}^-(^1\text{A}')$ as a function of the distance and the angle between Au^- ion and CO center as described in Fig. 4.0.1 using UCCSD(T)/Au=ECP60MDF-AVTZ, C=AVTZ, O=AVTZ. The dots represent the binding energy calculated at different geometries.

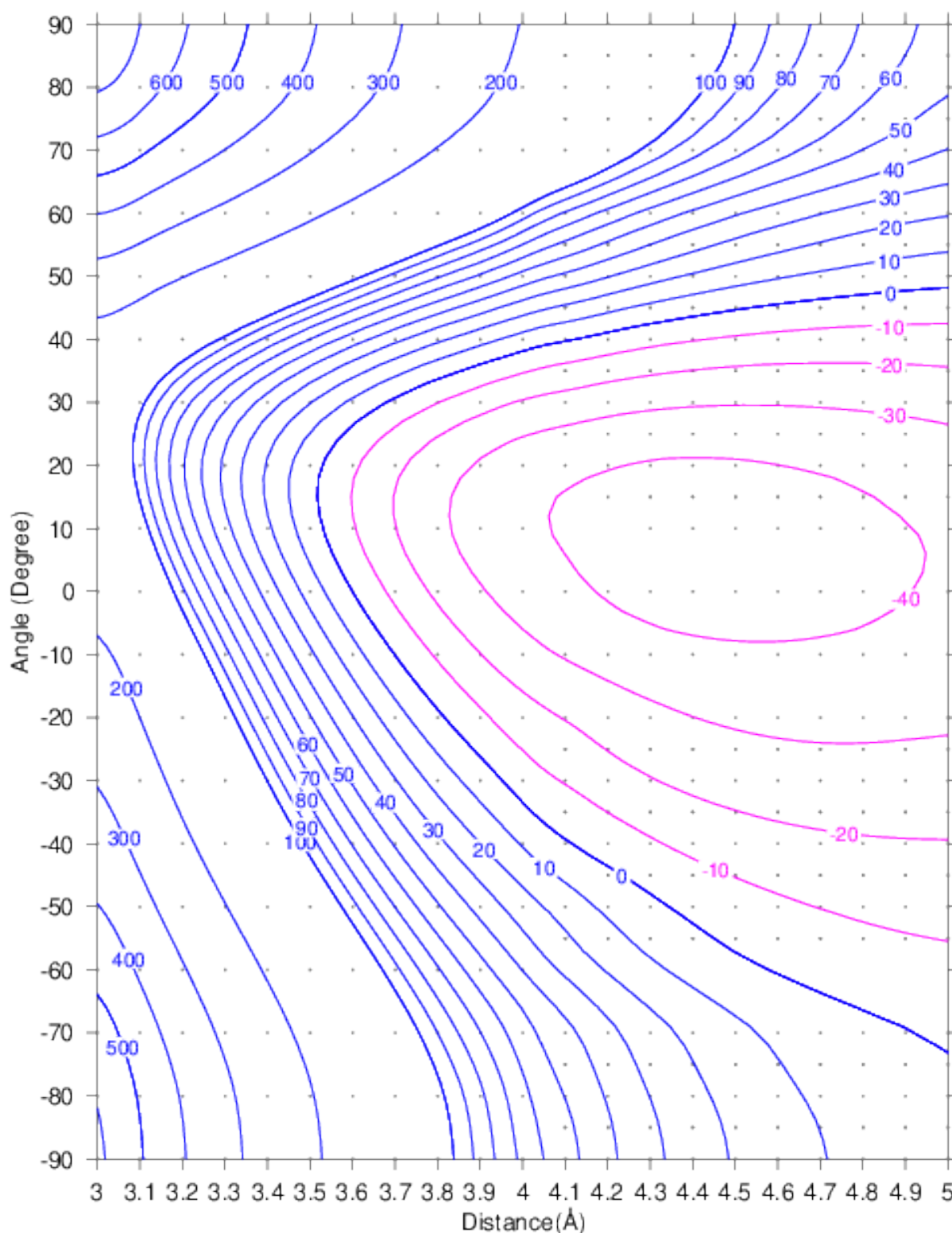


Figure 4.1.8: Counterpoise corrected binding energy surface of $\text{Ag}^-(^1\text{S}) + \text{CO}(^1\Sigma^+) \rightarrow \text{AgCO}^-(^1\text{A}')$ as a function of the distance and the angle between Ag^- ion and CO center as described in Fig. 4.0.1 using UCCSD(T)/Ag=ECP28MDF-AVTZ, C=AVTZ, O=AVTZ. The dots represent the binding energy calculated at different geometries.

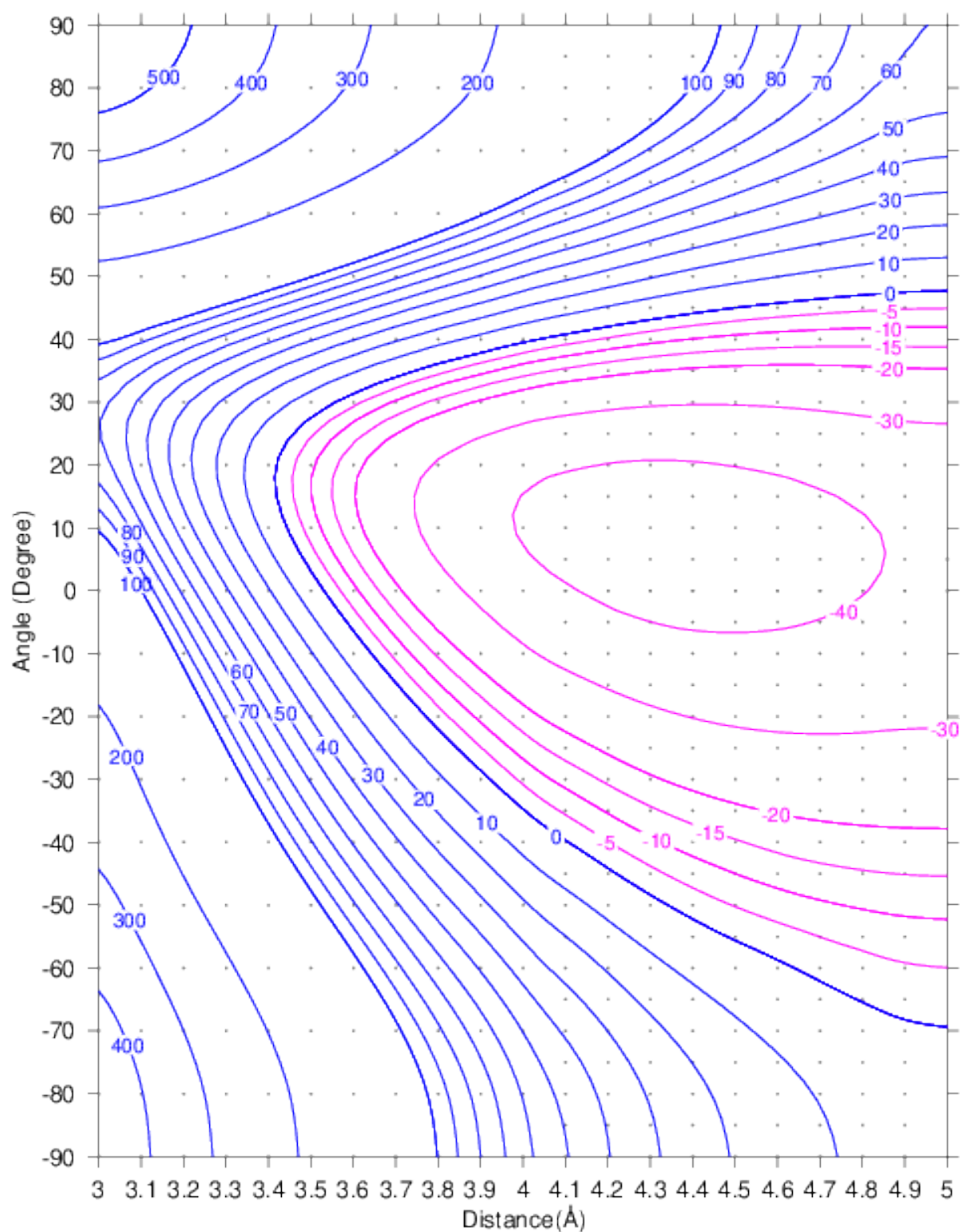


Figure 4.1.9: Counterpoise corrected binding energy surface of $\text{Cu}^-(^1\text{S}) + \text{CO}(^1\Sigma^+) \rightarrow \text{CuCO}^-(^1\text{A}')$ as a function of the distance and the angle between Cu^- ion and CO center as described in Fig. 4.0.1 using UCCSD(T)/Cu=ECP10MDF-AVTZ, C=AVTZ, O=AVTZ. The dots represent the binding energy calculated at different geometries.

In addition to the geometry analysis, the 2D-PES helps us to find the dissociation path that the complex follows to dissociate into its constituents. It is the minimum energy path that connects the minimum of the PES with the contour line of zero binding energy. This means that AuCO dissociate if the gold atom first bends to the angle 30° , then move away from the carbon atom. The CuCO complex dissociates by following the same path, too. But in AgCO case, the silver atom moves away from CO molecule without bending.

For the cationic carbonyl MCO^+ complexes, the PESs are shown in Figs. 4.1.4, 4.1.5, 4.1.6. The 2D-PES of AuCO cation shows that the interaction between the gold cation and the CO molecule is attractive over the whole the range of the parameter space, since all of the contours have negative binding energy. Furthermore, the PES has two minima (m_1, m_2) and a saddle point in between; the first minimum, m_1 , is in the carbon region at $\alpha = 90^\circ$ and $d = 2.5 \text{ \AA}$, with a binding energy of -1900 meV. This means that the gold cation binds with CO from the carbon side and forms a linear AuCO^+ complex. The second minimum, m_2 , is in the oxygen region at $\alpha = -90^\circ$ and $d = 2.6 \text{ \AA}$, with a binding energy of -400 meV. Hence, the gold cation binds with CO from the oxygen side and forms a linear AuOC^+ , too.

That means the gold cation binds with CO molecule either from the carbon side or from the oxygen side and forms a linear AuCO^+ or AuOC^+ complex, respectively. It binds much stronger from the carbon side, which means that the linear AuCO^+ is the stable complex while the linear AuOC^+ is a metastable complex. To transform AuOC^+ complex into the stable structure AuCO^+ , the AuOC^+ complex should pass through the saddle point and overcome the energy barrier of 100 meV. In addition, both complexes, AuCO^+ and AuOC^+ , dissociate into a neutral CO molecule and a gold cation when the gold cation rotates to be perpendicular to the CO molecule and then move away.

The PES of AgCO^+ is similar to the PES of AuCO^+ but weaker; the interaction of silver cation toward the CO molecule have nearly the same behavior but with weaker binding energy. It has two minima, m_1, m_2 , the first minimum is in carbon region at $\alpha = 90^\circ$ and $d = 2.7 \text{ \AA}$ with a binding energy of -900 meV. Hence, the silver cation binds with CO from the carbon side and forms a linear AgCO^+ complex. The second minimum is in the oxygen region at $\alpha = -90^\circ$ and $d = 2.7 \text{ \AA}$. Thus, the silver cation binds with CO molecule from oxygen side and forms a linear AgOC^+ complex.

This means that silver cation binds with CO either from the carbon side or from the oxygen side and forms linear AgCO^+ or AgOC^+ complexes, respectively. The linear AgCO^+ complex is more stable than the AgOC^+ complex and the energy barrier should be overcome to transfer the AgOC^+ to the AgCO^+ is about 120 meV. In addition, both complexes dissociate, like AuCO^+ and AuOC^+ , by bending the silver cation to be perpendicular to the CO molecule and then move away.

The interaction of copper cation towards the CO molecule have the same behavior as the gold and the silver cations, but the binding energy is weaker than gold cation and stronger than silver cation. Hence, the 2D-PES has two minima, m_1, m_2 , in carbon and oxygen regions, respectively. The first minimum at $\alpha = 90^\circ$ and $d = 2.4 \text{ \AA}$ with binding energy -1500 meV. The second minimum at angle $\alpha = -90^\circ$ and at distance 2.4 \AA with binding energy -600 meV. Thus, the copper cation binds with the CO molecule either from carbon side or from oxygen side and forms a linear complex, CuCO^+ or CuOC^+ , respectively. The CuCO^+ complex is more stable than CuOC^+ , and the energy barrier, that should be overcome to transform the metastable CuOC^+ to the most stable linear CuCO^+ , is about 240 meV, which is higher than the barrier of AgCO^+ and AuCO^+ . Moreover, both complexes dissociate if the copper cation bends to be perpendicular to the CO molecule and then go away.

Regarding the interaction of CO with coinage metals anions, the PESs of AuCO^- , AgCO^- , CuCO^- are shown in Figs. 4.1.7, 4.1.8, 4.1.9. The PES of AuCO^- is repulsive until $d = 3 \text{ \AA}$ then it starts to be attractive. It has a minimum around $d = 4 \text{ \AA}$ and $\alpha = 15^\circ$ with binding energy -80 meV. Hence, the gold anion binds with the CO molecule from carbon side and forms a bent AuCO^- complex. In addition, the AuCO^- complex dissociates if the gold anion rotates either to $\alpha = 40^\circ$ or $\alpha = -20^\circ$ and then move away.

The interaction of silver and copper anions with the CO molecule is weaker than the interaction of gold anion but the behavior is similar; the PESs of AgCO^- and AuCO^- are repulsive until $d = 3.5 \text{ \AA}$, $d = 3.7 \text{ \AA}$, respectively then they start to be attractive. Both have a wide minimum: The borders of the minimum are nearly from $d = 4 \text{ \AA}$ to $d = 4.9 \text{ \AA}$ and from $\alpha = 20^\circ$ to $\alpha = -5^\circ$ with binding energy -40 meV. Hence, if the anion, Ag^- or Cu^- , is perpendicular to the CO molecule, they bind with each other weakly and form AgCO^- or AuCO^- complex, respectively. In addition, both complexes, AgCO^- and

CuCO^- , dissociates if the anion rotates either to $\alpha = 40^\circ$ or $\alpha = -40^\circ$ and then move away.

In summary, the 2D-PESs of MCO have attractive and repulsive regions and one minimum; the attractive region of AuCO and CuCO are localized in carbon region and the minimum occur at short distances, 2.5 Å, 2.4 Å, respectively. While in AgCO case, the attractive region is spread over the entire range of α and $d \geq 4$ Å.

The 2D-PESs MCO^+ are attractive over the whole range of parameter space and have two minima. The minimum in carbon region have stronger binding energy than the minimum in oxygen region. Hence each cation binds with the CO molecule either from carbon side or from oxygen side, and forms a stable linear complex MCO^+ or a metastable linear complex MOC^+ . In addition, all the positive charged complexes dissociate if the cation bends to be in perpendicular position to the CO molecule and then go away. The only difference in the cations behavior is the strength of binding energy which is ranked according to the binding strength at the first minimum and second minimum as gold > copper > silver and copper > gold > silver, respectively.

The 2D-PESs of the MCO^- complexes are similar, the attractive region occurs when the anion is nearly perpendicular to the CO molecule and is at $d \geq 4$ Å. This mean all the anion have a dispersive minimum, thus, the negative charged complexes are weakly bound.

In conclusion, the CO molecule binds with the neutral, cation and anion of coinage metals atom from carbon side and the structure stability and the binding strength is affected by the type and the charge of the coinage metals atoms. The neutral and negative charge complexes have bent geometry while the positive charged complexes have linear geometry. In addition, the binding energy increases as the charge of coinage metal increases. As we saw, the binding energies of the negative charged complexes are the weakest then it become stronger in the neutral complexes and then much stronger in the positively charged complexes. Regarding the effect of the type of elements, the binding energies are ranked for all type of charge as the followig $\text{AuCO} > \text{CuCO} > \text{AgCO}$.

4.2 Electronic structure of coinage metals carbonyl

To know why CO molecule binds with gold and copper stronger than silver and why the negative charged complexes are weakly bound, a full geometry optimization and frequency calculation was performed using the geometry at the minimum of each PES as initial guess. Then, the counterpoise corrected binding energy is calculated for each optimized structure using Eqs. 4.1, 4.2. The optimized bond parameters and the binding energy, E_{CP} are listed in Tab. 4.2.1, and the normal modes frequencies and the CO frequency shift are listed in Tab. 4.2.2.

Molecular state	r_{MC} (Å)	r_{CO} (Å)	$\angle MCO$ Degree	BSSE meV	ΔZPE meV	$E_{CP+\Delta ZPE}$ meV
AuCO ⁻ (¹ A')	3.593	1.139	98.1	-10.72	5.3	-76.7
AuCO(² A')	2.018	1.143	148.0	-7.2	27.2	-319.1
AuCO ⁺ (¹ A ₁)	1.950	1.124	180.0	-49.0	68.8	-1890.9
AgCO ⁻ (¹ A')	4.229	1.137	93.1	-5.8	-0.2	-45.1
AgCO(² A')	3.665	1.136	120.2	-6.1	0.2	-11.8
AgCO ⁺ (¹ A ₁)	2.182	1.124	180.0	-27.1	49.5	-957.7
CuCO ⁻ (¹ A')	4.083	1.138	94.3	-7.7	9.8	-58.2
CuCO(² A')	1.880	1.142	154.2	-58.6	27.2	-261.3
CuCO ⁺ (¹ A ₁)	1.887	1.124	180.0	-35.9	64.5	-1494.0
	r_{MO}	r_{CO}	$\angle MOC$			
AuOC ⁺ (¹ A ₁)	2.255	1.148	180.0	-19.7	1.9	-509.2
AgOC ⁺ (¹ A ₁)	2.351	1.145	180.0	-24.7	18.8	-488.2
CuOC ⁺ (¹ A ₁)	1.987	1.149	180.0	-24.2	26.6	-642.5

Table 4.2.1: The optimized bond parameters of MCO^{0,±} and MOC⁺ with M: Au, Ag, Cu. The r_{M-O} and $\angle MNO$ are different than the angle (α) and the distance (d) in Fig. 4.0.1. The basis set superposition error (BSSE), zero point energy (ZPE) and the counterpoise ZPE corrected binding energy using UCCSD(T)/ECP(60,28,10)MDF-AVTZ are given.

At the beginning, let's look at the neutral complexes. The three complexes have bent geometry as predicted in the PES, the M-C bond distance in AgCO complex is larger

than in AuCO and CuCO complexes, the CO bond length in AgCO is the same as the free CO while in AuCO and CuCO is slightly longer than the free CO. That's mean the interaction between Ag and CO is much weaker than the interaction between Au, Cu and CO.

Molecular state	C-O stretching	M-C stretching	M-C-O bending	CO shift
	cm ⁻¹	cm ⁻¹	cm ⁻¹	
AuCO ⁻ (¹ A')	2118.3	110.6	39.2	-25.0
AuCO(² A')	2057.5	343.4	188.8	-85.8
AuCO ⁺ (¹ A ₁)	2251.5	381.5	309.6	+108.3
AgCO ⁻ (¹ A')	2131.9	78.1	27.0	-11.4
AgCO(² A')	2140.2	37.8	17.3	-6.1
AgCO ⁺ (¹ A ₁)	2244.7	244.5	226.5	+101.4
CuCO ⁻ (¹ A')	2129.0	83.2	29.2	-14.3
CuCO(² A')	2064.9	342.9	173.9	-78.4
CuCO ⁺ (¹ A ₁)	2250.0	361.6	289.7	+106.7
	C-O stretching	M-O stretching	M-O-C bending	
AuOC ⁺ (¹ A ₁)	2058.83	192.9	101.6	-84.4
AgOC ⁺ (¹ A ₁)	2074.7	173.7	98.9	-68.5
CuOC ⁺ (¹ A ₁)	2060.0	262.7	125.1	-83.3

Table 4.2.2: The vibrational frequencies of MCO^{0,±} and MOC⁺ with M: Au, Ag, Cu. The CO shift is calculated as a difference of C-O stretching frequency and the free CO frequency (2143.3 cm⁻¹) using UCCSD(T)/ECP(60,28,10)MDF-AVTZ.

To know the nature of the binding between the coinage metals and CO, I have looked at the molecular orbitals and at the Mulliken population analysis, see Tab. 6.0.1 in the Appendix. The canonical molecular orbital diagram of the AuCO complexes is shown in Fig. 4.2.1, the CuCO complex have the same pattern but different energies while the AgCO complex no molecular orbital diagram is drawn because there is no overlap between the Ag atomic orbitals and the CO molecular orbitals.

It is clear that number of electrons in bonding orbital is more than in antibonding orbital by one, which mean that AuCO and CuCO complexes have a bond order of 0.5. In both complexes, the HOMO consists from an antibonding combination of metal (s) orbital and

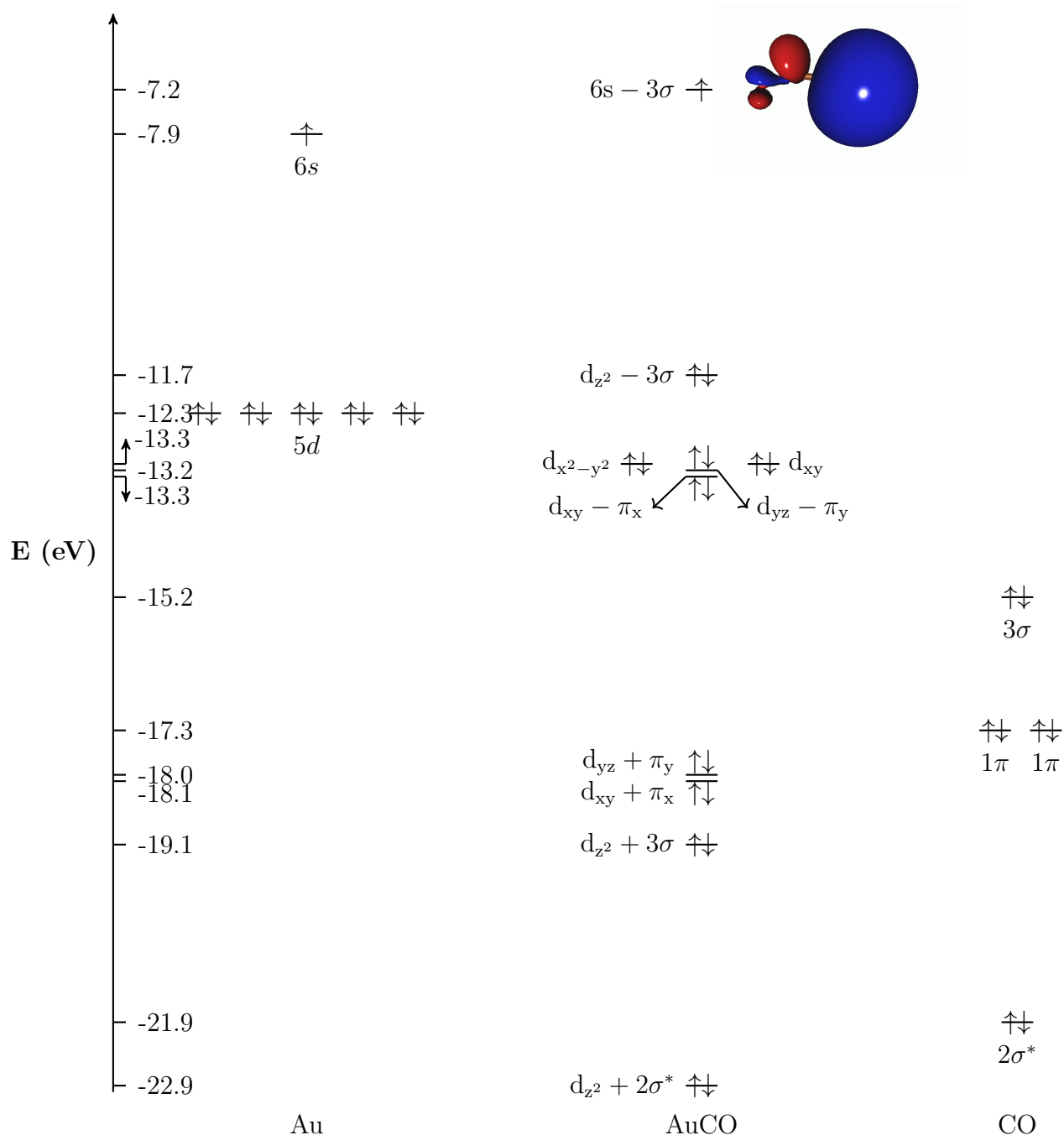


Figure 4.2.1: Energy level diagram for canonical valence molecular orbitals of AuCO complex ($^2A'$) using RHF/AVTZ. The CO molecular orbitals have the same labels as in Fig. 3.1.1. The molecular orbital occupation depending on C_s point group is: $(1a')^2(2a')^2(1a'')^2(3a')^2(2a'')^2(4a')^2(3a'')^2(5a')^2(6a')^2(7a')^1$. The highest occupied molecular orbital (HOMO) consists mainly from the 6s gold atomic orbital (The gold atom on the right and the CO unit on the left, the isocontour is 0.025).

CO (3σ) orbital. In addition, the charge analysis shows that the metal atom in AuCO and CuCO is negatively charged and the charge separation in $Au^{-\delta}CO^{+\delta}$ (0.45 electrons) is much larger than in $Cu^{-\delta}CO^{+\delta}$ (0.06 electrons). This means that the AuCO complex

have a dative bond and CuCO have covalent bond, and there is very small van der Waals interaction between CO and Ag atom. Therefore, the AuCO complex has the strongest binding energy, then the CuCO complex and the AgCO complex is the weakest.

The vibrational frequencies of MCO complexes follow the same trend; the C-O stretching frequency is the highest, then the M-C stretching frequency and the lowest is the M-C-O bending frequency. This emphasizes that the CO bond is much stronger than the M-C bond. Furthermore, the red shift in the CO stretching frequency in AuCO and CuCO can be ascribed to the σ donation from the ligand (CO) towards the metal.

About the positive charged complexes, they have two linear structures, MCO^+ and MOC^+ , see lower part of Tabs. 4.2.1, 4.2.2. The MCO^+ are more stable than the neutral complexes because the interatomic distance between the metal and the carbon is shorter than the corresponding ones in the neutral complexes, and their binding energies are larger in magnitude than the neutral complexes by at least one order of magnitude. This can be explained from molecular orbital point of view; the MCO^+ have a closed shell electron configuration and their molecular orbitals have the same pattern as the neutral complexes which shown in Fig. 4.2.1 but without an electron in $6s - 3\sigma$ orbital, therefore, the positive complexes have bond order of 1.

The MCO^+ has four vibrational frequencies, C-O stretching, M-C stretching and two degenerate M-C-O bending modes. The C-O stretching frequency is larger than the free CO frequency because the CO bond length in the MCO^+ is shorter than the free CO bond length which lead to blue shift in CO stretching frequency.

About the MOC^+ complexes, the bonds M-O and C-O are longer than the M-C and C-O in MCO^+ and the binding energies are weaker than the MCO^+ complexes. Because the overlap between d_{z^2} and 3σ is bigger if it occur from carbon side than oxygen side. Thus, the molecular orbitals built from the combination of metal (d_{z^2}) and CO (3σ) have lower energy in MCO^+ than in MOC^+ . Therefore, the MCO^+ complexes have stronger binding energy than the MOC^+ complexes. Based on the elongation of CO bond in MOC^+ complexes, the C-O stretching frequency becomes less, hence, the MOC^+ complexes have a red shift in the CO frequency.

Regarding the MCO^- complexes, the interatomic distance between the carbon and the

metal are longer than in the neutral and the positive charged complexes and the CO bond length and the C-O stretching frequency is nearly the same as the free CO. Moreover, there is no overlap between the anion and the CO orbitals. Therefore, the van der Waals forces are responsible for the long range attraction between the anion and the CO molecule. Hence, the MCO^- complexes have weak binding energies.

In conclusion, the MCO^+ has the strongest binding energy because they have bond order of one, then comes the MCO complexes which have bond order of 0.5. The MCO^- have no bond. In addition, the CO stretching frequency goes from blue shift to red shift when moving from positively charged complexes to the neutral complexes.

4.3 Potential energy surface of M_2CO

In order to see how does the binding energy change when the number of coinage metal atoms increases to two atoms, I assume different configurations to bind the CO molecule with the metal dimer either from the carbon side or from the oxygen side, see Tab. 4.3.1.



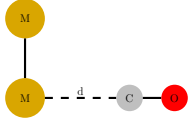
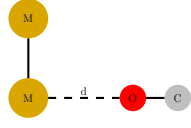
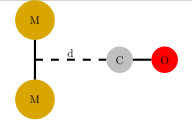
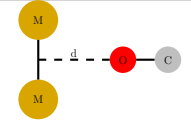
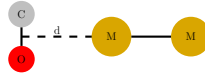
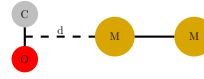
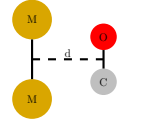
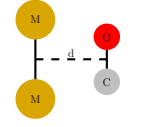
Shape	$M_2 - CO$	$M_2 - OC$
Linear		
L-shape		
T-shape		
CO-hat		
Parallel		

Table 4.3.1: Different configurations of $M_2 - CO$ and $M_2 - OC$, where M: Au, Ag, Cu.

Then I calculate the counterpoise corrected binding energy of the M_2CO and M_2OC complexes at different distance (d) with considering the metal dimer ground state ($^1\Sigma$) as the first monomer and the CO molecule ($^1\Sigma$) as the second monomer. The one dimension PESs plots are collected in Fig. 4.3.1. It contains the PESs of the binding energy for each complex in different configurations.

First, let us look at the binding of the gold dimer ($^1\Sigma$) with CO molecule ($^1\Sigma$), it is clear in Fig. 4.3.1, that the gold dimer binds with CO molecule from carbon side much stronger than the oxygen side. In addition the best configuration to have a stable complex is the linear configuration for both carbon and oxygen binding. Then come the CO-hat configuration. The other configurations have weaker binding energy, see Tab. 4.3.2. Furthermore, the binding energy of the linear M_2CO complex is three times greater than binding energy of AuCO complex.

Regarding the silver dimer, the best configuration to bind the CO molecule with the silver dimer is the linear configuration and it will much stronger when it binds from carbon side. The best second configuration is the parallel one not the CO-hat as for the gold dimer. The other configurations have very very weak binding energy. What is noticeable is that the CO binds with silver dimer much stronger than with the silver atom; where it binds at short distance with binding energy 30 times greater than the binding energy with silver atom.

About copper, the interaction of copper dimer with CO molecule is stronger than the silver dimer but weaker than the gold dimer in linear configurations only. But the behavior is different for the other configurations, the copper dimer attracts the CO weaker than silver and becomes repulsive in T-shape configuration. This mean that the binding energies of $M_2 - CO$ have the same trend as MCO if M_2 binds with CO in linear geometry, $Au_2 - CO < Cu_2 - CO < Ag_2 - CO$.

Returning back to $Au_2 - CO$, because the binding energy of CO-hat is near to the linear $Au_2 - OC$, I calculate 2D-potential energy surface of the binding energy in which the $Au_2 - CO$ complex transforms from the linear $Au_2 - CO$ to the linear $Au_2 - OC$ by passing through CO-hat depending on the geometry of Fig. 4.3.2.

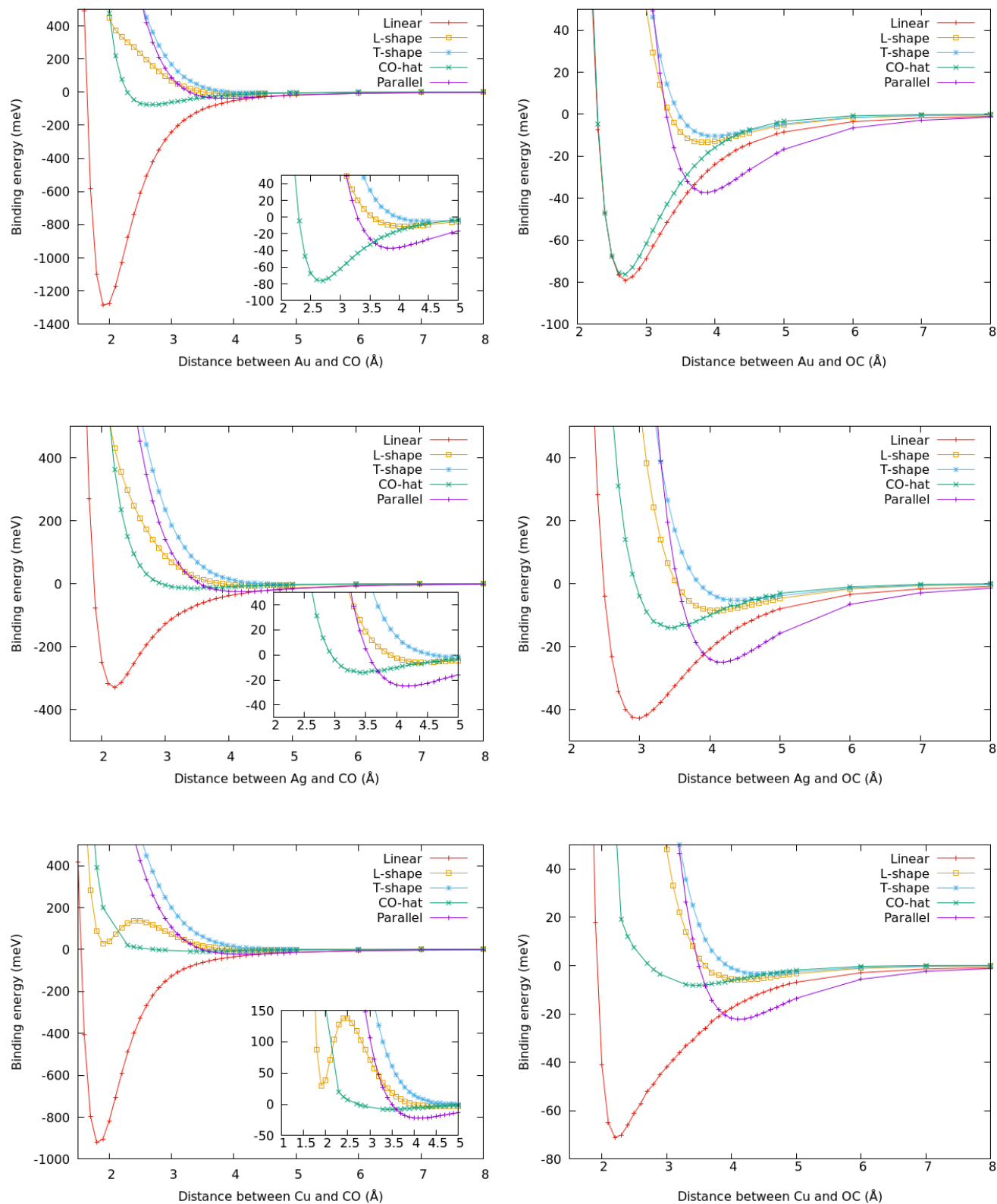


Figure 4.3.1: Counterpoise corrected binding energy of $M_2(^1\Sigma) + CO(^1\Sigma^+) \rightarrow M_2 - CO$, with M : Au, Ag, Cu as a function of the distance between C atom or O atom and coinage metals dimer as described in the Tab.4.3.1 using UCCSD(T)/ECP(10,28,60)MDF-AVTZ,C=AVTZ,O=AVTZ. The subfigures on the right are zoom in for M-C distance.

	$M_2 - CO$					
	Gold		Silver		Copper	
	E_{CP} meV	d_{Au_2-C} Å	E_{CP} meV	d_{Ag_2-C} Å	E_{CP} meV	d_{Cu_2-C} Å
Linear	-1282.8	1.9	-329.0	2.2	-921.2	1.8
L-shape	-11.1	4.1	-6.0	4.3	-3.3	4.5
T-shape	-4.9	4.5	-1.4	5.0	-	-
CO-hat	-76.2	2.7	-14.0	3.4	-8.1	3.5
Parallel	-37.3	3.9	-24.9	4.2	-22.2	4.1
	$M_2 - OC$					
	E_{CP}	d_{Au_2-O}	E_{CP}	d_{Ag_2-O}	E_{CP}	d_{Cu_2-O}
	meV	Å	meV	Å	meV	Å
Linear	-79.1	2.7	-42.7	3.0	-71.0	2.2
L-shape	-13.4	3.8	-8.5	4.1	-5.8	4.1
T-shape	-10.4	4.0	-5.3	4.4	-	-

Table 4.3.2: Counterpoise corrected binding energy of $M_2 - CO$ and $M_2 - OC$, where M: Au, Ag and Cu for different configurations and the corresponding distance between the metal and carbon or oxygen atoms based on the geometry described in Tab.4.3.1 calculated by UCCSD(T)/ECP(60, 28, 10)MDF-AVTZ. The CO-hat and parallel configurations are the same for $M_2 - CO$ and $M_2 - OC$.

The 2D-PES of $Au_2 - CO$ is shown in Fig. 4.3.2. It has two minima (m_1, m_2) , the first one at $d = 2.5$ Å and $\alpha = 0^\circ$ when the $Au_2 - CO$ have linear geometry, the second minimum at $d = 3.1$ Å and $\alpha = 180^\circ$ at the linear geometry $Au_2 - OC$. In addition the CO-hat geometry regarded a transition state and the energy barrier should the linear $Au_2 - OC$ overcome to transform into the stable $Au_2 - CO$ is about 30 meV.

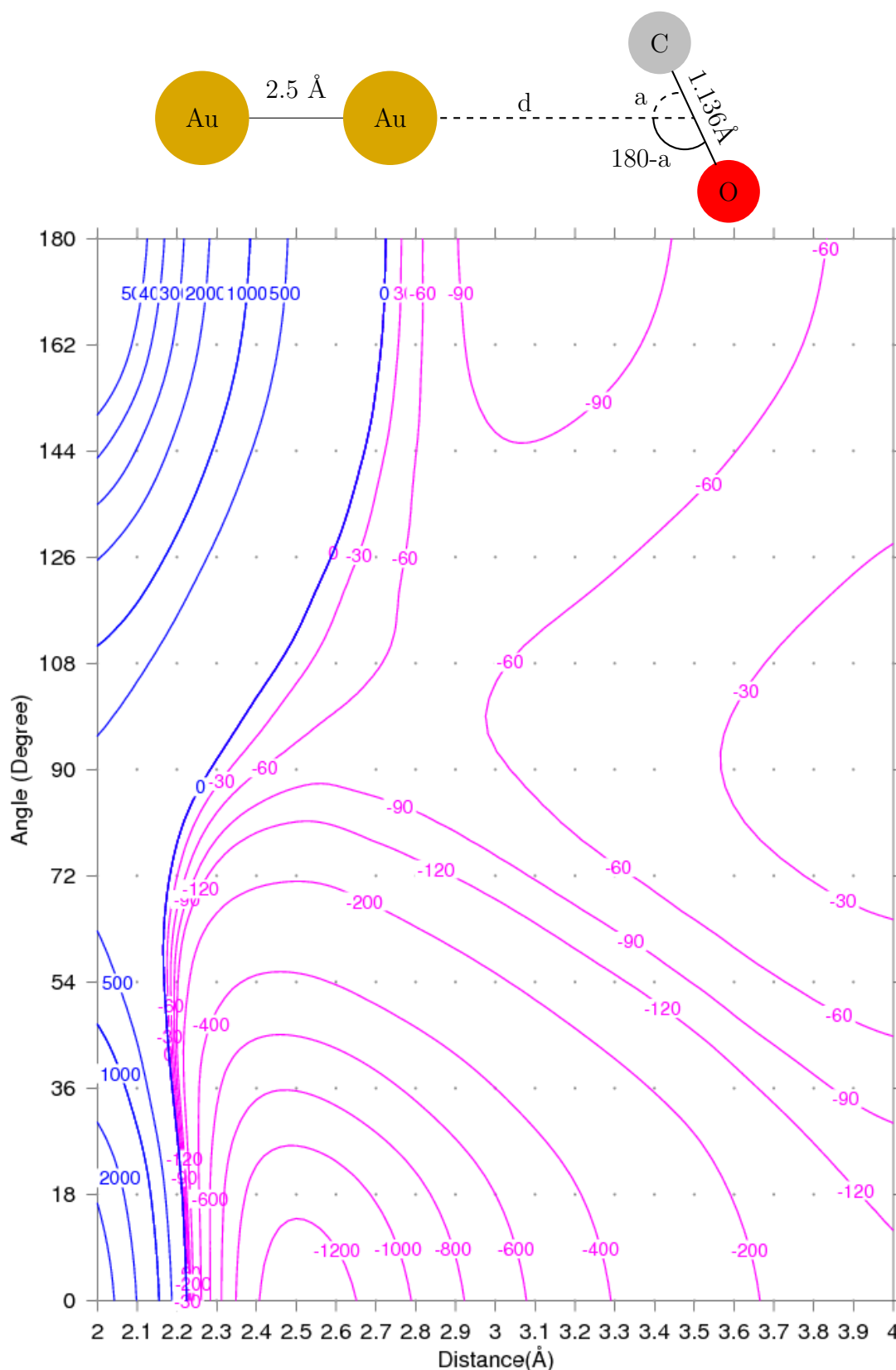


Figure 4.3.2: Counterpoise corrected binding energy surface of Au_2CO as a function of the distance between Au atom and CO center and the angle as described in the geometry at the upper part of the figure (when $a = 0^\circ$ the geometry is linear Au_2CO , $a = 90^\circ$ it is CO hat, $a = 180^\circ$ the geometry is linear Au_2OC) using UCCSD(T)/Au=ECP60MDF-AVTZ, C=AVTZ, O=AVTZ. The dots represent the binding energy calculated at different geometries.

CHAPTER 5

Two dimensions potential energy surfaces of coinage metals nitrosyl complexes

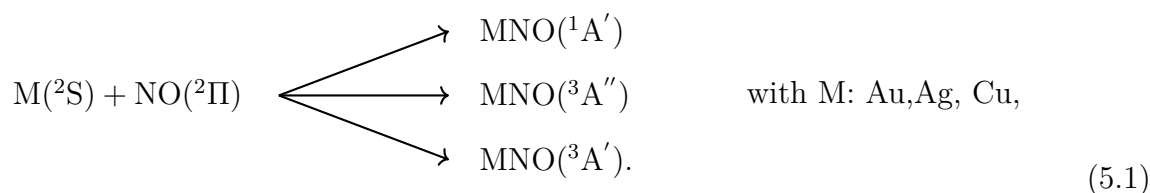
Coinage metals mononitrosyl complexes are compounds that contain one NO as a coordinated ligand (M-NO, M: Au, Ag, Cu). These complexes are formed by the interaction of the ground state of NO($^2\Pi$) with the ground state of the coinage metals atoms or ions, 2S or 1S , respectively. In analogy to the CO-case, I have calculated two-dimensional potential energy surfaces (2D-PESs) that describe the adsorption of the NO molecule on the coinage metals atoms and ions. The surfaces were calculated using the same geometry of MCO $^{0,\pm}$, see Fig. 4.0.1, with NO molecule instead of the CO molecule, with keeping the NO bond length fixed to its equilibrium value 1.1569 Å, that is calculated by CCSD(T)/AVTZ.

The calculations were performed by applying the symmetry point group, C_S , to be able to distinguish between the complex states that result from the combination of the space and spin symmetry of the monomers according to the Wigner-Witmer rules[209].

In the following sections, the 2D-PESs of different states for the neutral and charged coinage metals nitrosyl are discussed together with the optimized parameters, binding energy and the vibrational frequencies of each complex.

5.1 2D-PESs of MNO complexes

The interaction of the NO molecule ($^2\Pi$) with the atomic ground state of coinage metal 2S will produce four different molecular states; $^1A'$, $^3A'$, $^1A''$, $^3A''$. Because there is no open shell singlet Hartree Fock implementation, the CCSD(T) method could not calculate the 2D-PES of $^1A''$ state. Hence, I have calculated three 2D-PESs for $^1A'$, $^3A'$, $^3A''$ states for each MNO complex:



The 2D-PES of AuNO states, $^1A'$, $^3A'$, $^3A''$, are shown in Figs. 5.1.1, 5.1.2, 5.1.3, respectively. About the AuNO($^1A'$) state, the PES has three separate attractive regions; the largest attractive region is in nitrogen region, it starts and ends smoothly at the minimum, $\alpha = 40^\circ$ and $d = 2.4 \text{ \AA}$ with binding energy -800 meV, this means that the gold atom binds with NO from nitrogen side and form a bent shape. The other attractive regions are small and have very sharp minima. I will pay attention only to the smooth minimum because the sharp minima could not be accurately described by CCSD(T) method and they need multi-configuration treatment.

The PES of AuNO($^3A'$) is almost repulsive and has shallow minimum when the gold atom perpendicular to the geometrical center of NO molecule at a distance 3.6 \AA . Due to the weak binding energy (-20 meV) and far distance, this minimum is called dispersive minimum. About $^3A''$ state, its PES is totally repulsive. Hence, the $^1A'$ and $^3A'$ are bound states and $^3A''$ is an unbound state.

The 2D-PESs that describe the binding of silver atom with the NO molecule are shown in Figs. 5.1.4, 5.1.5, 5.1.6. It is clear that the singlet state ($^1A'$) is bound state while the triplet states, $^3A'$, $^3A''$ are unbound states since their PESs are totally repulsive. It seems to me that the PES of $^1A'$ is a superposition of different configurations and CCSD(T) can not describe it well, hence, it needs a multi configuration treatment. I just concentrate on the minimum in the nitrogen region at $\alpha = 40^\circ$ and $d = 2.7 \text{ \AA}$ because I will compare it

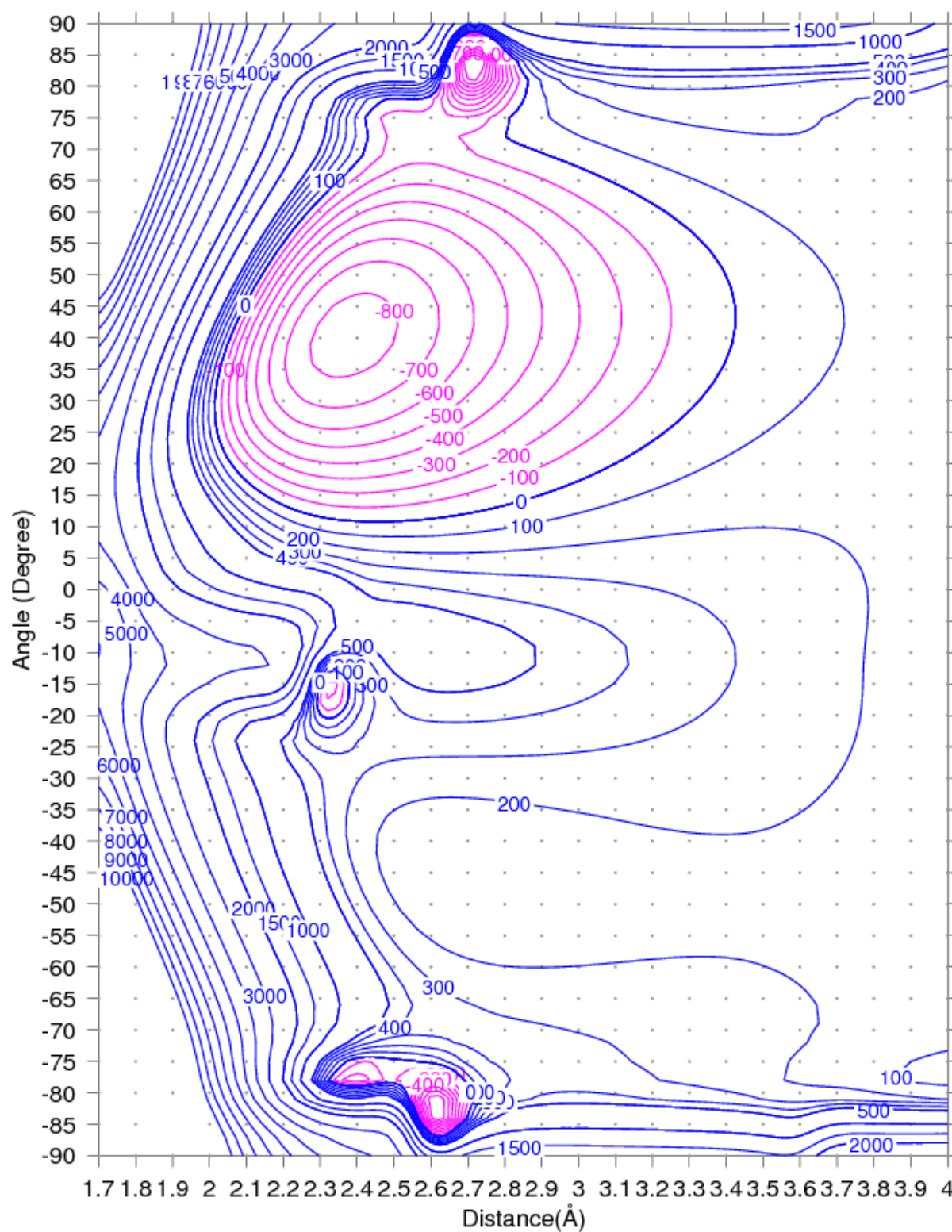


Figure 5.1.1: Counterpoise corrected binding energy surface of $\text{Au}(^2S) + \text{NO}(^2\Pi) \rightarrow \text{AuNO}(^1A')$ as a function of the angle and the distance between Au atom and NO center as described in Fig. 4.0.1 using UCCSD(T)/Au=ECP60MDF-AVTZ, N=AVTZ, O=AVTZ. The dots represent the binding energy calculated at different geometries.

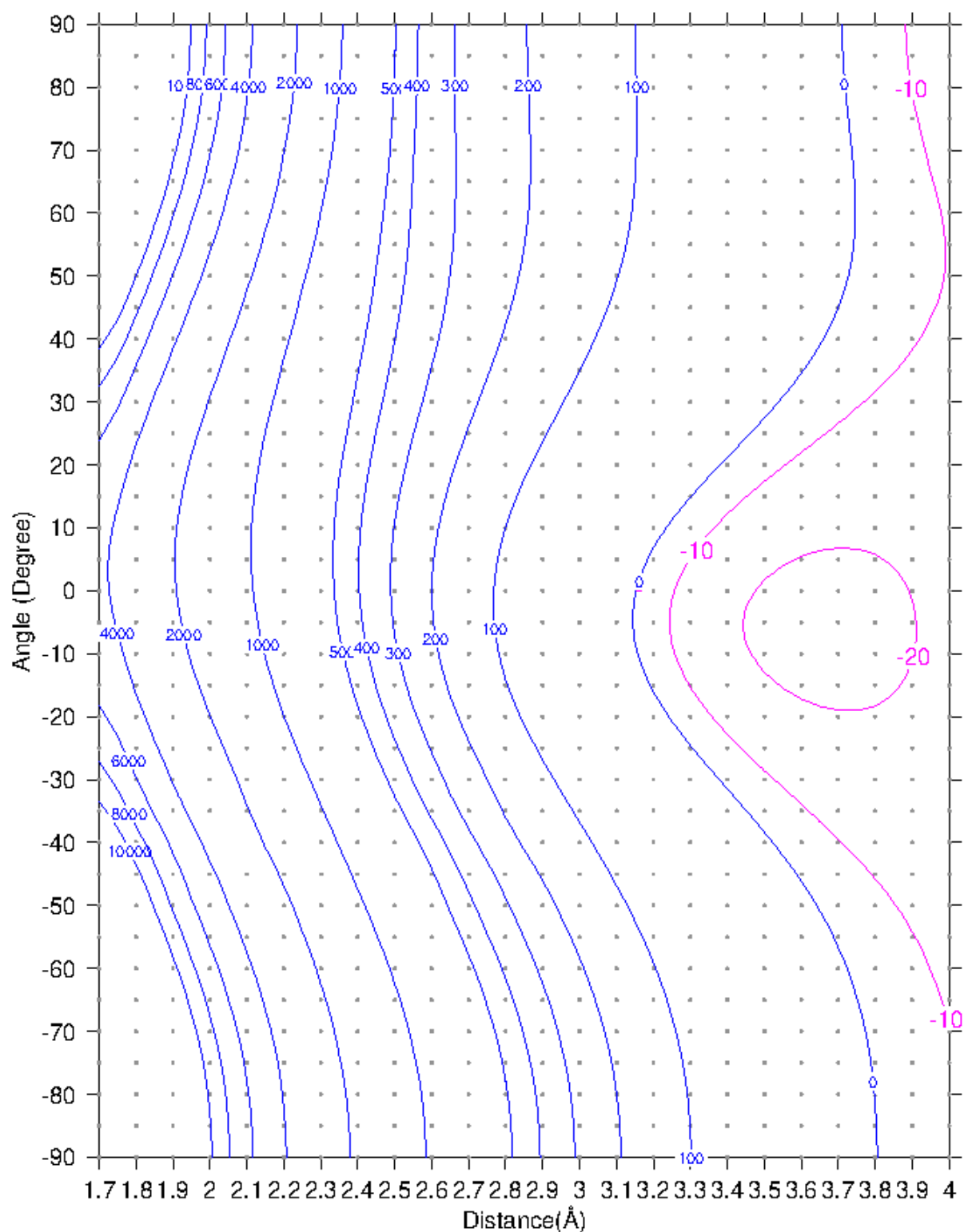


Figure 5.1.2: Counterpoise corrected binding energy surface of $\text{Au}(^2\text{S}) + \text{NO}(^2\Pi) \rightarrow \text{AuNO}(^3\text{A}')$ as a function of the angle and the distance between Au atom and NO center as described in Fig. 4.0.1 using UCCSD(T)/Au=ECP60MDF-AVTZ, N=AVTZ, O=AVTZ. The dots represent the binding energy calculated at different geometries.

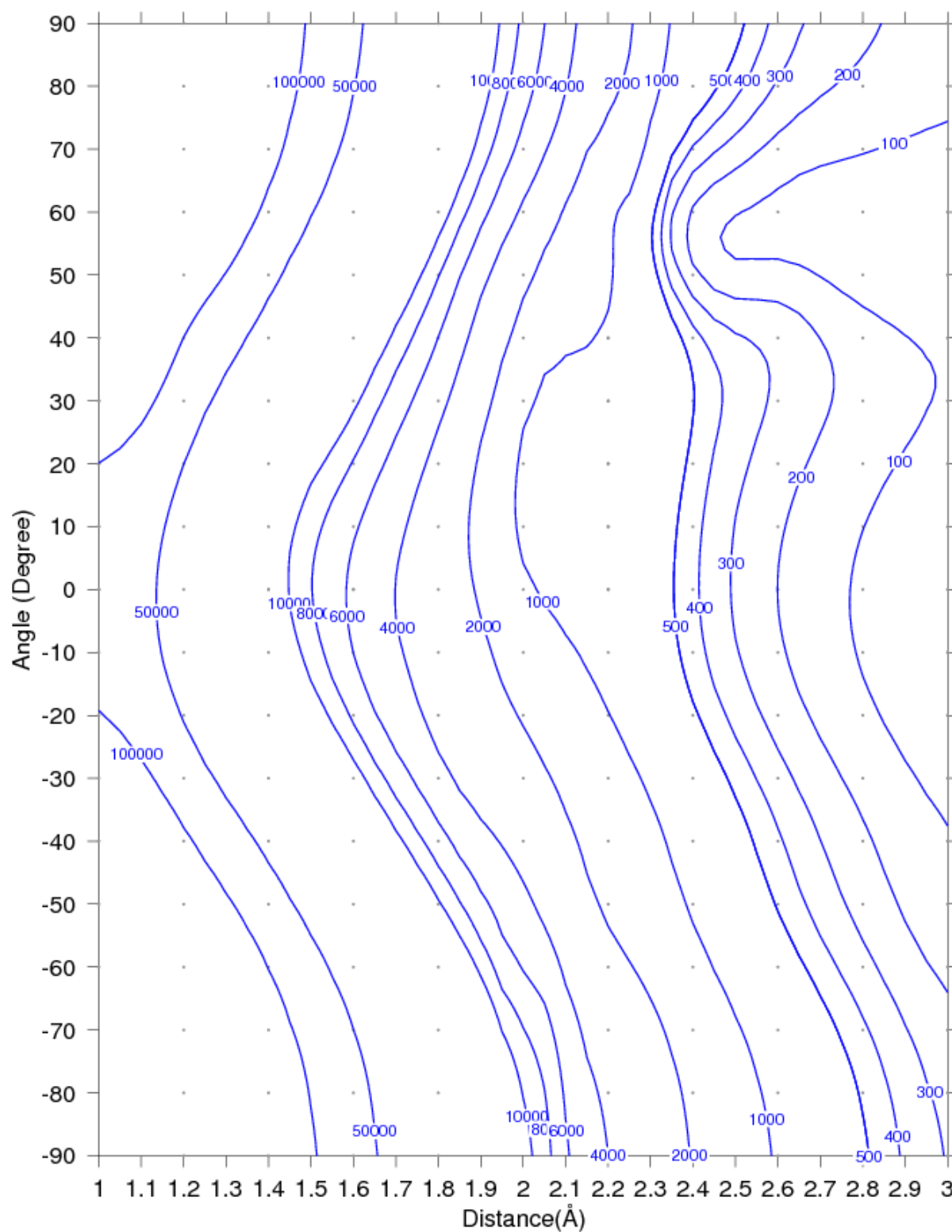


Figure 5.1.3: Counterpoise corrected binding energy surface of $\text{Au}(^2S) + \text{NO}(^2\Pi) \rightarrow \text{AuNO}(^3A'')$ as a function of the angle and the distance between Au atom and NO center as described in Fig. 4.0.1 using UCCSD(T)/Au=ECP60MDF-AVTZ, N=AVTZ, O=AVTZ. The dots represent the binding energy calculated at different geometries.

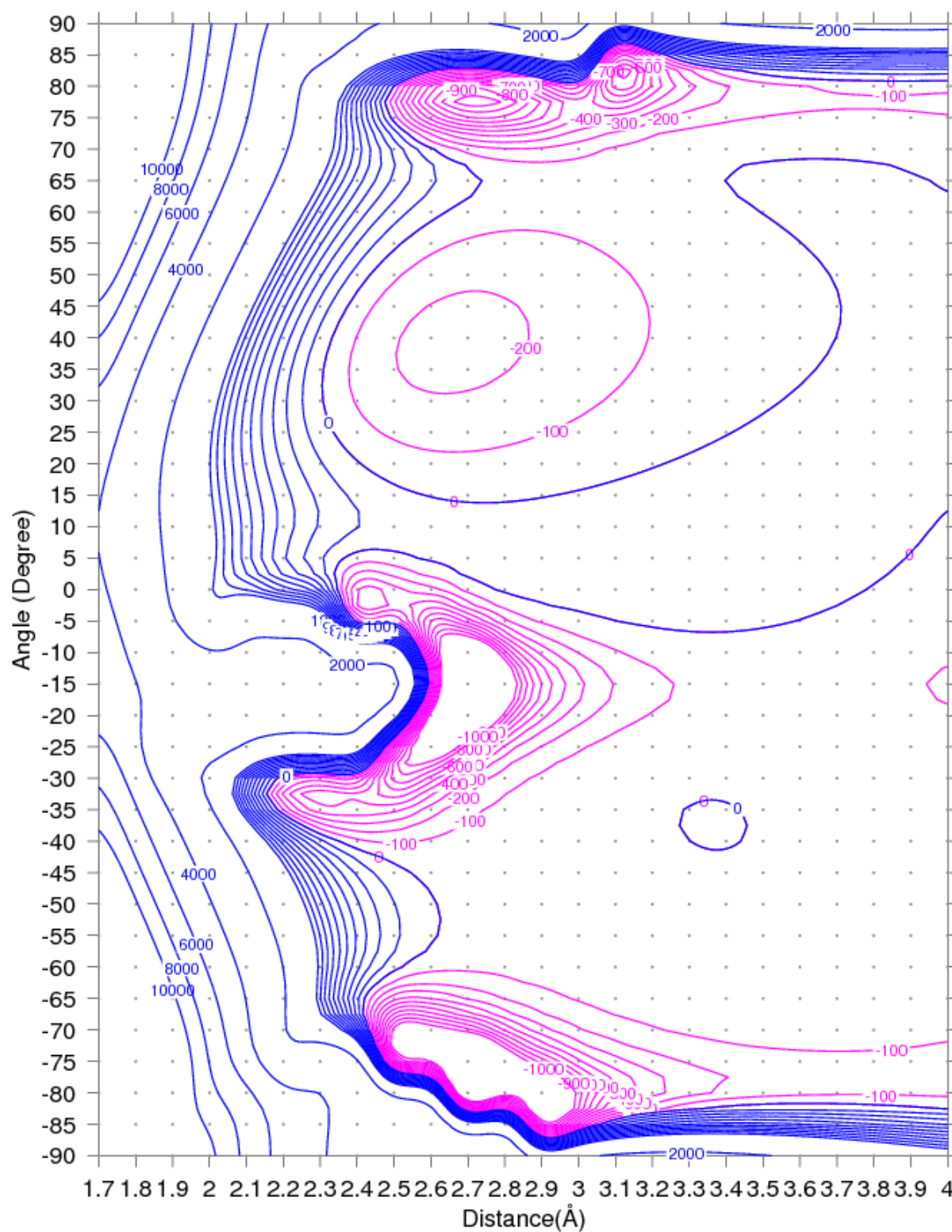


Figure 5.1.4: Counterpoise corrected binding energy surface of $\text{Ag}(^2S) + \text{NO}(^2\Pi) \rightarrow \text{AgNO}(^1A')$ as a function of the angle and the distance between Ag atom and NO center as described in Fig. 4.0.1 using UCCSD(T)/Ag=ECP28MDF-AVTZ, N=AVTZ, O=AVTZ. The dots represent the binding energy calculated at different geometries.

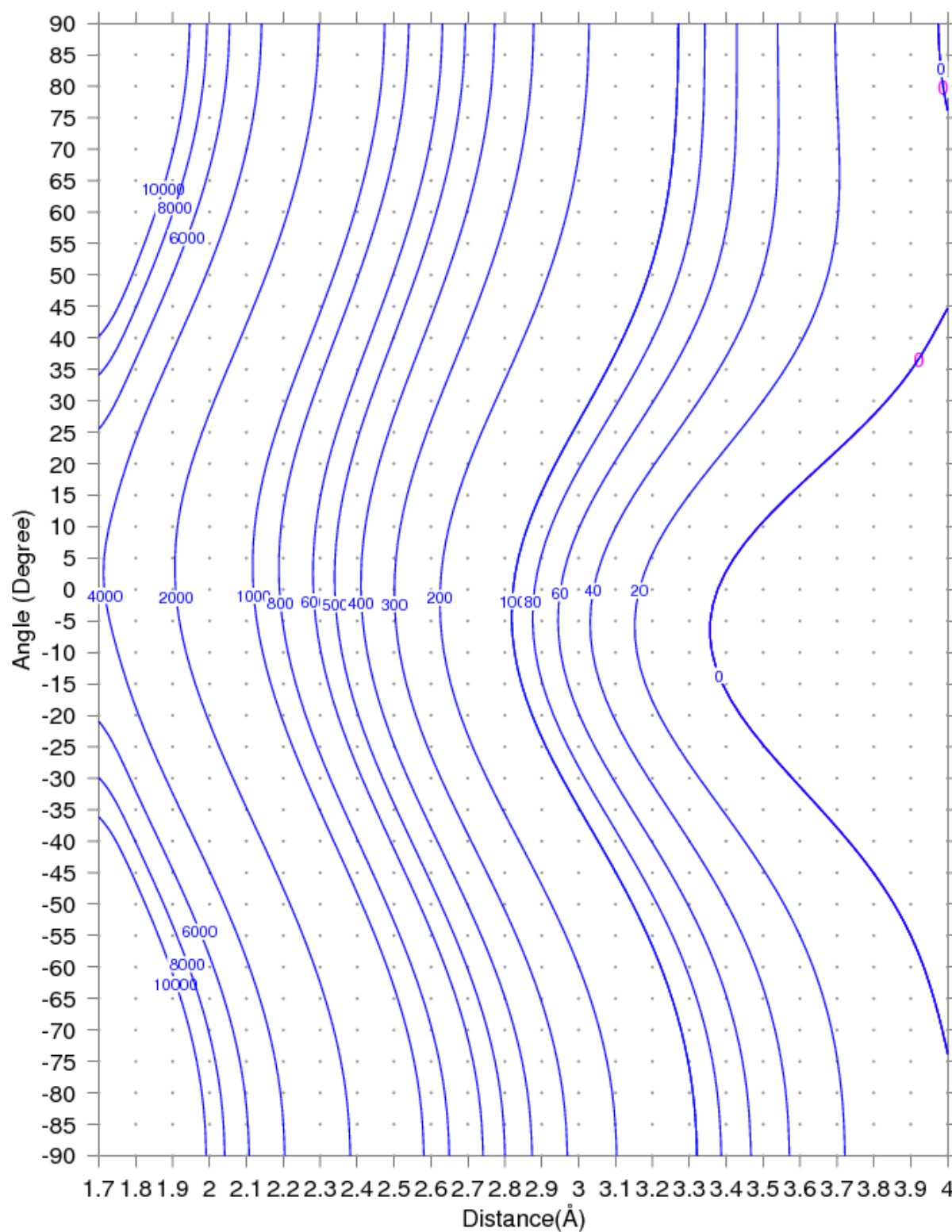


Figure 5.1.5: Counterpoise corrected binding energy surface of $\text{Ag}(^2\text{S}) + \text{NO}(^2\Pi) \rightarrow \text{AgNO}(^3\text{A}')$ as a function of the angle and the distance between Ag atom and NO center as described in Fig. 4.0.1 using UCCSD(T)/Ag=ECP28MDF-AVTZ, N=AVTZ, O=AVTZ. The dots represent the binding energy calculated at different geometries.

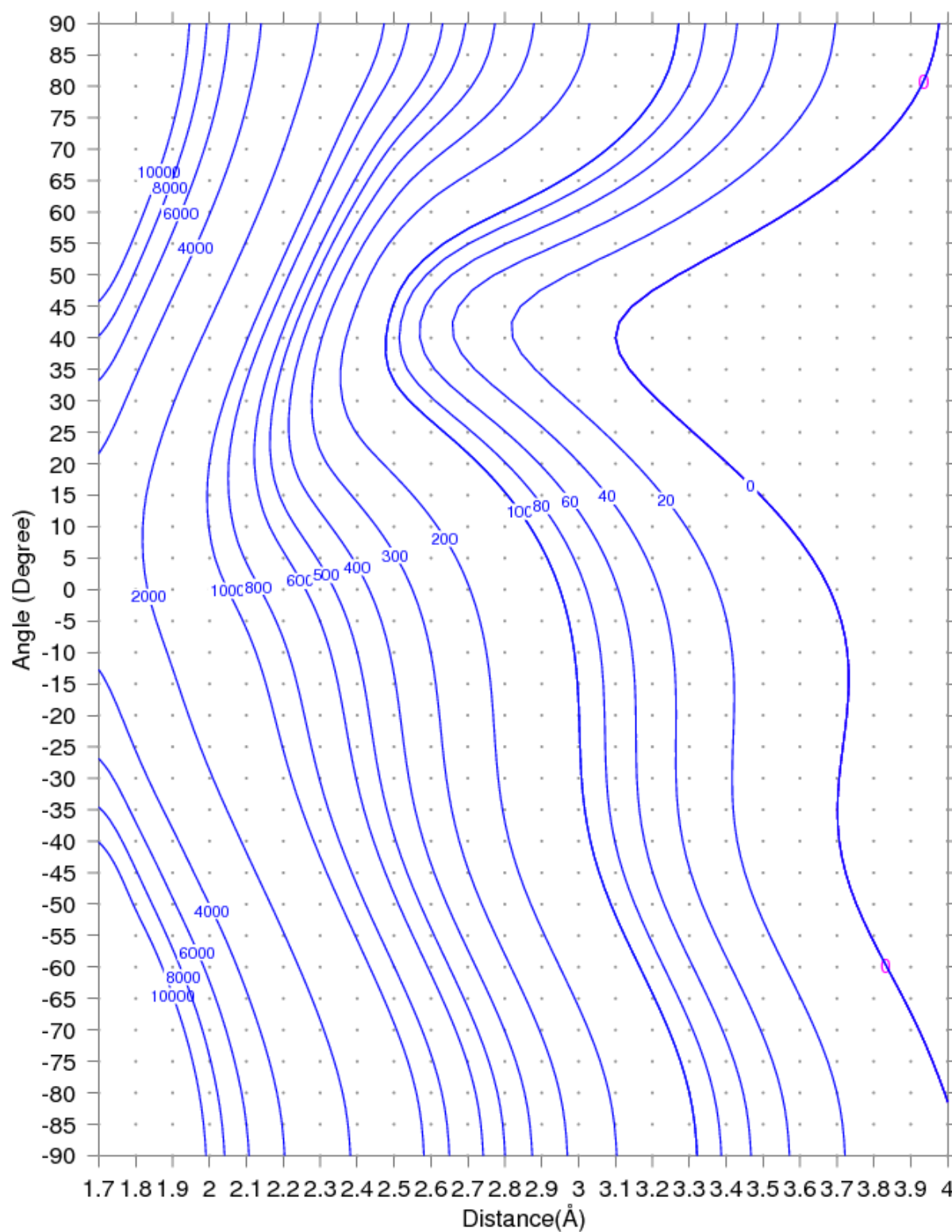


Figure 5.1.6: Counterpoise corrected binding energy surface of $\text{Ag}(^2S) + \text{NO}(^2\Pi) \rightarrow \text{AgNO}(^3A'')$ as a function of the angle and the distance between Ag atom and NO center as described in Fig. 4.0.1 using UCCSD(T)/Ag=ECP28MDF-AVTZ, N=AVTZ, O=AVTZ. The dots represent the binding energy calculated at different geometries.

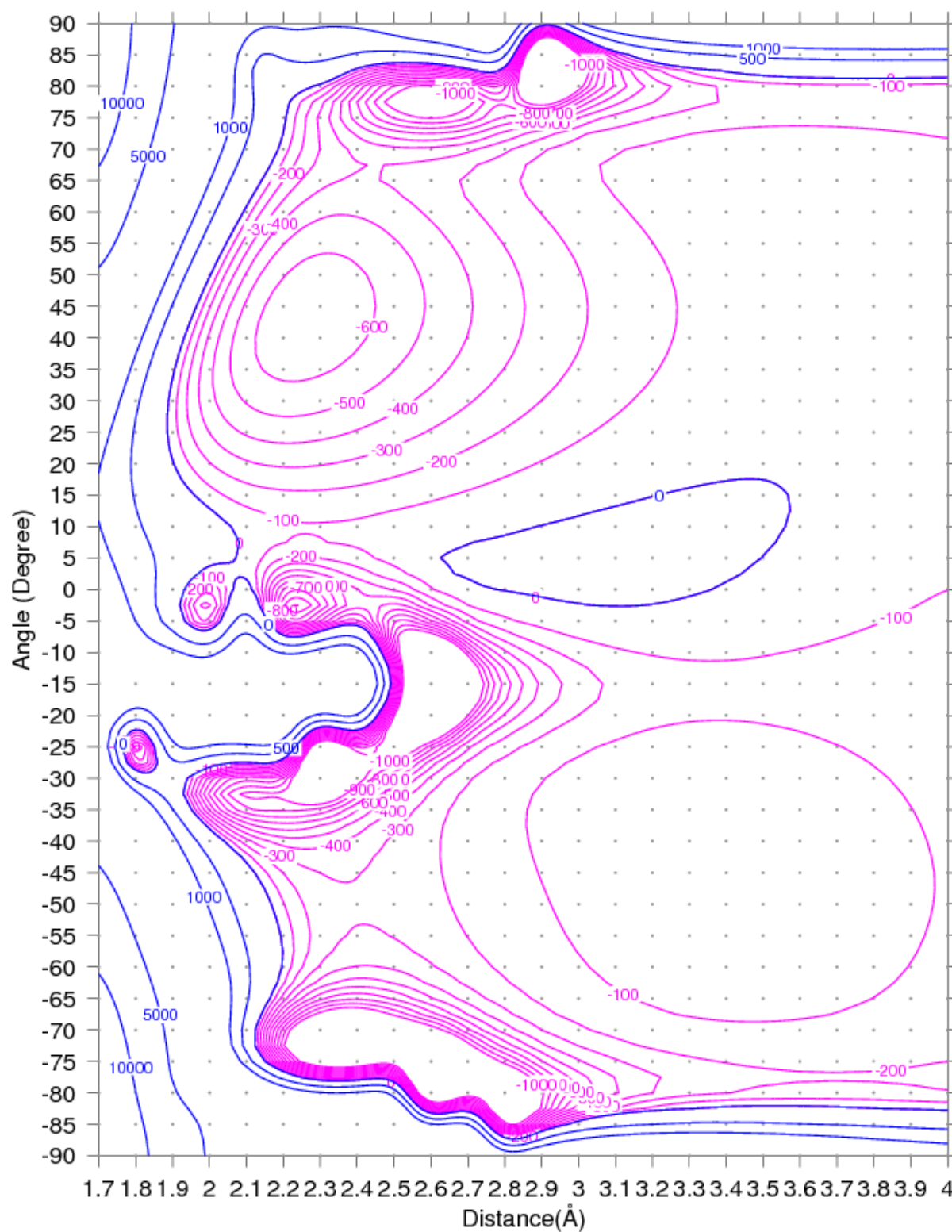


Figure 5.1.7: Counterpoise corrected binding energy surface of $\text{Cu}(^2S) + \text{NO}(^2\Pi) \rightarrow \text{CuNO}(^1A')$ as a function of the angle and the distance between Cu atom and NO center as described in Fig. 4.0.1 using UCCSD(T)/Cu=ECP10MDF-AVTZ, N=AVTZ, O=AVTZ. The dots represent the binding energy calculated at different geometries.

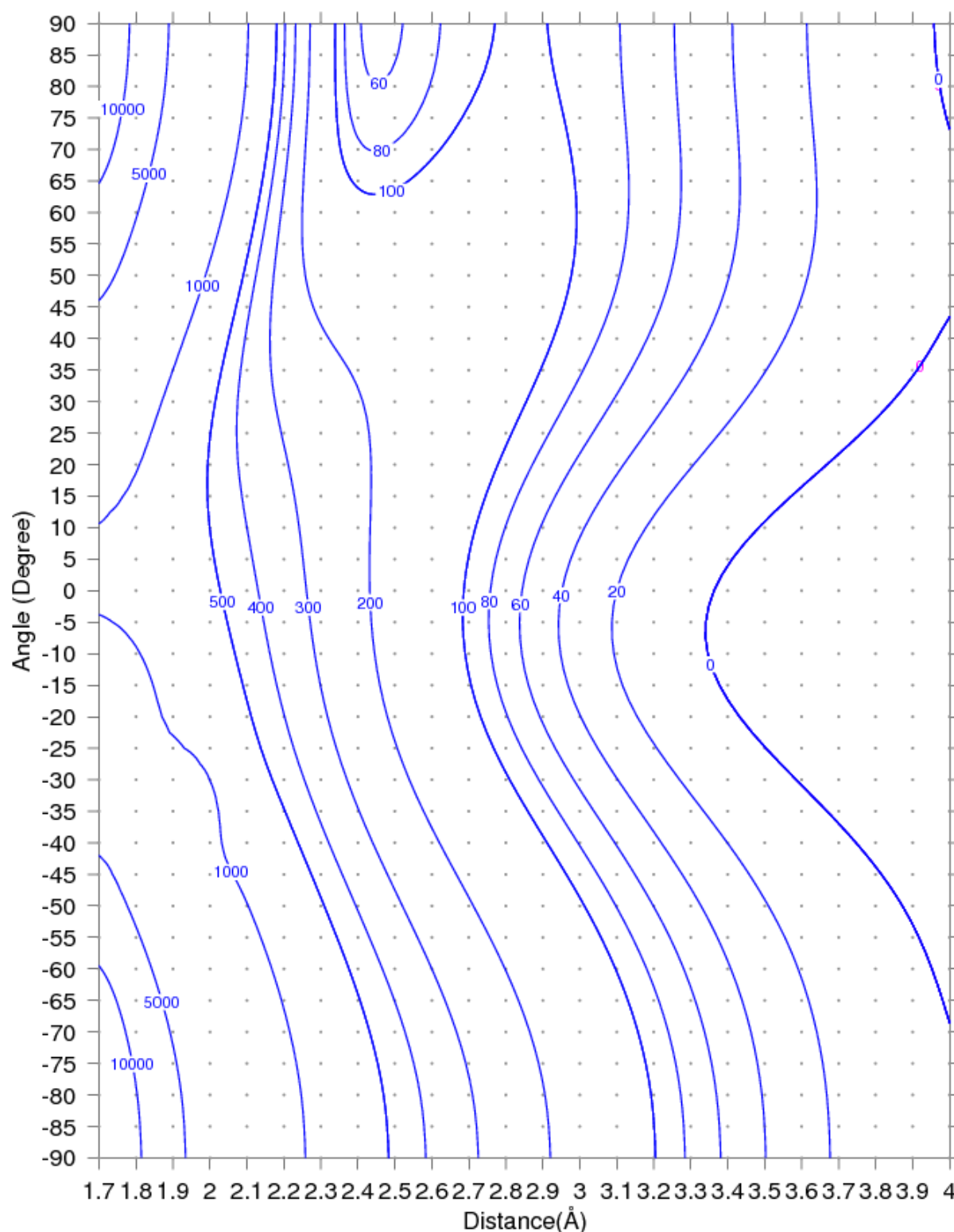


Figure 5.1.8: Counterpoise corrected dissociation energy surface of $\text{Cu}(^3\text{P}) + \text{NO}(^2\Pi) \rightarrow \text{CuNO}(^3\text{A}')$ as a function of the distance between Cu atom and NO center and the angle as described in Fig. 4.0.1 using UCCSD(T)/Cu=ECP10MDF-AVTZ,N=AVTZ,O=AVTZ. The dots represent the dissociation energy calculated at different geometries.

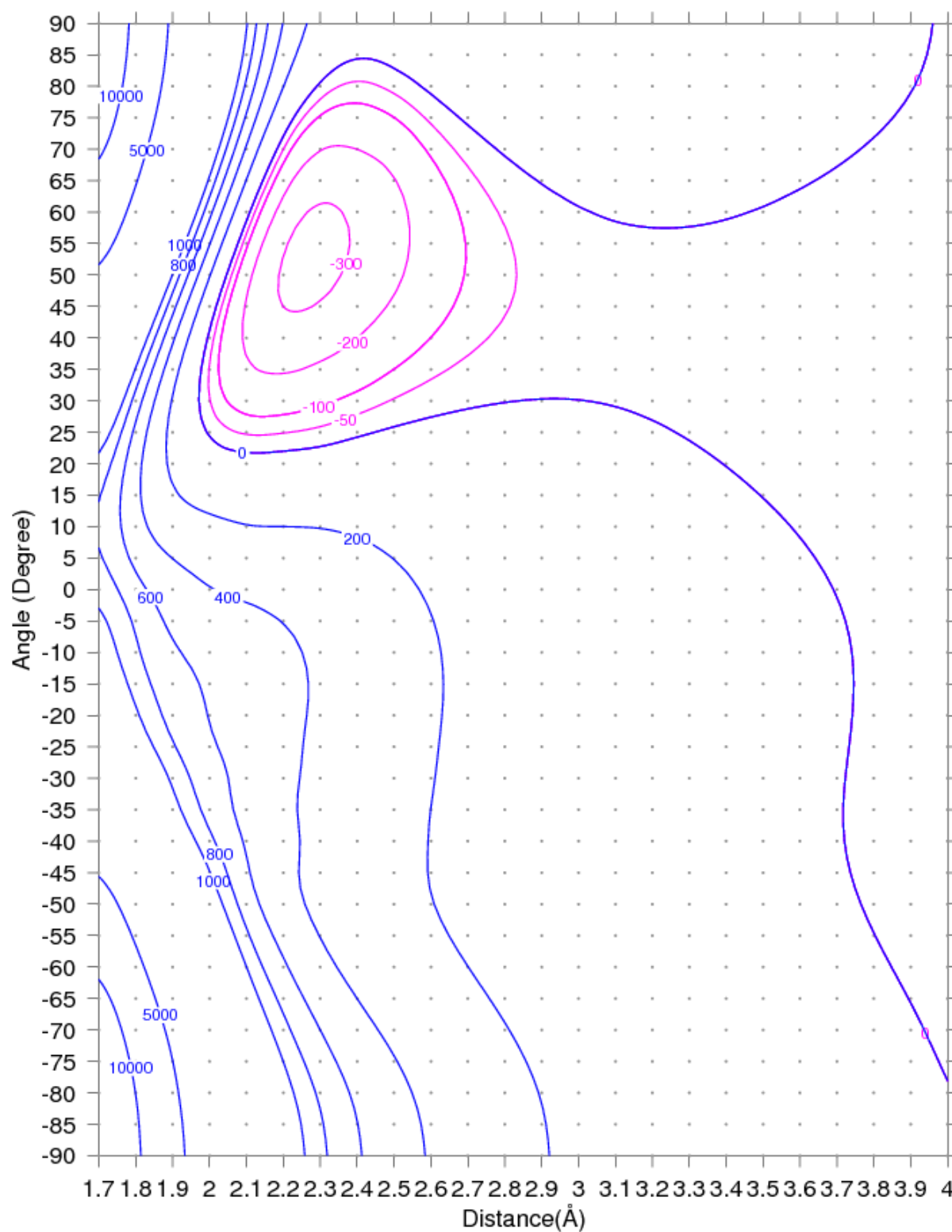


Figure 5.1.9: Counterpoise corrected binding energy surface of $\text{Cu}(^2S) + \text{NO}(^2\Pi) \rightarrow \text{CuNO}(^3A'')$ as a function of the angle and the distance between Cu atom and NO center as described in Fig. 4.0.1 using UCCSD(T)/Cu=ECP10MDF-AVTZ, N=AVTZ, O=AVTZ. The dots represent the binding energy calculated at different geometries.

with the similar minimum of AuNO ($^1A'$).

The 2D-PESs that describe the three states of copper mononitrosyl, $^1A'$, $^3A'$ and $^3A''$, are shown in Figs. 5.1.7, 5.1.8, 5.1.9, respectively. The PES of $^1A'$ state is similar to the PES of the $^1A'$ state of AuNO and AgNO, it have attraction and repulsive regions with many sharp minima. I only pay attention to the minimum in the nitrogen region at $\alpha = 45^\circ$ and $d = 2.2 \text{ \AA}$ with binding energy -600 meV because it starts and finish smoothly. This minimum is an evidence that the copper binds with NO molecule from nitrogen side and form a bent complex. About the triplet spin states, the PES of $^3A'$ is totally repulsive, and the PES of $^3A''$ state has a minimum in nitrogen region, hence a bent complex is formed. Thus, the CuNO complex has two bound states $^1A'$ and $^3A''$.

In order to know how much the NO bond length is changed and what are the optimized parameters for each bound state, a full optimization calculation were done with considering the geometry at the minimum as an initial guess. The optimized bond parameters and the counterpoise ZEP corrected binding energy are summarized in Tab. 5.1.1, and the calculated vibrational frequencies are in Tab. 5.1.2.

Complex	Molecular state	r_{M-N} Å	r_{N-O} Å	$\angle MNO$ Degree	ΔE meV	BSSE meV	ΔZPE meV	$E_{CP+\Delta ZPE}$ meV
AuNO	$^1A'$	2.043	1.163	118.0	0	-48.0	39.2	-813.8
	$^3A'$	3.535	1.157	179.0	+875.8	-9.6	-0.08	-15.5
AgNO	$^1A'$	2.317	1.1713	118.1	0	-20.9	20.1	-230.9
CuNO	$^1A'$	1.903	1.1756	120.0	0	-36.9	30.7	-670.8
	$^3A''$	1.823	1.2084	129.5	+262.7	+56.5	17.4	-515.0

Table 5.1.1: The optimized bond parameters of MNO with M: Au, Ag, Cu. The r_{M-N} and $\angle MNO$ are different than the angle (α) and the distance (d) in Fig. 4.0.1. The basis set superposition error(BSSE), zero point energy (ZPE) and the counterpoise ZPE corrected binding energy using UCCSD(T)/ECP(60,28,10)MDF-AVTZ.

The ground state of the AuNO complexes is $^1A'$, it has a bent shape as predicted from the 2D-PES, the bond length between the oxygen and nitrogen is longer than the free NO bond length that makes the N-O stretching frequency less than the frequency of the free NO molecule and hence a red shift in N-O stretching frequency is calculated. To know the reason why AuNO($^1A'$) is bonding and AuNO($^3A''$) unbonding state, the canonical

Complex	Molecular state	N-O stretching cm ⁻¹	M-N stretching cm ⁻¹	M-N-O bending cm ⁻¹	NO shift cm ⁻¹
AuNO	¹ A'	1732.4	515.7	273.1	-156.7
	³ A'	1887.8	-	-	-1.3
AgNO	¹ A'	1744.4	318.1	151.4	-144.7
CuNO	¹ A'	1683.3	434.8	265.5	-205.8
	³ A''	1488.3	460.0	220.9	-400.8

Table 5.1.2: The vibrational frequencies of MNO with M: Au, Ag, Cu. The NO shift is calculated as a difference of N-O stretching frequency and the free NO frequency (1889.1 cm⁻¹) using UCCSD(T)/ECP(60,28,10)MDF-AVTZ.

molecular orbitals diagram of both states were studied, see Fig. 5.1.10.

The canonical orbitals of AuNO(¹A') show that this complex is a diamagnetic one since all the orbitals are doubly occupied and it has one bond since the number of electrons in bonding orbitals is more than in the antibonding orbitals by two electrons. However, the Mulliken population analysis from the canonical orbitals, see Tab. 6.0.2, shows that there is a little charge transfer, 0.08 electrons, from NO to the Au, this means that the binding is done through a covalent bond. In addition, the HOMO is a bonding orbital between gold and nitrogen and antibonding between nitrogen and oxygen, it is formed from the constructive overlap between (6s) orbital of gold and (3π*) of NO which leads to bending geometry with ∠AuNO = 118.0°.

About the AuNO(³A'') state, there is a difference between the molecular orbitals diagram of the AuNO(³A'') and AuNO(¹A') states; the HOMO of AuNO(³A'') state is singly occupied and there is another singly occupied orbital called HOMO-1 which is an antibonding orbital formed by combination of d_{xy} gold atomic orbital and 2π_x* NO molecular orbital, see the orbitals in Fig. 5.1.10. This makes the bond order zero and so no bond is formed.

The third state of gold-mononitrosyl (³A'), it is very weakly bond since its binding energy is -15.5 meV and the canonical orbitals shows that there is no overlap between the atomic orbitals of the gold atom and the NO molecular orbitals. Moreover, the r_{M-N} is longer than the ground state (¹A') by 1.492 Å and the NO bond length and its frequency are nearly same as the free NO. This means that the (³A') state is formed because of van der Waals dispersion interaction.

Regarding the silver nitrosyl, the molecular ground state is $^1A'$, where the silver atom can capture spontaneously the NO molecule at distance 2.317 Å. Its canonical molecular orbitals diagram is similar to the molecular orbital diagram of AuNO in Fig. 5.1.10, and the Mulliken charge analysis in Tab. 6.0.2 shows that there is a significant charge transfer, 0.3 electrons, from silver atom to NO molecule. Therefore, the N-O bond length increases and the N-O stretching frequency decreases, and hence a red shift in the NO vibrational frequency is calculated. Due to the charge transfer and the shape of the HOMO, the silver atom binds with NO molecule through a dative covalent bond and form a bent shape with 118° .

Concerning the copper nitrosyl, it has two bound states, $^1A'$ and $^3A''$. The ground state is $^1A'$ where the copper atom binds with NO molecule through a dative covalent bond because there is significant charge transfer from copper atom to the NO molecule, 0.28 electrons, see Tab. 6.0.2. The HOMO consists from the constructive overlap between the 4s copper atomic orbital and the $2\pi^*$ NO molecular orbital, thus, the geometry of the CuNO $^1A'$ complex is bent shape with $\angle \text{CuNO} = 120^\circ$.

Furthermore, the canonical molecular orbitals of the excited states of copper nitrosyl ($^3A''$) shows that the HOMO and HOMO-1 are singly occupied, $2\pi_x^*$ and $2\pi_y^*$, which mean that the NO molecule captures the valence electron of copper. This explain the increasing of the NO bond length and the decreasing of NO frequency and the short bond length between copper and nitrogen.

In conclusion, the ground state of MNO complexes is $^1A'$, the NO molecule binds with gold through covalent bond while it binds with silver and copper through a dative covalent bond. The $^1A'$ state has multi-references character. Therefore, the CCSD(T) could not produce smooth PES.

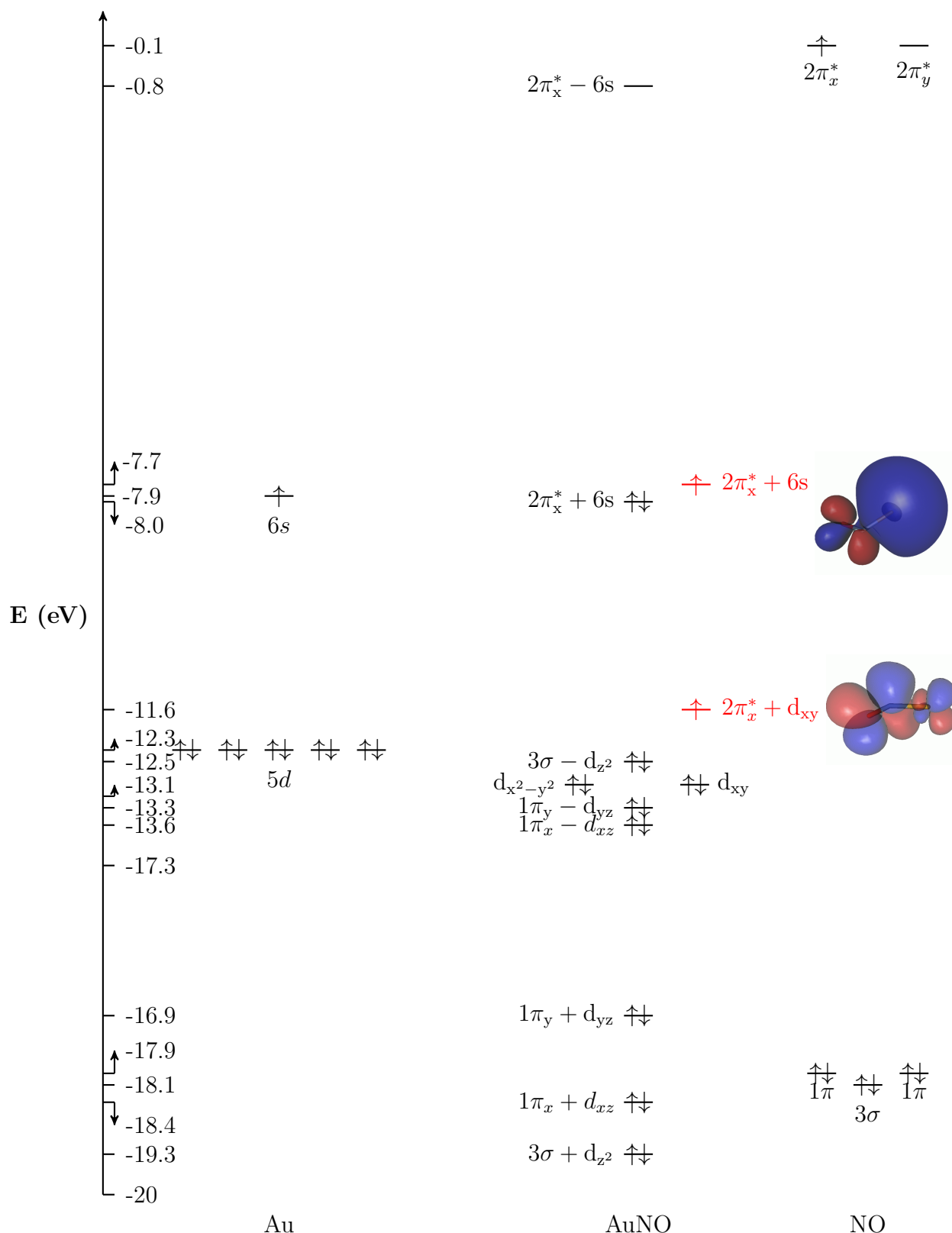
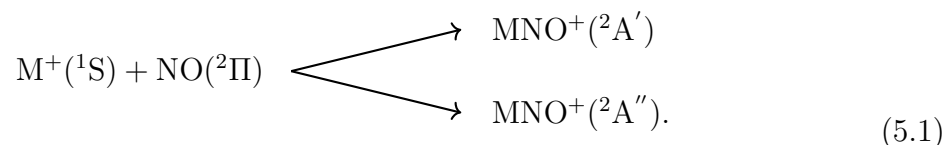


Figure 5.1.10: Energy level diagram for canonical molecular orbitals of AuNO complex ($^1A'$) using RHF/AVTZ. The NO molecular orbitals have the same labels as in Fig. 3.2.1. The molecular orbital occupation depending on C_s point group is: $(1a')^2(1a'')^2(2a')^2(2a'')^2(3a')^2(3a'')^2(4a')^2(5a')^2(6a')^2$. The molecular orbital diagram of $^3A''$ state has two unpaired electrons instead of two electrons in $2\pi_x^* + 6s$ orbital, see the red colored orbitals and the pictures, they are the HOMO and HOMO-1 of $^3A''$. Hence, the molecular orbitals occupation of $^3A''$: $(1a')^2(1a'')^2(2a')^2(2a'')^2(3a')^2(3a'')^2(4a')^2(5a')^2(6a'')^1(6a')^1$. (the gold atom on the right and the NO molecule on the left, the isocontour is 0.025.)

5.2 2D-PESs of MNO^+ complexes

The interaction of the ground state of the coinage metal cation (^1S) with the NO molecule ($^2\Pi$) produces two different states of the coinage mononitrosyl cation MNO^+ , $^2\text{A}'$, $^2\text{A}''$, depending on C_s point group:



Based on Eq. 5.1, I have calculated two PESs for each MNO^+ , see Figs. 5.2.1, 5.2.6. The PESs of AuNO^+ show that the interaction between the gold cation and the NO molecule is attractive interaction over the entire parameters space and they have two minima, (m_1, m_2) , the first minimum is in the nitrogen region and the second minimum is in the oxygen region with weaker binding energy. In details, the first minimum of the $^2\text{A}'$ state is at $\alpha = 45^\circ$ and $d = 2.4 \text{ \AA}$ with binding -1250 meV , the second minimum is at $\alpha = -45^\circ$ and $d = 2.6 \text{ \AA}$ with binding energy -650 meV . This means that the gold cation binds with NO molecule either from nitrogen side or from oxygen side and forms bent AuNO^+ or AuON^+ structure. Furthermore, the AuON^+ should overcome an energy barrier of 300 meV to transform into AuNO^+ by rotating the gold cation from $\alpha = -45^\circ$ to $\alpha = 45^\circ$.

The PES of the $^2\text{A}''$ state have two minima at $\alpha = \pm 90$ and distances 2.7 \AA , 2.9 \AA , respectively. This mean that $^2\text{A}''$ state have two linear structures AuNO^+ and AuON^+ . The AuNO^+ structure of both states, $^2\text{A}'$, $^2\text{A}''$ are more stable than AuON^+ structures because they have stronger binding energies. The energy needed to transform the AuON^+ structure into the stable structure is about 200 meV . Both states dissociate into gold cation and NO molecule if the gold cation rotates to be perpendicular to the NO molecule and then move a way.

About the AgNO^+ complex, the PESs are shown in Figs. 5.2.3, 5.2.4. They are almost attractive and have two minima, the deep minimum is in the nitrogen region and the shallow minimum is in the oxygen region as the AuNO^+ complex. Regarding the $^2\text{A}'$ state, it has bent stable structure AgNO^+ at $\alpha = 50^\circ$ and $d = 2.7 \text{ \AA}$, with binding energy -650 meV and a bent metastable structure AgON^+ at $\alpha = -50^\circ$ and $d = 2.8 \text{ \AA}$ with

binding -350 meV. In addition, the energy barrier that the metastable structure should overcome to transform into the stable structure around 50 meV.

Concerning the ${}^2A''$ state, it has linear stable structure $AgNO^+$ at $d = 2.9 \text{ \AA}$ with binding energy -500 meV, and linear metastable structure $AgON^+$ at $d = 3 \text{ \AA}$ with binding energy -250 meV. The energy required to transform from the metastable structure to the stable structure is 150 meV. Both states of $AgNO^+$ dissociate by rotating the silver cation to be perpendicular to the NO molecule and then move away as $AuNO^+$.

The PESs that describe the interaction of copper cation with the NO molecule are shown in Figs. 5.2.5, 5.2.6, they are similar to the corresponding states of $AuNO^+$ and $AgNO^+$ since they are almost attractive with two minima, a minimum with strong binding energy in the nitrogen region and the other with weaker binding energy in the oxygen region. Regarding the ${}^2A'$ state, it has bent stable structure $CuNO^+$ at $\alpha = 55^\circ$ and $d = 2.3 \text{ \AA}$ with binding energy -1000 meV, and a bent metastable structure $CuON^+$ at $\alpha = -50^\circ$ and $d = 2.4 \text{ \AA}$ with binding energy -600 meV. The energy barrier that the metastable structure should overcome to transform into the stable structure around 200 meV.

Concerning the ${}^2A''$ state, it has linear stable structure $CuNO^+$ at $d = 2.5 \text{ \AA}$, and linear metastable structure $CuON^+$ at $d = 2.6 \text{ \AA}$. The energy required to transform the metastable structure into the stable structure is 200 meV.

In conclusion, the behavior of the gold, silver and copper cations towards the NO molecule are similar; the PESs are attractive over the entire parameters space and each PES has two minima, the minimum in nitrogen region has stronger binding energy than the minimum in oxygen region. The ${}^2A'$ states have bent structure while the ${}^2A''$ states have linear structure. The $AuNO^+$ complex have the strongest binding energy, then the $CuNO^+$ complex, and the $AgNO^+$ is the weakest.

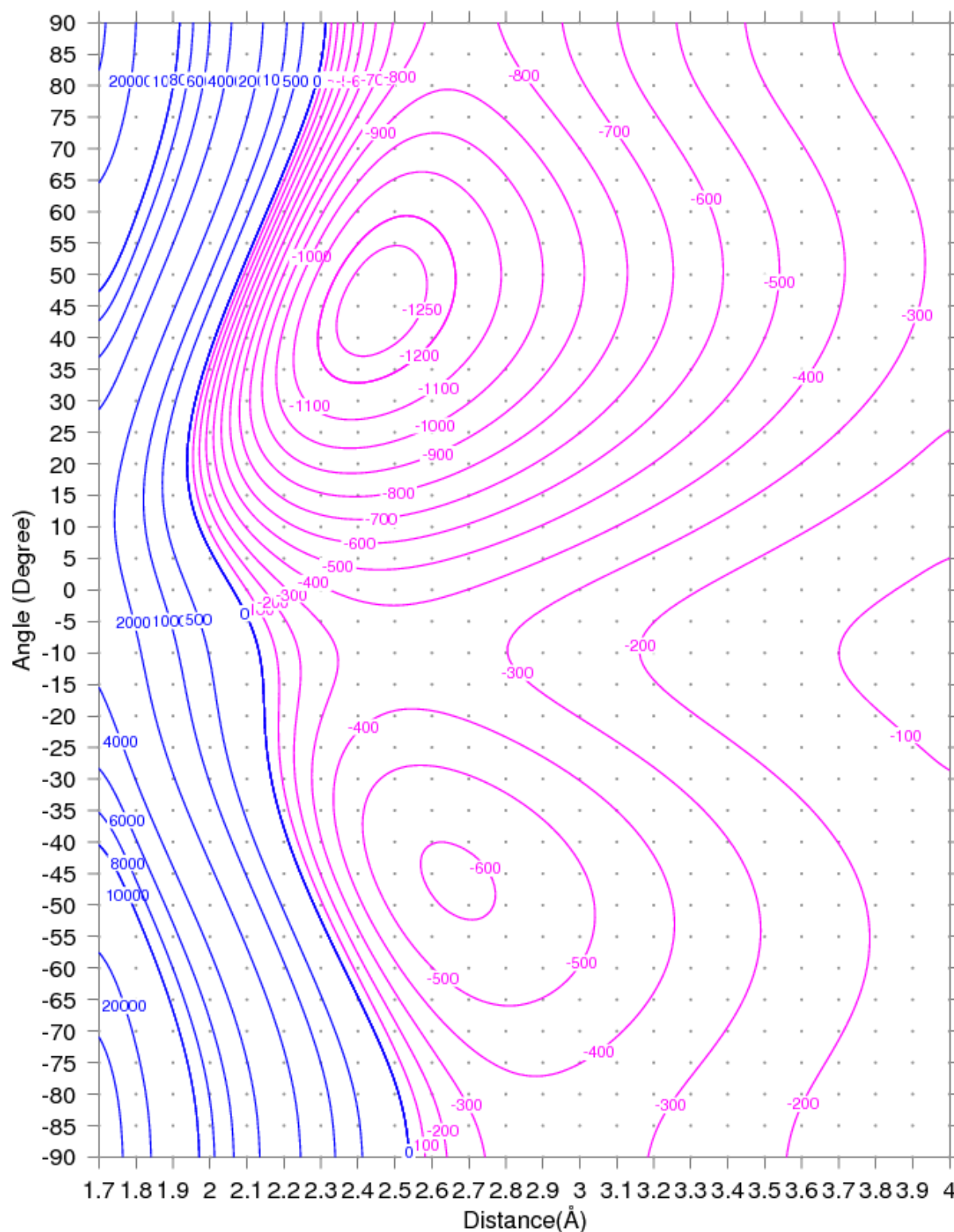


Figure 5.2.1: Counterpoise corrected binding energy surface of $\text{Au}^+(^1\text{S}) + \text{NO}(^2\Pi) \rightarrow \text{AuNO}^+(^2\text{A}')$ as a function of the angle and the distance between Au atom and NO center as described Fig. 4.0.1 using UCCSD(T)/Au=ECP60DF-AVTZ, N=AVTZ, O=AVTZ. The dots represent the binding energy calculated at different geometries.

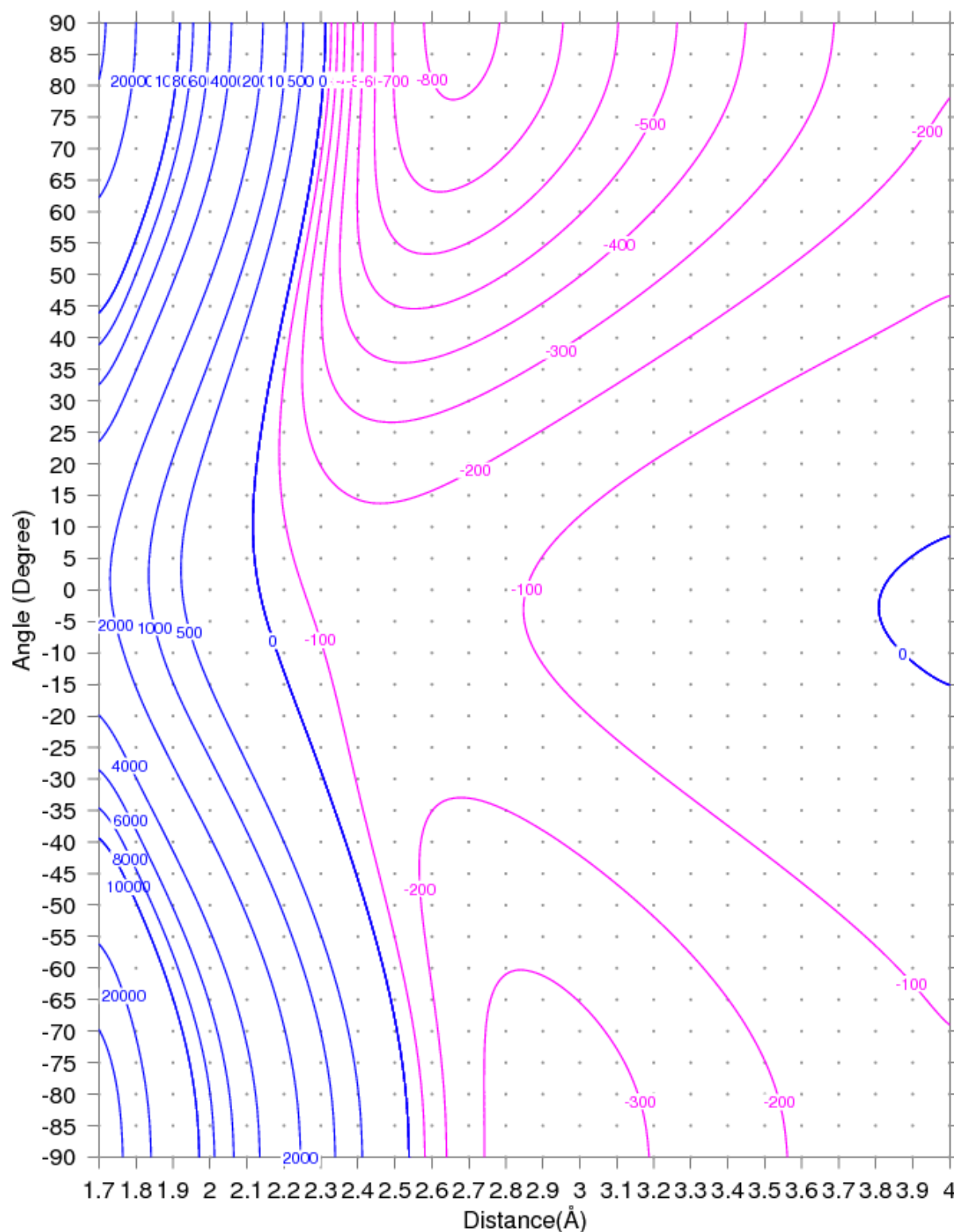


Figure 5.2.2: Counterpoise corrected binding energy surface of $\text{Au}^+(^1\text{S}) + \text{NO}(^2\Pi) \rightarrow \text{AuNO}^+(^2\text{A}'')$ as a function of the angle and the distance between Au atom and NO center as described in Fig. 4.0.1 using UCCSD(T)/Au=ECP60DF-AVTZ, N=AVTZ, O=AVTZ. The dots represent the binding energy calculated at different geometries.

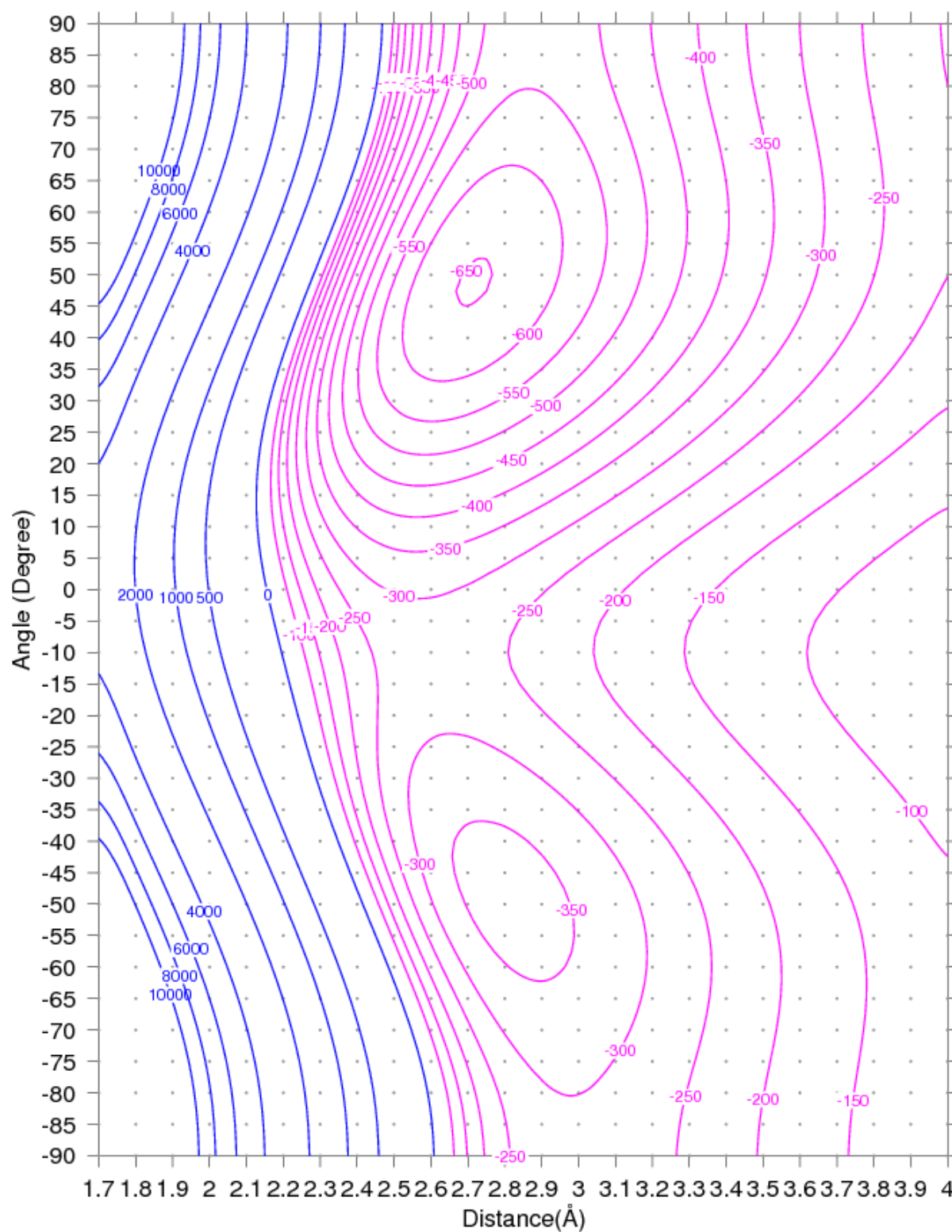


Figure 5.2.3: Counterpoise corrected binding energy surface of $\text{Ag}^+(^1\text{S}) + \text{NO}(^2\Pi) \rightarrow \text{AgNO}^+(^2\text{A}')$ as a function of the angle and the distance between Ag atom and NO center as described in Fig. 4.0.1 using UCCSD(T)/Ag=ECP28MDF-AVTZ, N=AVTZ, O=AVTZ. The dots represent the binding energy calculated at different geometries.

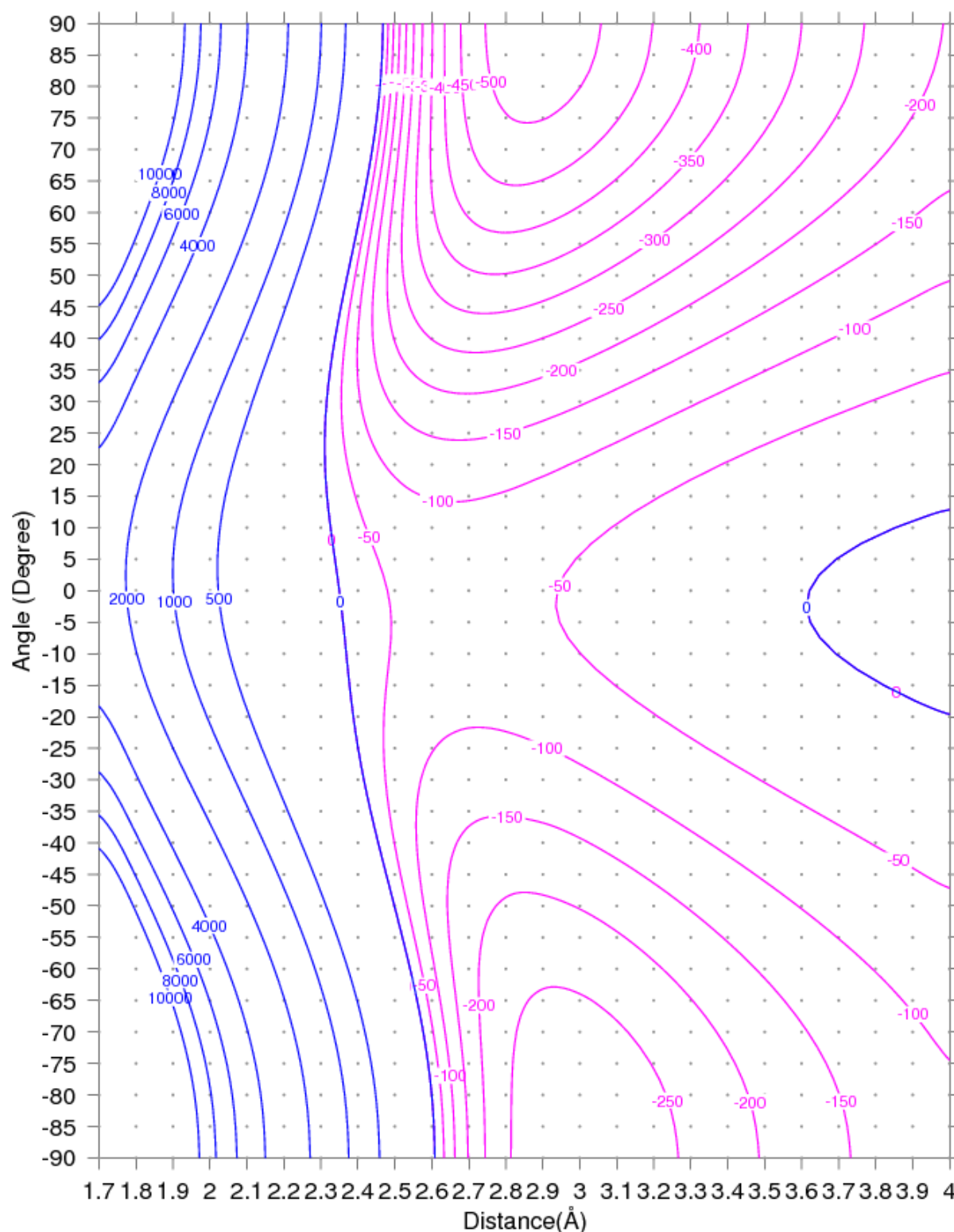


Figure 5.2.4: Counterpoise corrected binding energy surface of $\text{Ag}^+(^1\text{S}) + \text{NO}(^2\Pi) \rightarrow \text{AgNO}^+(^2\text{A}'')$ as a function of the angle and the distance between Ag atom and NO center as described in Fig. 4.0.1 using UCCSD(T)/Ag=ECP28MDF-AVTZ, N=AVTZ, O=AVTZ. The dots represent the binding energy calculated at different geometries.

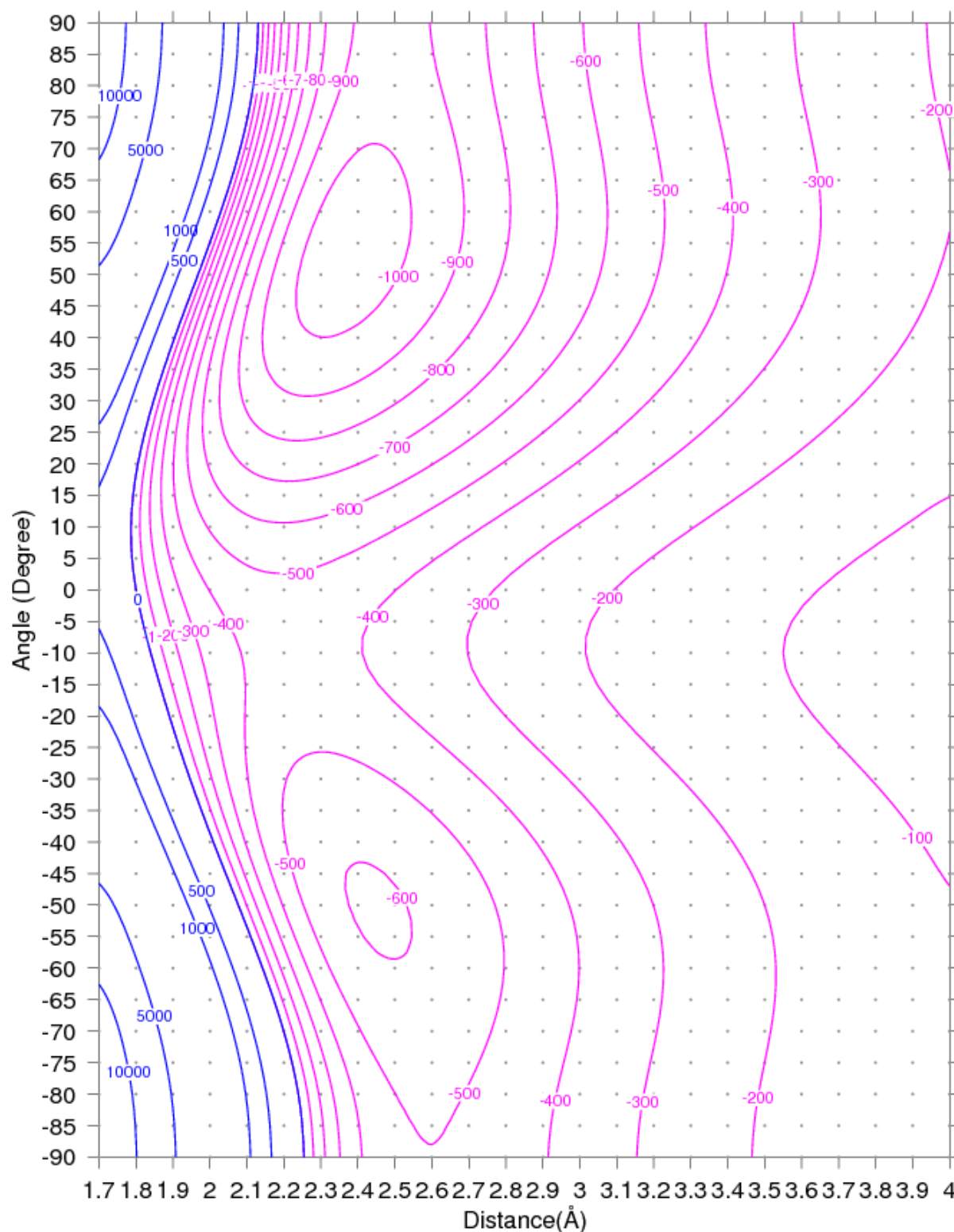


Figure 5.2.5: Counterpoise corrected binding energy surface of $\text{Cu}^+(^1\text{S}) + \text{NO}(^2\Pi) \rightarrow \text{CuNO}^+(^2\text{A}')$ as a function of the distance between Cu atom and NO center and angle as described in Fig. 4.0.1 using UCCSD(T)/Cu=ECP10MDF-AVTZ, N=AVTZ, O=AVTZ. The dots represent the binding energy calculated at different geometries.

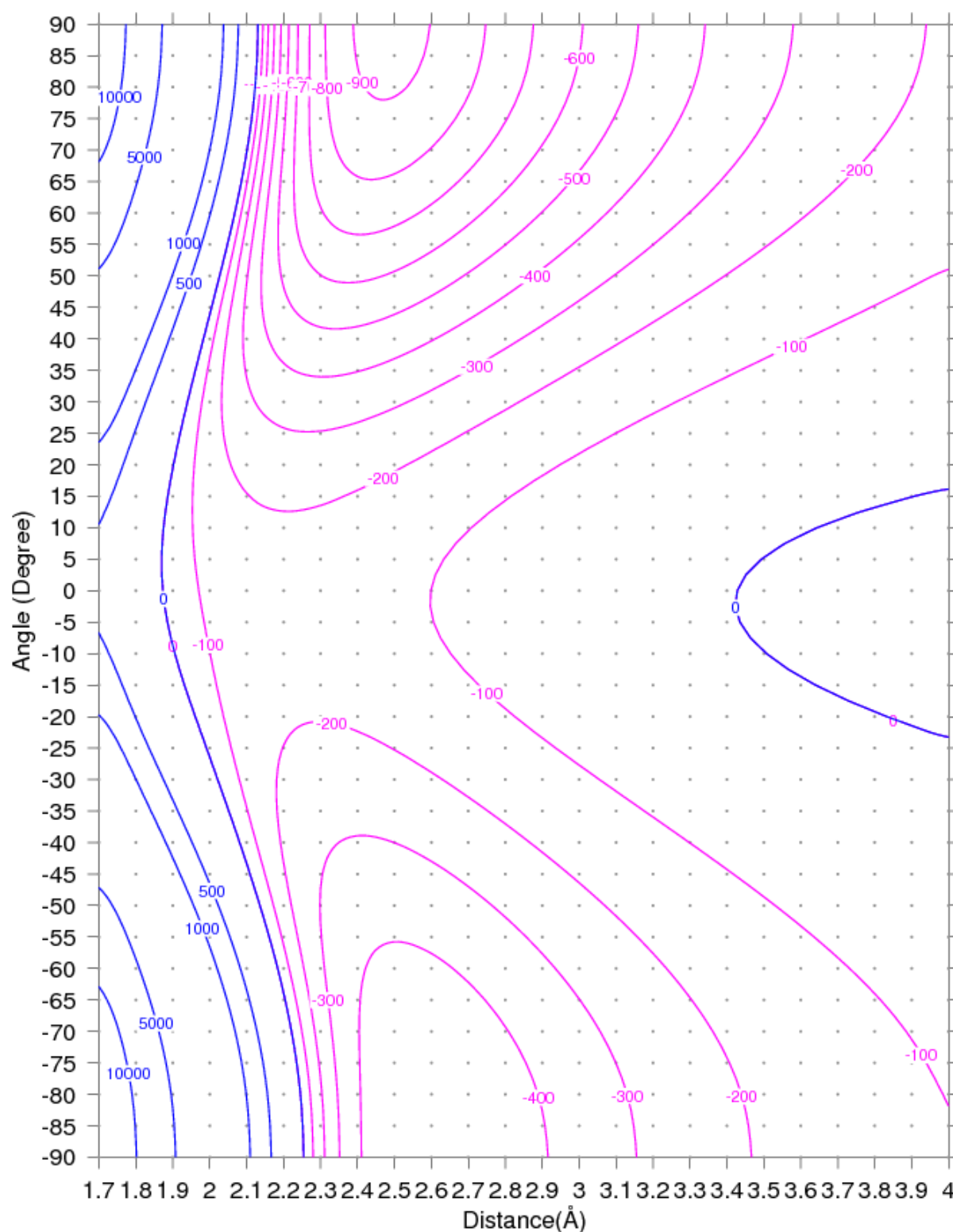


Figure 5.2.6: Counterpoise corrected binding energy surface of $\text{Cu}^+(^1\text{S}) + \text{NO}(^2\Pi) \rightarrow \text{CuNO}^+(^2\text{A}'')$ as a function of the distance between Cu atom and NO center and angle as described in Fig. 4.0.1 using UCCSD(T)/Cu=ECP10MDF-AVTZ, N=AVTZ, O=AVTZ. The dots represent the binding energy calculated at different geometries.

To know the optimized parameters of the stable and the metastable structures of the positively charged coinage metals nitrosyl complexes, a full optimization calculation and frequency calculation were done and the results are summarized in Tab. 5.2.1, 5.2.2.

Complex	Molecular state	$r_{\text{M-N}}$ (Å)	$r_{\text{N-O}}$ (Å)	$\angle\text{MNO}$ Degree	ΔE meV	BSSE meV	ΔZPE meV	$\text{E}_{\text{CP}+\Delta\text{ZPE}}$ meV
AuNO^+	${}^2\text{A}'$	2.079	1.135	125.2	0	-14.4	38.6	-1299.9
	${}^2\text{A}''$	2.080	1.146	180.0	+472.0	-41.8	32.6	-806.5
AgNO^+	${}^2\text{A}'$	2.301	1.144	130.5	0	-18.1	27.4	-640.7
	${}^2\text{A}''$	2.284	1.146	180.0	+115.7	-27.7	26.6	-516.2
CuNO^+	${}^2\text{A}'$	1.932	1.144	135.1	0	-27.0	35.9	-1062.5
	${}^2\text{A}''$	1.893	1.144	180.0	+113.5	-35.8	38.2	-910.5
AuON^+		$r_{\text{M-O}}$	$r_{\text{N-O}}$	$\angle\text{MON}$				
	${}^2\text{A}'$	2.270	1.156	126.1	0	-30.0	19.5	-593.8
	${}^2\text{A}''$	2.320	1.164	180.0	+265.9	-25.9	12.8	-338.7
AgON^+	${}^2\text{A}'$	2.388	1.162	129.7	0	-20.4	16.5	-373.1
	${}^2\text{A}''$	2.397	1.163	180.0	+79.3	-20.9	13.3	-293.3
CuON^+	${}^2\text{A}'$	2.023	1.166	130.2	0	-25.9	21.9	-596.5
	${}^2\text{A}''$	2.006	1.165	180.0	+112.7	-28.2	19.6	-483.8

Table 5.2.1: The optimized parameters of MNO^+ and MON^+ with M: Au, Ag, Cu. The BSSE and ZPE errors. The counterpoise and ZPE corrected binding energy using UCCSD(T)/ECP(60,28,10)MDF-AVTZ, N=AVTZ, O=AVTZ.

It is clear that the ground state for both structures MNO^+ and MON^+ is ${}^2\text{A}'$, and ${}^2\text{A}''$ is the excited state. In addition, the ground state has bent geometry and the excited state has a linear geometry. The MNO^+ complexes have a blue shifts in the N-O stretching frequency while the MON^+ complexes have red shift in N-O stretching frequency.

In details, the NO molecule binds with the gold cation at distance 2.079 Å to form $\text{AuNO}^+({}^2\text{A}')$ which is 0.036 Å longer than the Au-N bond length of the neutral gold nitrosyl complex. The canonical molecular orbitals diagram is similar to the neutral gold nitrosyl's diagram, but the HOMO ($6a'$) is singly occupied. The Mulliken population analysis, see Tab. 6.0.2, shows that the charge of the gold cation decreases from +1 to +0.6 electrons, which mean that the electron density shifts from the NO molecule to the

Complex	Molecular state	N-O stretching cm ⁻¹	M-N stretching cm ⁻¹	M-N-O bending cm ⁻¹	NO shift cm ⁻¹
AuNO ⁺	² A'	1901.1	381.5	229.7	+12.0
	² A''	1966.3	246.2	201.0	+77.2
AgNO ⁺	² A'	1927.2	255.6	147.8	+38.2
	² A''	1963.7	185.7	167.9	+74.6
CuNO ⁺	² A'	1933.6	334.6	199.8	+44.5
	² A''	1979.3	299.4	228.6	+90.2
AuON ⁺		N-O stretching	M-O stretching	M-O-N bending	
	² A'	1746.2	294.1	163.2	-142.9
	² A''	1839.0	154.4	102.0	-50.1
AgON ⁺	² A'	1825.5	208.8	120.9	-63.6
	² A''	1850.2	148.5	104.3	-38.9
CuON ⁺	² A'	1803.3	279.2	158.9	-85.8
	² A''	1843.0	230.1	130.9	-46.1

Table 5.2.2: The vibrational frequencies of MNO⁺ and MON⁺ with M: Au, Ag, Cu. The NO shift is calculated as a difference of N-O stretching frequency and the free NO frequency (1889.1 cm⁻¹) using UCCSD(T)/ECP(60,28,10)MDF-AVTZ.

empty 6s and 6p orbitals of the gold cation. This explains the shortening of the NO bond length in the AuNO⁺(²A') complex, whereas the electron density become less in the antibonding orbital and thus the bond order of NO increases and its bond length decreases, thus it has a blue shifts in the N-O stretching frequency.

Regarding the excited state (²A''), it differs from the ground state mainly by the HOMO orbital, it is an antibonding orbital consisting from the combination of the NO (π_x^*) orbital and the gold d_{xz} orbital and the amount of the charge transfer from NO molecule to the gold cation is less than by 0.03 electrons, hence, the N-O bond length is a bit longer than the corresponding bond of the ground state (²A'). The antibonding nature of the HOMO makes the dative covalent bond weaker than the dative bond of the (²A') state. Therefore, the binding energy of (²A'') is less in magnitude than the binding energy of (²A') state. In addition, the (²A'') state has an imaginary vibrational frequency (375.1 cm⁻¹), which mean it is unstable state.

About the AgNO^+ complexes, the length of Ag-N and N-O bonds are longer than the corresponding bonds in the ($\text{AuNO}^+(^2A')$) by 0.222 \AA , which reflects a weaker interaction between the silver cation and the NO molecule. The orbital diagram of $\text{AgNO}^+(^2A')$ is similar to the diagram $\text{AuNO}^+(^2A')$ where the HOMO is a bonding orbital that constitutes from the NO molecular orbital π^* and the empty silver 5s atomic orbital, this explains the bent shape of $\text{AgNO}^+(^2A')$. In addition, the charge of silver cation decreases from +1 to +0.8 because there is an electron density shift, 0.2 electrons, from NO π^* to the empty 5s and 5p orbitals. Therefore, the NO binds with silver cation through a dative bond.

The first excited state of AgNO^+ is $^2A''$, it is higher in energy than the ground state by +115.7 meV, which is less than the excitation energy of AuNO^+ by 75%. The HOMO is an antibonding orbital that constitutes from π_x^* NO molecular orbital and d_{xy} silver orbital. In addition, there is an electron density transfer, 0.2 electrons, from the NO molecule to silver cation. Therefore, the $\text{AgNO}^+(^2A'')$ has a dative covalent bond but it is weaker than of the $\text{AgNO}^+(^2A')$ because of antibonding nature of its HOMO. The same as for $\text{AuNO}^+(^2A'')$, the excited state $\text{AgNO}^+(^2A'')$ have an imaginary vibrational frequency (179.4cm^{-1}), which mean it is unstable state.

Regarding the CuNO^+ complex, it has a bent shape because its HOMO is a bonding orbital that result from the combination of NO π^* molecular orbital and copper 4s atomic orbital. Moreover, the copper cation binds with the NO molecule with one electron dative covalent bond because its canonical molecular orbital diagram is similar to Fig. 5.1.10, and the HOMO is singly occupied orbital and there is an electron density transfer (0.32 electrons) from the NO molecule to the copper cation based on Mulliken charge analysis in Tab. 6.0.2.

Furthermore, the excited state of $\text{CuNO}^+(^2A'')$ is higher in energy by 113.5 meV from the ground state. It has linear structure and its canonical molecular orbitals differs from the ground state in HOMO, it is antibonding orbitals that results from the combination of the copper d_{xz} orbital with the NO π^* orbital which make the bond weaker than ground state. In addition, the amount of the charge transfer from the NO to the copper cation is about 0.34 electrons which is slightly larger than the ground state, this makes the magnitude of NO frequency shift larger. The same as $\text{AuNO}^+(^2A'')$ and $\text{AgNO}^+(^2A'')$, the excited state $\text{CuNO}^+(^2A'')$ have an imaginary vibrational frequency (208.5cm^{-1}), which mean it

is unstable state.

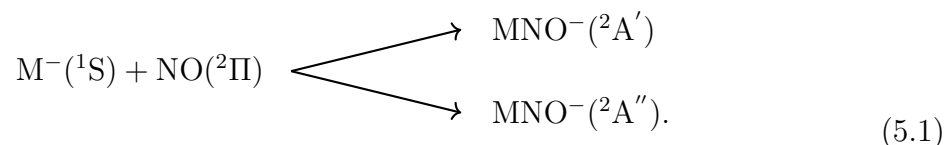
About the metastable structures of MON^+ , it is clear that the bond length between the metal and the oxygen is longer than the bond length between the metal and the nitrogen and the N-O bond length is nearly equal or longer than the bond length of the free NO molecule. Therefore, all the MON^+ complexes have red shifts in NO stretching frequency. In addition, each excited state have imaginary frequency, which are 248.4cm^{-1} , 137.3cm^{-1} , 175.9cm^{-1} for $AuNO^+(^2A'')$, $AgNO^+(^2A'')$, $CuNO^+(^2A'')$, respectively. Thus, all the excited states are unstable states.

In addition, the magnitude of the binding energies of MON^+ is less than the binding energies of MNO^+ because the HOMO of the NO molecule is not symmetric, the lobe on the oxygen atom is smaller than the lobe on the nitrogen atom, thus, the overlap between the metal cation and the NO molecule from oxygen side is less than the nitrogen side. This make the binding energy of MON^+ complexes weaker than MNO^+ complexes. In conclusion, the red shift in the NO stretching frequency and the magnitude of the binding energy are the criteria that distinguish $AuON^+$ from $AuNO^+$ complexes.

Finally, all the MNO^+ and MON^+ complexes dissociate if the metal cation rotates to be perpendicular to the NO molecule and then move away.

5.3 2D-PESs of MNO^- complex

The interaction of the ground state of the coinage metal anion (^1S) with the NO molecule ($^2\Pi$) produces two different states of the coinage mononitrosyl anion MNO^- , $^2\text{A}'$, $^2\text{A}''$, depending on C_s point group:



Based on Eq. 5.1, I have calculated two PESs for each MNO^- , see Figs. 5.3.1 - 5.3.6. The PES of $\text{AuNO}^-(^2\text{A}')$ is repulsive until 3.6 Å, then two shallow minima (m_1, m_2) appear. The first minimum at $d = 3.9$ Å and $\alpha = 80^\circ$ with binding energy -20 meV. The second minimum at $d = 3.9$ Å and $\alpha = -80^\circ$ with binding energy -100 meV. This mean that the gold anion have dispersive interaction with the NO molecule due to the far distance and weak binding energy.

About the PES of $\text{AuNO}^-(^2\text{A}'')$ state, the attractive interaction starts smoothly from $d = 2.4$ Å and continue after 4 Å. The strongest binding energy (-80 meV) occurs between 2.9 Å and 4 Å and $\alpha = 30^\circ$ and $\alpha = -10^\circ$. This mean that the gold anion binds with the NO molecule from nitrogen side and form a bent AuNO^- . The bent $\text{AuNO}^-(^2\text{A}'')$ complex dissociate if the gold anion rotates to $\alpha = 55^\circ$ and then move away.

About the AgNO^- , the $^2\text{A}'$ state is totally repulsive. The $^2\text{A}''$ state has a wide minimum as $\text{AuNO}^-(^2\text{A}'')$ state with binding energy -50 meV. Thus, the silver anion binds with the NO molecule weakly from the nitrogen side and form a bent AgNO^- complex. It dissociates if the silver anion rotates to $\alpha = 50^\circ$ and then move away.

Regarding the CuNO^- , the $^2\text{A}'$ state is totally repulsive as AgNO^- . The $^2\text{A}''$ state has a minimum in nitrogen region at $d = 2.2$ Å and $\alpha = 45^\circ$ with binding energy -400 meV. Thus, the copper anion binds with the NO molecule from nitrogen side and forms a bent $\text{CuNO}^-(^2\text{A}'')$ which have stronger binding energy than the corresponding states of AuNO^- and AgNO^- . It dissociates by rotating the anion to $\alpha = 65^\circ$ or $\alpha = 15^\circ$ and then move away.

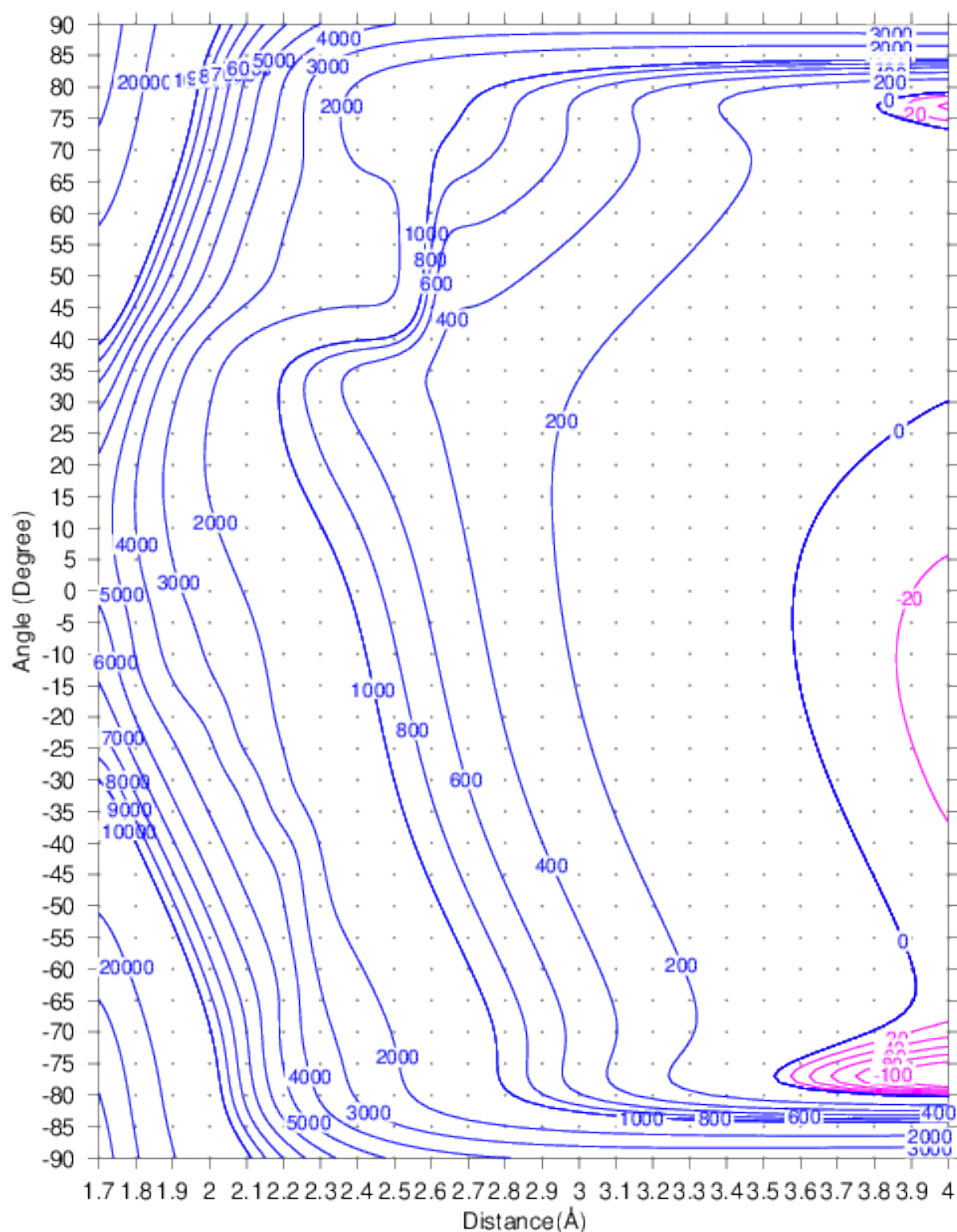


Figure 5.3.1: Counterpoise corrected binding energy surface of $\text{Au}^-(^1\text{S}) + \text{NO}(^2\Pi) \rightarrow \text{AuNO}^-(^2\text{A}')$ as a function of the angle and the distance between Au atom and NO center as described in Fig. 4.0.1 using UCCSD(T)/Au=ECP60DF-AVTZ, N=AVTZ, O=AVTZ. The dots represent the binding energy calculated at different geometries.

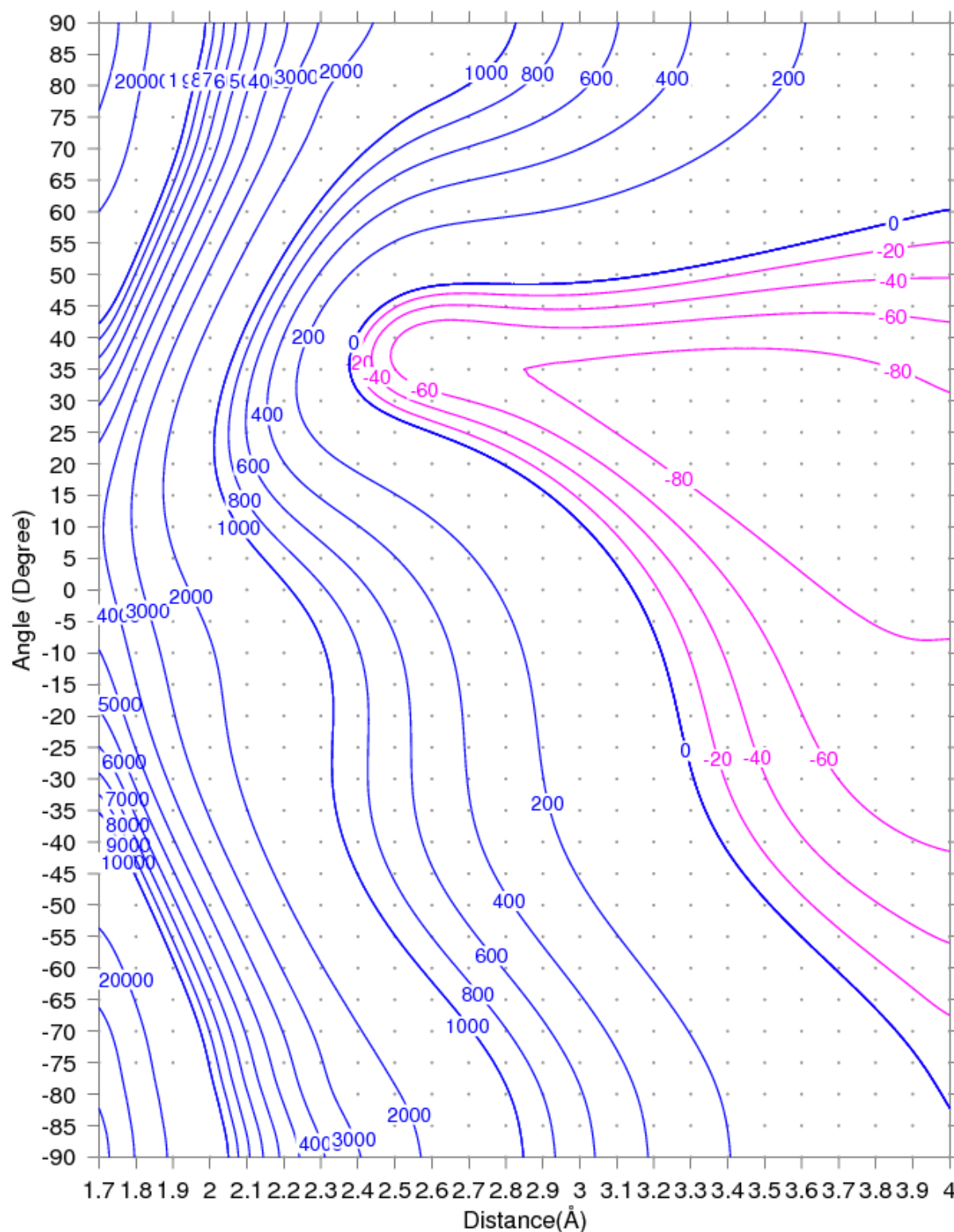


Figure 5.3.2: Counterpoise corrected binding energy surface of $\text{Au}^-(^1\text{S}) + \text{NO}(^2\Pi) \rightarrow \text{AuNO}^-(^2\text{A}'')$ as a function of the angle and the distance between Au atom and NO center as described in Fig. 4.0.1 using UCCSD(T)/Au=ECP60DF-AVTZ, N=AVTZ, O=AVTZ. The dots represent the binding energy calculated at different geometries.

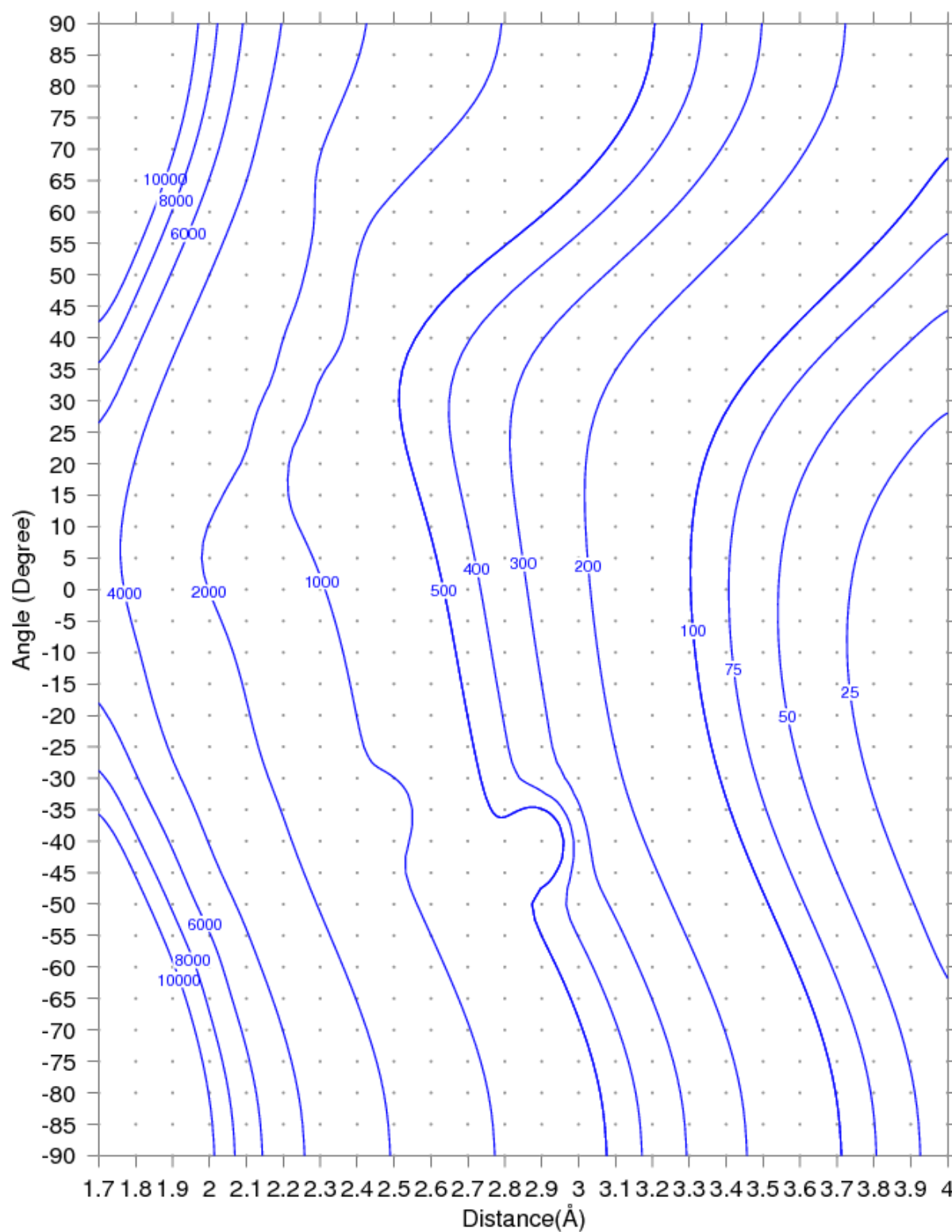


Figure 5.3.3: Counterpoise corrected binding energy surface of $\text{Ag}^-({}^1\text{S}) + \text{NO}({}^2\Pi) \rightarrow \text{AgNO}^-({}^2\text{A}')$ as a function of the angle and the distance between Ag atom and NO center as described in Fig. 4.0.1 using UCCSD(T)/Ag=ECP28MDF-AVTZ, N=AVTZ, O=AVTZ. The dots represent the binding energy calculated at different geometries.

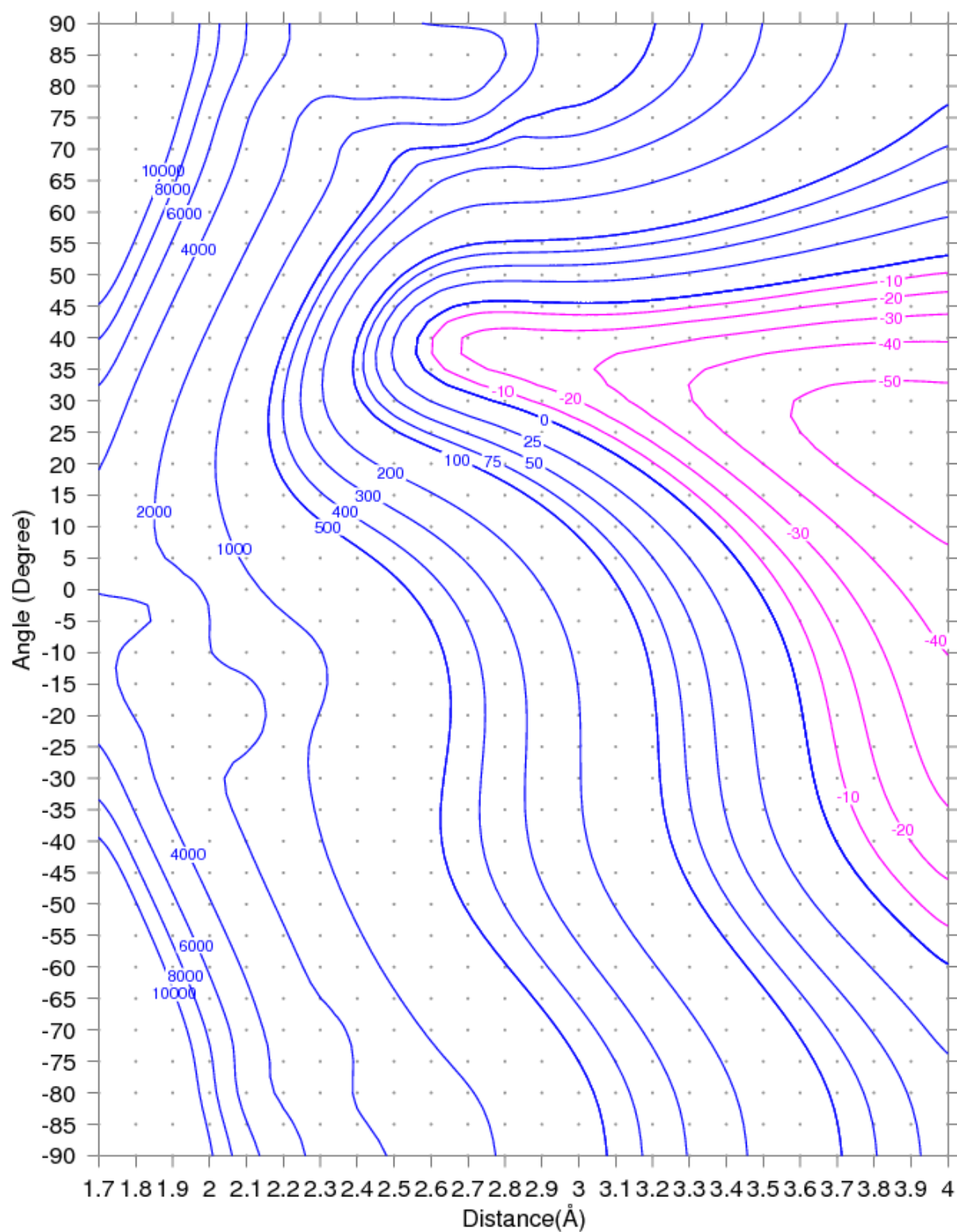


Figure 5.3.4: Counterpoise corrected binding energy surface of $\text{Ag}^-({}^1\text{S}) + \text{NO}({}^2\Pi) \rightarrow \text{AgNO}^-({}^2\text{A}'')$ as a function of the angle and the distance between Ag atom and NO center as described in Fig. 4.0.1 using UCCSD(T)/Ag=ECP28MDF-AVTZ, N=AVTZ, O=AVTZ. The dots represent the binding energy calculated at different geometries.

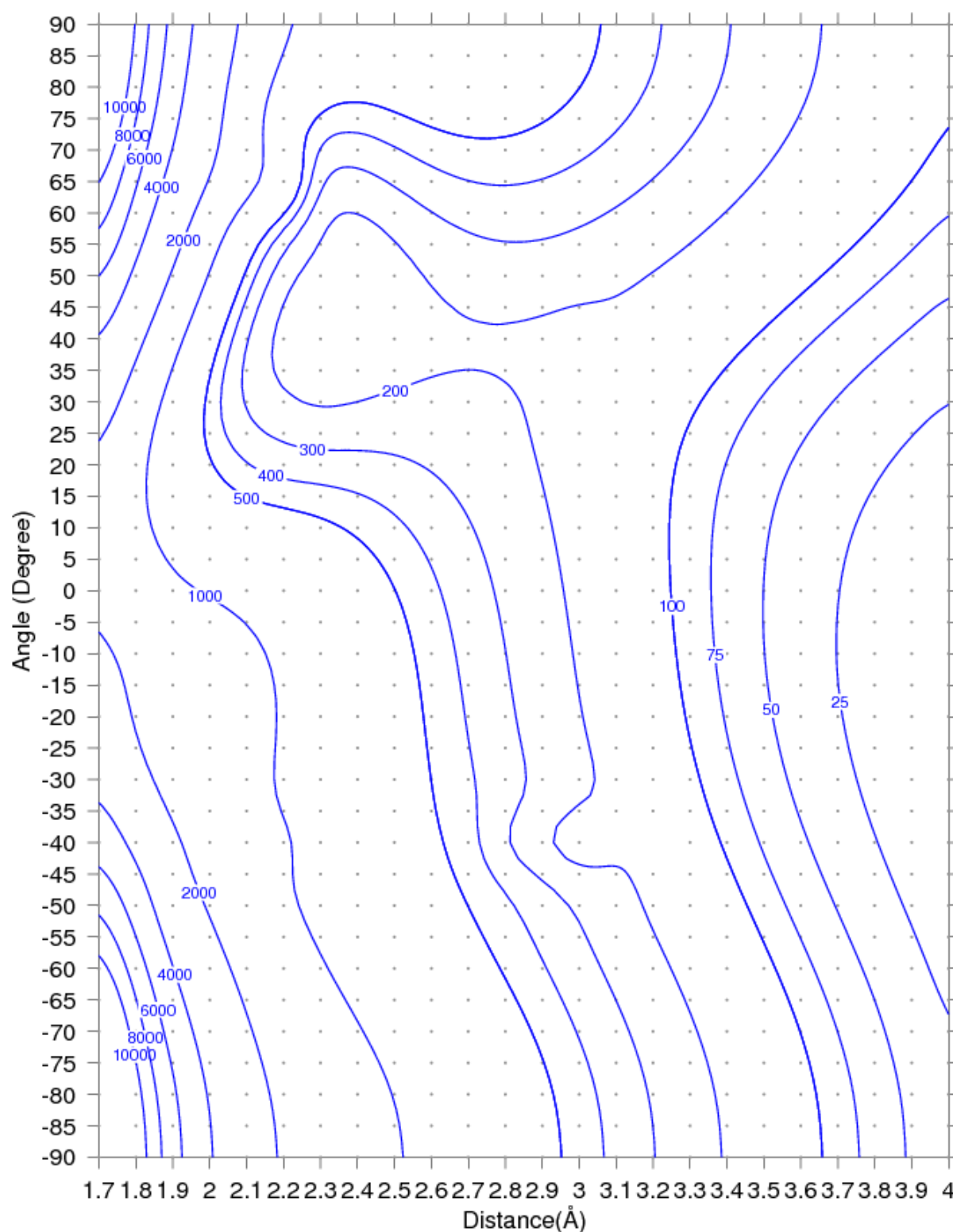


Figure 5.3.5: Counterpoise corrected binding energy surface of $\text{Cu}^-(^1\text{S}) + \text{NO}(^2\Pi) \rightarrow \text{CuNO}^-(^2\text{A}')$ as a function of the distance between Cu atom and NO center and angle as described in Fig. 4.0.1 using UCCSD(T)/Cu=ECP10MDF-AVTZ, N=AVTZ, O=AVTZ. The dots represent the binding energy calculated at different geometries.

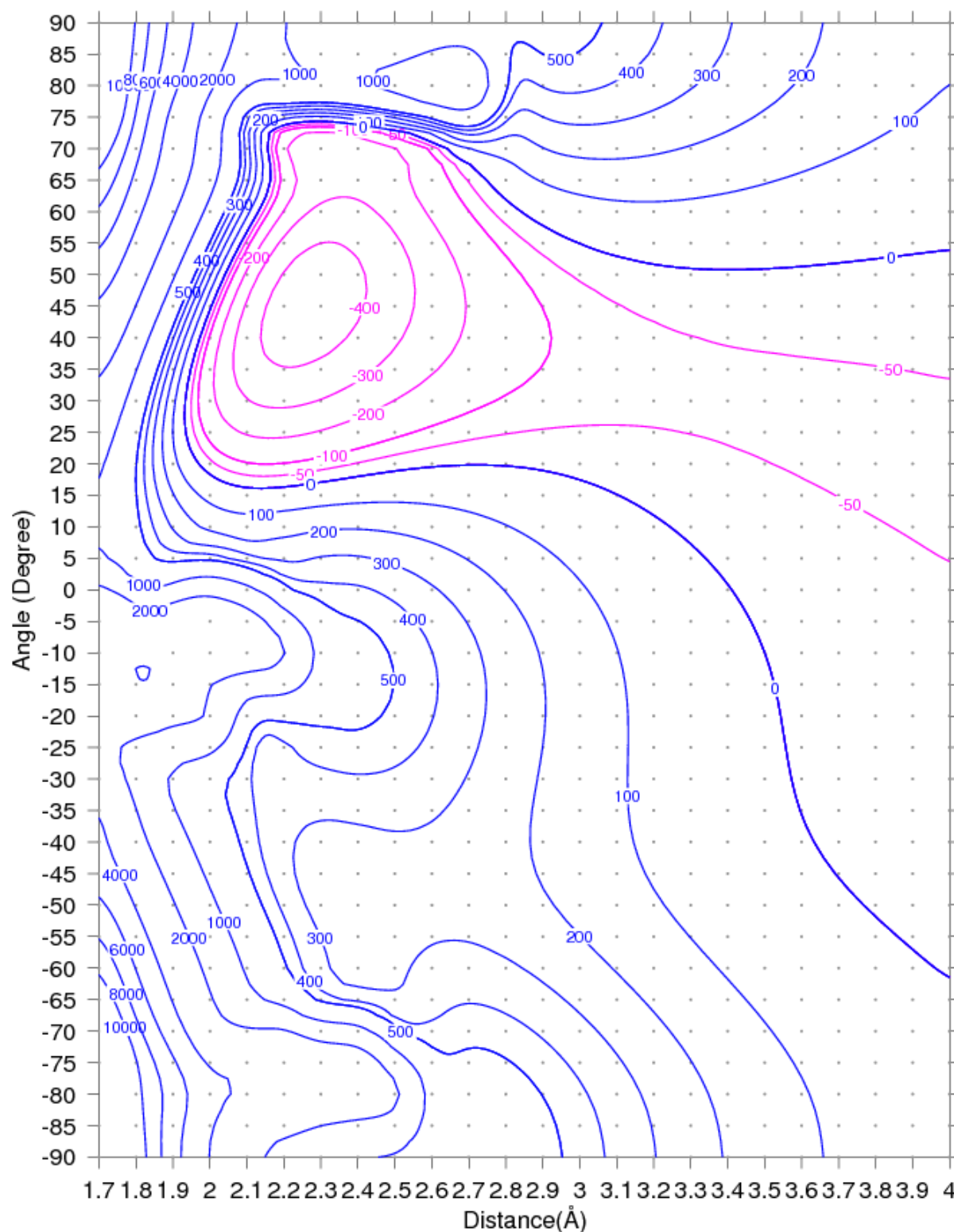


Figure 5.3.6: Counterpoise corrected binding energy surface of $\text{Cu}^-({}^1\text{S}) + \text{NO}({}^2\Pi) \rightarrow \text{CuNO}^-({}^2\text{A}'')$ as a function of the distance between Cu atom and NO center and angle as described in Fig. 4.0.1 using UCCSD(T)/Cu=ECP10MDF-AVTZ, N=AVTZ, O=AVTZ. The dots represent the binding energy calculated at different geometries.

The optimized parameters and the vibrational frequencies for each bond state are summarized in Tabs. 5.3.1 , 5.3.2.

Complex	Molecular state	d _{Au-N} Å	d _{N-O} Å	∠AuNO Degree	ΔE meV	BSSE meV	ΔZPE meV	E _{CP+ΔZPE} meV
AuNO ⁻	² A''	2.146	1.220	116.2	0	+107.5	11.0	-342.8
	² A'	4.316	1.156	67.8	215.6	-6.1	0.3	-26.1
AgNO ⁻	² A''	2.224	1.227	118.3	0	+154.3	3.0	-358.0
CuNO ⁻	² A''	1.869	1.241	120.3	0	+203.0	14.3	-957.3

Table 5.3.1: The optimized bond parameters of MNO⁻ with M: Au, Ag, Cu. The r_{M-N} and ∠MNO are different than the angle (α) and the distance (d) in Fig. 4.0.1. The basis set superposition error(BSSE), zero point energy (ZPE) and the counterpoise ZPE corrected binding energy using UCCSD(T)/ECP(60,28,10)MDF-AVTZ.

Complex	Molecular state	N-O stretching cm ⁻¹	M-N stretching cm ⁻¹	M-N-O bending cm ⁻¹	NO shift cm ⁻¹
AuNO ⁻	² A''	1469.9	398.7	197.1	-419.1
	² A'	1895.8	-	-	6.7
AgNO ⁻	² A''	1421.0	339.5	175.7	-468.1
CuNO ⁻	² A''	1408.3	465.5	245.6	-408.8

Table 5.3.2: The vibrational frequencies of MNO⁻ with M: Au, Ag, Cu. The NO shift is calculated as a difference of N-O stretching frequency and the free NO frequency (1889.1 cm⁻¹) using UCCSD(T)/ECP(60,28,10)MDF-AVTZ.

The ground state of AuNO⁻ is ²A'', its HOMO is an antibonding orbital consisting from the NO molecular orbital π* and the Au atomic orbital d_{yz}. In addition, the Mulliken population analysis, Tab. 6.0.3, shows that the charge of gold anion increases from -1 to -0.88 which mean there is a charge transfer (0.12 electrons) from Au anion to the NO molecule that leads to elongating the NO bond by 0.063 Å hence, red shift in NO stretching frequency is calculated. Based on charge transfer, the NO molecule binds with the gold anion through a dative covalent bond.

The first excited state of AuNO⁻ is ²A', it is weakly bound state because the distance between the gold anion and the nitrogen is long in comparison with the ground state and the NO bond length is equal to the free NO molecule. In addition, there is no overlap

between the molecular orbitals of the NO and the atomic orbitals of the Au anion, and there is no charge transfer between them, see Tab. 6.0.3. This means that there is an attractive van der Waals force between the Au anion and the NO molecule but no chemical bond.

About the silver mononitrosyl anion AgNO^- , the ground state is $^2A''$ as the AuNO^- complex. Its HOMO is an antibonding orbital consisting from the NO molecular orbital π^* and the Ag atomic orbital d_{yz} . In addition, the Mulliken population analysis, Tab. 6.0.3, shows that there is a charge transfer (0.12 electrons) from Ag anion to the NO molecule that leads to elongating the NO bond by 0.07 Å. This leads to red shift in NO stretching frequency. Based on charge transfer, the NO molecule binds with the silver anion through a dative covalent bond.

The ground state of the copper mononitrosyl anion CuNO^- is $^2A''$ as AuNO^- and AuNO^- complexes. The NO bond length is longer than the free NO by 0.084 Å which leads to red shifts in NO stretching frequency. The HOMO is an antibonding orbital consisting from NO molecular orbital π^* and the Cu atomic orbital d_{xz} . In addition, there is a charge transfer (0.29 electrons) from the copper anion to the NO molecule, hence, dative bond is formed.

Finally, the ground state of MNO^- complexes is $^2A''$ in all cases, it has bent geometry, red shift in N-O stretching frequency and dative bond between the anion and the NO molecule. There are two notes about the MNO^- . The BSSE have positive values instead of negative values, and there is a big difference in the binding energy values of the MNO^- in the 2D-PES and in Tab. 5.3.1. This is because of the NO molecule, its bond length in the complex longer than the free NO molecule, thus the energy of the NO molecule used in calculating the binding energy is higher than its ground state energy (unrelaxed molecule) even it uses the basis set of the metal which lead to positive BSSE. The value of the BSSE of NO is +146.0, +187.5, +261.6 in AuNO^- , AgNO^- , CuNO^- , respectively, while the BSSE of the anion is negative. About the difference in the binding energy values, the calculation of 2D-PES were done based on frozen (relaxed) NO molecule (the ground state of the NO molecule with equilibrium bond length 1.157 Å) while in Tab. 5.3.1 the NO molecule were unrelaxed.

5.4 Potential energy surface of M_2NO

In analogy to CO, I have investigated the binding of the coinage metal dimer($^1\Sigma$) with NO molecule ($^2\Pi$) by calculating the PES of the counterpoise corrected binding energy of M_2NO at different distances of different configurations as explained in Tab. 4.3.1, with replacing the CO molecule with NO molecule. The PESs are collected in Fig. 5.4.1.

It is clear that the gold dimer binds with NO molecule from nitrogen side much stronger (six times) than the oxygen side. The best configuration to bind the NO molecule with the metal dimer is the linear configuration, then comes the parallel configuration and then the NO-hat configuration. The other configurations have very weak binding energy, Tab. 5.4.1 summarizes the binding energies of the different configuration and their corresponding distance.

In addition, I have calculated 2D-PES that describes the transforming the linear $Au_2 - NO$ into the linear $Au_2 - ON$ by passing through NO-hat based on the geometry of Fig. 4.3.2. The 2D-PES is shown in Fig. 5.4.2. It has only one minimum around angle 36° and distance 2.6 \AA with binding energy -500 meV . This means that the most stable structure is bent structure with $\angle N Au Au = 36^\circ$. Hence, increasing the number of gold atom to two atoms decreases the binding energy by 51% which is opposite to Au_2CO .

Regarding the silver dimer, the strength of binding energy and the best configuration is different than the gold dimer. The best configuration to bind the silver dimer with the NO molecule from nitrogen side is the linear configuration, then the NO-hat configuration. But when the silver dimer binds from oxygen side, the best configuration is the NO-hat configuration then comes the linear configuration. The other configurations have very weak binding energy. What is noticeable is that the binding energy of NO with silver atom is 3 times more than the silver dimer. Hence, increasing the number of silver atom to two atoms decreases the binding energy by 71% which is opposite to Ag_2CO .

About the copper dimer, it is clear that the interaction of the copper dimer with the NO molecule is the strongest among the coinage metals dimer. The best configuration to bind the copper dimer with the NO molecule from nitrogen side is the linear configuration, then the NO-hat configuration then the parallel configuration, there is no attractive interaction when the complex has L-shape and T-shape configurations.

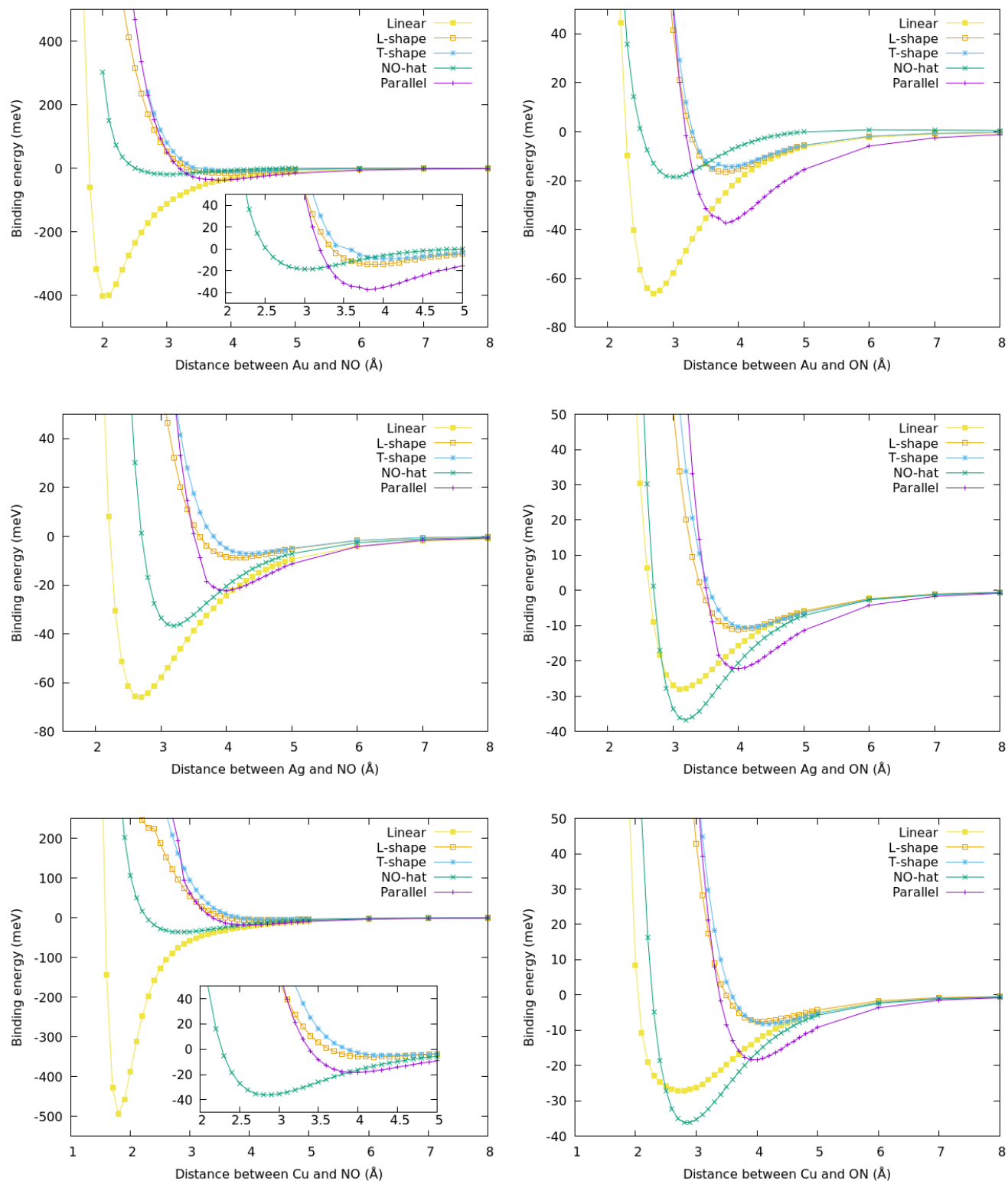


Figure 5.4.1: Counterpoise corrected binding energy of $M_2(^1\Sigma) + NO(^2\Pi) \rightarrow M_2 - NO$, with M : Au, Ag, Cu as a function of the distance between N atom or O atom and coinage metals dimer as described in the Fig. 4.3.1 using UCCSD(T)/ECP(10,28,60)MDF-AVTZ, N=AVTZ, O=AVTZ. The subfigures on the right are zoom in for M-N distance.

The behavior is different when the copper dimer binds from oxygen side, the best configuration is the NO-hat configuration then comes the linear configuration, then the parallel configuration, and there is very weak interaction when complex have L-shape and T-shape configurations. The binding energy of Cu_2NO decrease by 26.4% when the number of copper atom increases to two atoms.

In conclusion, the best configuration for binding the NO molecule with coinage metal dimer is the linear configuration from nitrogen side. In addition, the binding energy decreases as the number of atom is increased to two atoms. Finally, the binding of the NO molecule with copper dimer is the strongest among the coinage metals dimer then comes the gold dimer, then the silver dimer which is not the same trend of the binding energy of MNO complexes.

shape	$X_2 - NO$					
	Gold		Silver		Copper	
	E_{CP} meV	d_{Au_2-N} Å	E_{CP} meV	d_{Ag_2-N} Å	E_{CP} meV	d_{Cu_2-N} Å
Linear	-400.2	2.0	-66.0	2.7	-493.8	1.8
L-shape	-14.4	3.9	-8.8	4.2	unbound	-
T-shape	-9.2	4.1	-7.1	4.4	unbound	-
NO-hat	-18.7	3.0	-36.7	3.2	-36.1	2.8
Parallel	-37.5	3.8	-22.3	4	-18.4	4.0
shape	$X_2 - ON$					
	E_{CP}	d_{Au_2-O}	E_{CP}	d_{Ag_2-O}	E_{CP}	d_{Cu_2-O}
	meV	Å	meV	Å	meV	Å
Linear	-66.2	2.7	-27.9	3.1	-27.1	2.8
L-shape	-16.4	3.8	-11.0	4.0	-7.6	4.1
T-shape	-15.1	3.6	-10.6	4.1	-8.1	4.2

Table 5.4.1: Counterpoise corrected binding energy of $M_2 - NO$ and $M_2 - ON$, where M: Au, Ag and Cu for different configurations and the corresponding distance between the metal and nitrogen or oxygen atoms based on the geometry described in Tab. 4.3.1 calculated by UCCSD(T)/ECP(60, 28, 10)MDF-AVTZ. The CO-hat and parallel configurations are the same for $M_2 - NO$ and $M_2 - ON$

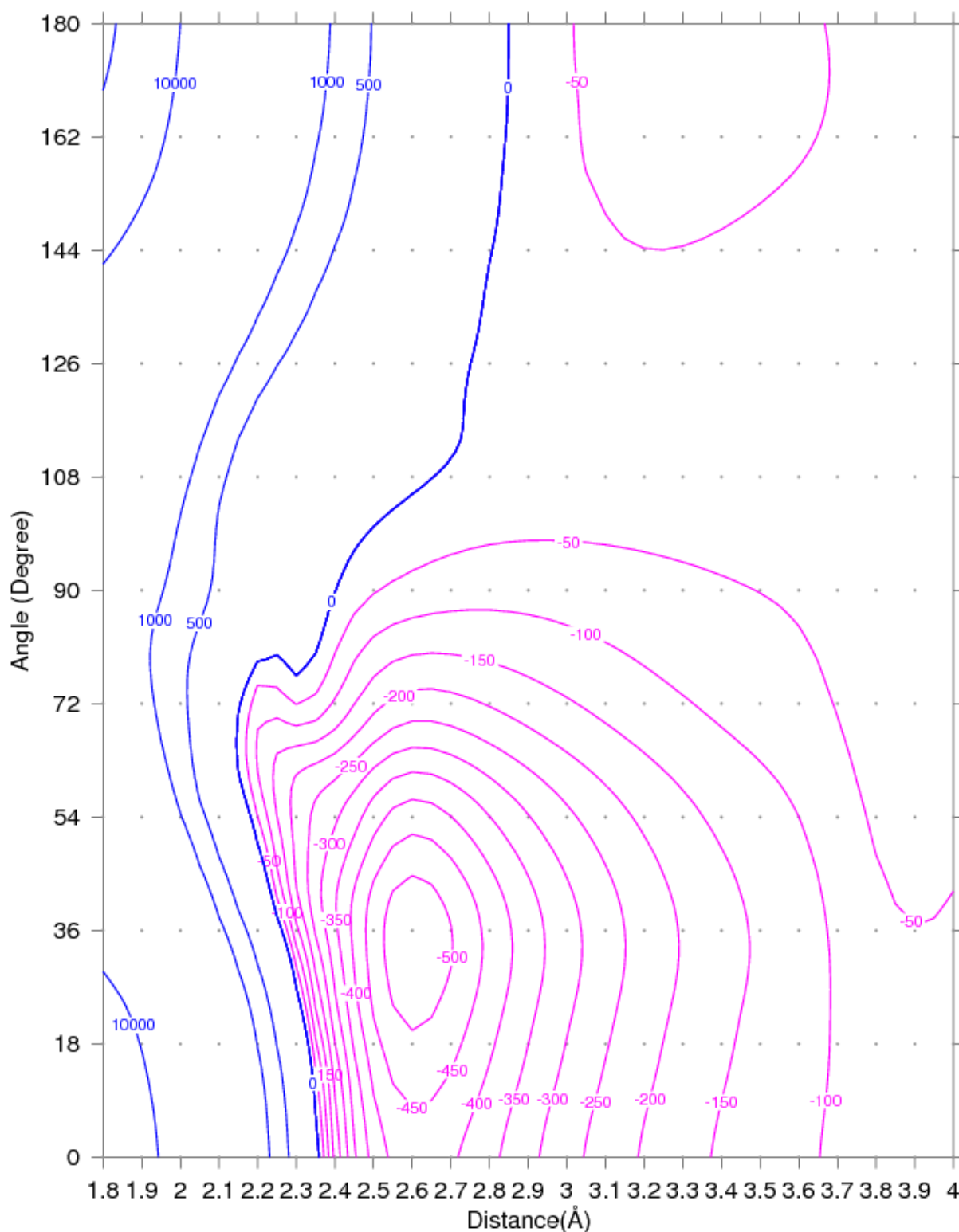


Figure 5.4.2: 2-dimensions Counterpoise corrected binding energy surface of Au_2NO as a function of the distance between Au atom and NO center and the angle as described in Fig. 4.3.2 using UCCSD(T)/Au=ECP60MDF-AVTZ, N=AVTZ, O=AVTZ. The dots represent the binding energy calculated at different geometries.

CHAPTER 6

Conclusion

The potential energy surfaces for binding the CO molecule and the NO molecule with the neutral and charged coinage metals atoms were calculated using UCCSD(T) method with effective core potential for the coinage metals atom and augmented valence-triple-zeta basis set. Here, I will compare the reaction of the CO molecule toward the coinage metals atoms and dimers with the reaction of the NO molecule.

Based on Wigner-Witmer rules, the reaction of the CO ground state with the coinage metal atoms or its ions ground state always produce single states. While the reaction of the NO ground state with the coinage metal atoms or ions ground state produce multiple states. Therefore, I have calculated 9 PESs for $MCO^{0,\pm}$ and 21 PESs for $MNO^{0,\pm}$.

The 2D-PESs of MCO complexes have attractive and repulsive regions and one minimum; the attractive region of AuCO and CuCO are localized in carbon region and the minimum occur at short distances, 2.5 Å and 2.4 Å, respectively. Thus, bent AuCO, CuCO complexes are formed. While in AgCO case, the attractive region is spread over the entire range of α and $d \geq 4$ Å.

Each MNO complex has three different PESs. The 2D-PESs of the ground states of $MNO(^1A')$ have one smooth minimum and many jumps. The binding energy at the smooth minimum of MNO complexes are stronger than the binding energy at the minimum of the MCO complexes. The 2D-PES of the excited trip states ($^3A', ^3A''$) are either repulsive or have dispersive minima, except the $CuNO(^3A'')$ has a minimum at the nitrogen region with binding energy of -300 meV.

The 2D-PESs of the MCO^+ and the MNO^+ complexes are attractive over the whole range of parameter space and have two minima. The minimum in the carbon/nitrogen region have stronger binding energy than the minimum in the oxygen region. Hence each cation binds with the CO/NO molecule either from the carbon/nitrogen side or from oxygen side, and forms a stable complexes $\text{MCO}^+/\text{MNO}^+$, or metastable complexes $\text{MOC}^+/\text{MON}^+$. In addition, all the positive charged complexes dissociate due bending of the cation to the perpendicular position of the CO/NO molecule. The only difference in the cations behavior is the strength of binding energy which is ranked according to the binding energy strength at the first minimum and second minimum as gold > copper > silver and copper > gold > silver, respectively.

The 2D-PESs predict that the MCO^+ and MOC^+ complexes have linear geometries, and the ground states of MNO^+ and MON^+ (${}^2\text{A}'$) have bent geometries while the excited states (${}^2\text{A}''$) have linear geometries.

The 2D-PESs of the MCO^- complexes and the ground state MNO^- (${}^2\text{A}''$) are similar, the attractive region occurs when the anion is nearly perpendicular to the CO/NO molecule and at $d \geq 4\text{\AA}$ (dispersive minimum) except the CuNO^- (${}^2\text{A}''$), it have a minimum at nitrogen region with binding energy -400 meV. Thus, the negative charged complexes are weakly bound.

The strength of the binding energy for both $\text{MCO}^{0,\pm}$ and $\text{MNO}^{0,\pm}$ increases as the charge of coinage metal increases. As we saw, the binding energies of the negative charged complexes are the weakest then it become stronger in the neutral complexes and then much stronger in the positive charged complexes. The strength of the binding energies are ranked based on the type of the metal for all type of charges as Au > Cu > Ag.

About the isoelectric pairs: MCO , MNO^+ and MCO^- , MNO , there is no correlation between the number of electrons and the shape of the PES. The 2D-PESs of MCO complex have one minimum in the carbon region while the 2D-PESs of MNO^+ complexes have two minima, one in the nitrogen region and the other in the oxygen region. Regarding the MCO^- and the MNO complexes, the 2D-PESs of the former complexes have dispersive minimum while the later complexes have a minimum at shorter interatomic distance with stronger binding energy.

From binding of the CO/NO with one metal atom to the binding with metal dimers, the CO molecule binds with the coinage metal dimer much stronger than with the coinage metal atom, because the MCO complexes have open shell electronic structure while the M_2CO complexes have closed shell electronic structure. The strength of the binding energy of M_2CO complexes have the same trend as the MCO complexes if the M_2 binds with the CO molecule in linear geometry, $Au_2CO > Cu_2CO > Ag_2CO$.

On the contrary, the NO molecule binds with the coinage metal dimer much weaker than with the coinage metal atom, because the $MNO(^1A')$ complexes have close shell electronic structure while the M_2NO complexes have open shell electronic structure. The strength of the binding of the NO molecule with the copper dimer is the strongest among the coinage metals dimer then comes the gold dimer, then the silver dimer which is not the same trend of the binding energy of MNO complexes.

About the bond order, bond type and the optimized geometry, both complexes the AuCO and the CuCO complexes have a bond order of 0.5 and they have bent geometries. In addition, the AuCO complex have a dative bond and the CuCO complex have covalent bond since there is a charge transfer from the CO molecule to the gold atom but not to the copper atom. However, the bond order of the AgCO complex is zero since there is no chemical bond formed, only very small van der Waals attractive interaction occurs between the CO molecule and the Ag atom. Therefore, the AuCO complex have the strongest binding energy, then the CuCO complex and the AgCO complex is the weakest.

About the MNO complexes, they have bent geometries, too. Their bond order is 1, thus their binding energies are stronger than the binding energy of MCO complexes. The NO molecule binds with the gold atom through covalent bond while it binds with the silver and the copper atoms through a dative bond, based on the Mulliken charge analysis.

The MCO^+ complexes have bond order of 1 and a dative bond based on the Mulliken charge analysis. They have linear geometries and they are more stable than the neutral complexes and therefore the interatomic distance between the metal and the carbon is shorter than the corresponding ones in the neutral complexes, and their binding energies are larger in magnitude than the neutral complexes by at least one order of magnitude.

About the MOC^+ complexes, the bonds M-O and C-O are longer than the M-C and C-O

in the MCO^+ complexes. The binding energies are weaker than the MCO^+ complexes, because the overlap between d_{z^2} and 3σ is bigger if it occur from carbon side than oxygen side. Thus, the molecular orbitals are built from the combination of metal (d_{z^2}) and CO (3σ) have lower energies in MCO^+ than in MOC^+ . Based on the change in the CO bond length, the MOC^+ complexes have blue shift in the C-O stretching frequency while the MOC^+ complexes have red shift.

The ground state of the MNO^+ and MON^+ complexes have bond order of 0.5, and bent geometries because of the nature of their HOMO; it is bonding orbital results from NO π^* molecular orbital and the valence s orbital of the metal cation. But, the magnitude of the binding energies of MON^+ is less than the binding energies of MNO^+ because the HOMO of the NO molecule is not symmetric, the lobe on the oxygen atom is smaller than the lobe on the nitrogen atom, thus, the overlap between the metal cation and the NO molecule from oxygen side is less than the nitrogen side. This make the binding energy of MON^+ complexes weaker than MNO^+ complexes. In addition, the MNO^+ and MON^+ complexes differ in the N-O stretching frequency, The MNO^+ complexes have a blue shift in the N-O stretching frequency while the MON^+ complexes have red shift.

About the excited state of the MNO^+ and MON^+ complexes, they have bond order of 0.5, too, and the trend of the binding energies and the N-O stretching frequency are the same as the ground states. They only differ in the geometry, they have linear geometries because their HOMO is antibonding orbital constitutes from the NO molecular orbital (π^*) and the atomic orbital d_{xy} .

Regarding the MCO^- complexes, their bond order is zero because there is no overlap between the anion and the CO orbitals. The interatomic distance between the carbon and the metal are longer than in the neutral and the positive charged complexes and the CO bond length and the C-O stretching frequency is nearly the same as the free CO. Therefore, the van der Waals forces are responsible for the long range attraction between the anion and the CO molecule.

The ground state of MNO^- complexes have bond order of 0.5. They have bent geometries, dative bond based on the Mulliken charge analysis and red shift in N-O stretching frequency. There is a difference in the binding energy values, in the 2D-PES and in the optimized structure since the calculation of 2D-PES were done based on frozen (relaxed)

NO molecule where the NO molecule in binding energy calculation of the optimized structure is unrelaxed.

Those accurate PESs are used to find the vibrational energy levels of the $\text{MCO}^{0,\pm}$ and $\text{MNO}^{0,\pm}$ complexes. In addition, they are used in the quantum dynamics simulations to model the scattering of CO/NO molecules on coinage metal surfaces.

After having completed this comprehensive study on binding of CO/NO molecules with the coinage metal atoms, an insight was won in the aspects behind the catalytic activity of the coinage metals in the CO oxidation and the NO reduction. For a more intuitive understanding of the lack in catalytic activity of the coinage metals, the next step would be the modeling of the CO/NO adsorption on a different cluster of the coinage metals in the presence of the oxygen and hydrocarbon molecules.

Appendix

Monocarbonyle	Atom	s	p	d	Total	Charge
AuCO ⁻ (¹ A')	O	3.77465	4.34105	0.04952	8.16931	- 0.16931
	Au	3.88383	6.01329	10.00217	19.89947	- 0.89947
	C	3.83551	1.95009	0.12379	5.93122	+ 0.06878
AuCO(² A')	O	3.87401	4.35715	0.06781	8.30340	- 0.30340
	Au	3.26724	6.43176	9.72570	19.44584	- 0.44584
	C	3.19050	1.88297	0.14099	5.25076	+ 0.74924
AuCO ⁺ (¹ A')	O	3.84995	4.22977	0.07520	8.15972	- 0.15972
	Au	2.72729	6.26711	9.73217	18.74394	+ 0.25606
	C	3.01357	1.93342	0.10475	5.09634	+ 0.90366
AgCO ⁻ (¹ A')	O	3.77986	4.31937	0.05037	8.15370	- 0.15370
	Ag	3.99587	6.00361	10.00093	20.00042	- 1.00042
	C	3.79470	1.90910	0.12032	5.84588	+ 0.15412
AgCO(² A')	O	3.78819	4.31307	0.05147	8.15678	- 0.15678
	Ag	3.00270	6.00175	9.9988	19.00331	- 0.00331
	C	3.80455	1.89869	0.11534	5.83991	+ 0.16009
AgCO ⁺ (¹ A')	O	3.80761	4.24523	0.07792	8.13611	- 0.13611
	Ag	2.23616	6.15972	9.95236	18.35701	+ 0.64299
	C	3.48605	1.90945	0.07624	5.50688	+ 0.49312
CuCO ⁻ (¹ A')	O	3.82158	4.37982	0.05509	8.26071	- 0.26071
	Cu	4.35253	5.98877	9.88616	20.23014	- 1.23014
	C	3.41982	1.93126	0.13048	5.50915	+ 0.49085
CuCO(² A')	O	3.76723	4.28563	0.06507	8.12253	- 0.12253
	Cu	2.94093	6.26389	9.85081	19.05894	- 0.05894
	C	3.74294	1.91771	0.12000	5.81853	+ 0.18147
CuCO ⁺ (¹ A')	O	3.71424	4.14820	0.07300	7.94076	+ 0.05924
	Cu	2.12015	6.07786	9.89299	18.09313	+ 0.90687
	C	3.87399	1.97429	0.07509	5.96611	+ 0.03389

Table 6.0.1: Mulliken population analysis for the neutral and charged coinage metal monocarbonyle MCO^{±,0} complexes using HF/Au=ECP60MDF-AVTZ, C=AVTZ, O=AVTZ.

Mononitrosyl	Atom	s	p	d	Total	Charge
AuNO ($^1A'$)	O	3.90053	4.31613	0.08496	8.31096	- 0.31096
	Au	3.21961	6.10462	9.73719	19.08084	- 0.08084
	N	3.56601	2.92423	0.09721	6.60820	+ 0.39180
AgNO ($^1A'$)	O	3.86859	4.33043	0.06764	8.27489	- 0.27489
	Ag	2.62805	6.08362	9.96639	18.68736	+ 0.31264
	N	3.76707	3.17595	0.07893	7.03774	- 0.03774
CuNO ($^1A'$)	O	3.88019	4.37688	0.07338	8.33926	- 0.33926
	Cu	2.66768	6.12149	9.92113	18.71684	+ 0.28316
	N	3.64236	3.20552	0.07828	6.94390	+ 0.05610
AuNO $^+(^2A')$	O	3.89463	4.16384	0.10482	8.17438	- 0.17438
	Au	2.35803	6.15208	9.87334	18.40309	+ 0.59691
	N	3.59320	2.74233	0.06915	6.42253	+ 0.57747
AuNO $^+(^2A'')$	O	3.88011	4.20146	0.10544	8.19903	- 0.19903
	Au	2.28896	6.17023	9.89060	18.37166	+ 0.62834
	N	3.59369	2.78738	0.02748	6.42931	+ 0.57069
AgNO $^+(^2A')$	O	3.86784	4.18570	0.09092	8.15497	- 0.15497
	Ag	2.11002	6.07964	9.98738	18.18572	+ 0.81428
	N	3.76992	2.81926	0.05621	6.65931	+ 0.34069
AgNO $^+(^2A'')$	O	3.87610	4.20923	0.09362	8.19026	- 0.19026
	Ag	2.10114	6.08702	9.98991	18.18732	+ 0.81268
	N	3.77400	2.80298	0.02899	6.62242	+ 0.37758
CuNO $^+(^2A')$	O	3.88071	4.17824	0.10199	8.17247	- 0.17247
	Cu	2.22521	6.13264	9.95572	18.31955	+ 0.68045
	N	3.64204	2.80129	0.04824	6.50798	+ 0.49202
CuNO $^+(^2A'')$	O	3.86796	4.20590	0.10762	8.19414	- 0.19414
	Cu	2.23748	6.14972	9.94725	18.34127	+ 0.65873
	N	3.62909	2.80407	0.01194	6.46459	+ 0.53541

Table 6.0.2: Mulliken population analysis for the neutral and positive charged coinage metal mononitrosyl MNO, MNO $^+$ complexes using HF/Au=ECP60MDF-AVTZ, N=AVTZ, O=AVTZ.

Mononitrosyl	Atom	s	p	d	Total	Charge
AuNO ⁻ (² A'')	O	3.89876	4.48362	0.06161	8.45204	- 0.45204
	Au	3.93499	6.11634	9.82385	19.88701	- 0.88701
	N	3.64042	2.90728	0.09332	6.66096	+ 0.33904
AuNO ⁻ (² A')	O	3.81477	4.23726	0.06904	8.12922	- 0.12922
	Au	3.98911	6.00285	10.00178	19.99377	- 0.99377
	N	3.93261	2.85037	0.07865	6.87702	+ 0.12298
AgNO ⁻ (² A')	O	3.89816	4.41989	0.05752	8.38344	- 0.38344
	Ag	3.84349	6.09419	9.94154	19.88638	- 0.88638
	N	3.64890	2.98289	0.08104	6.73019	+ 0.26981
CuNO ⁻ (² A'')	O	3.89511	4.48046	0.05512	8.43865	- 0.43865
	Cu	3.65418	6.18509	9.87197	19.71722	- 0.71722
	N	3.57011	3.16926	0.08585	6.84413	+ 0.15587

Table 6.0.3: Mulliken population analysis for the negative charged coinage metal mononitrosyl MNO⁻ complexes using HF/Au=ECP60MDF-AVTZ, N=AVTZ, O=AVTZ.

Bibliography

- [1] P. Thakur, *Advanced Mine Ventilation: Respirable Coal Dust, Combustible Gas and Mine Fire Control*, Woodhead Publishing, **2018**.
- [2] J. Kašpar, P. Fornasiero, N. Hickey, *Catalysis today* **2003**, *77*, 419–449.
- [3] R. J. Farrauto, R. M. Heck, *Catalysis Today* **1999**, *51*, 351–360.
- [4] L. C. Young, B. A. Finlayson, *AIChE Journal* **1976**, *22*, 343–353.
- [5] R. Isermann, J. Schaffnit, S. Sinsel, *Control Engineering Practice* **1999**, *7*, 643–653.
- [6] W. Ribbens, *Understanding automotive electronics: an engineering perspective*, Butterworth-heinemann, **2017**.
- [7] K. Schürholz, D. Brückner, M. Gresser, D. Abel, *IFAC-PapersOnLine* **2018**, *51*, 742–747.
- [8] H. Ling, Y. Xiu-Min, L. Guo-Liang, X. Nan, *Energy Procedia* **2012**, *17*, 547–554.
- [9] H. Santos, M. Costa, *Energy Conversion and Management* **2008**, *49*, 291–300.
- [10] O. Laguna, M. Domínguez, M. Centeno, J. Odriozola in *New Materials for Catalytic Applications*, Elsevier, **2016**, pp. 81–120.
- [11] N. M. Kinnunen, J. T. Hirvi, K. Kallinen, T. Maunula, M. Keenan, M. Suvanto, *Applied Catalysis B: Environmental* **2017**, *207*, 114–119.
- [12] R. Winderlich, *Journal of Chemical Education* **1948**, *25*, 500.
- [13] J. A. Moulijn, P. W. van Leeuwen, R. A. van Santen, *Catalysis: an integrated approach to homogeneous, heterogeneous and industrial catalysis, Vol. 79*, Elsevier, **1993**.
- [14] S. R. Couto, M. A. Sanromán, *Journal of Food Engineering* **2006**, *76*, 291–302.
- [15] R. Aravindan, P. Anbumathi, T. Viruthagiri, *Indian Journal of Biotechnology* **2007**, *6*, 141–158.

- [16] A. Rajendran, A. Palanisamy, V. Thangavelu, *Brazilian archives of biology and technology* **2009**, *52*, 207–219.
- [17] S. Varadarajan, D. J. Miller, *Biotechnology progress* **1999**, *15*, 845–854.
- [18] R. Rahman, V. Uahengo, D. Likius, *Global Drugs and Therapeutics* **2017**, *2*, 1–6.
- [19] G. W. Huisman, D. Gray, *Current opinion in biotechnology* **2002**, *13*, 352–358.
- [20] J. M. Hawkins, T. J. Watson, *Angewandte Chemie International Edition* **2004**, *43*, 3224–3228.
- [21] P. Tufvesson, J. Lima-Ramos, M. Nordblad, J. M. Woodley, *Organic Process Research & Development* **2010**, *15*, 266–274.
- [22] D. J. Pollard, J. M. Woodley, *TRENDS in Biotechnology* **2007**, *25*, 66–73.
- [23] J. P. Rasor, E. Voss, *Applied Catalysis A: General* **2001**, *221*, 145–158.
- [24] S. Kulprathipanja, *Zeolites in industrial separation and catalysis*, John Wiley & Sons, **2010**.
- [25] K. Tanabe, W. F. Hölderich, *Applied Catalysis A: General* **1999**, *181*, 399–434.
- [26] G. Martino in *Studies in Surface Science and Catalysis, Vol. 130*, Elsevier, **2000**, pp. 83–103.
- [27] M. Iwamoto in *Studies in Surface Science and Catalysis, Vol. 130*, Elsevier, **2000**, pp. 23–47.
- [28] R. Weber, T. Sakurai, H. Hagenmaier, *Applied Catalysis B: Environmental* **1999**, *20*, 249–256.
- [29] C. Gannoun, A. Turki, H. Kochkar, R. Delaigle, P. Eloy, A. Ghorbel, E. M. Gaigneaux, *Applied Catalysis B: Environmental* **2014**, *147*, 58–64.
- [30] S. Guo, K. Heck, S. Kasiraju, H. Qian, Z. Zhao, L. C. Grabow, J. T. Miller, M. S. Wong, *ACS Catalysis* **2017**, *8*, 503–515.
- [31] Y. I. Matatov-Meytal, M. Sheintuch, *Industrial & engineering chemistry research* **1998**, *37*, 309–326.
- [32] P. Fornasiero, *Encyclopedia of Life Support Systems*.
- [33] G. Centi, S. Perathoner, *Applied Catalysis B: Environmental* **2003**, *41*, 15–29.
- [34] M. Hu, Y. Liu, Z. Yao, L. Ma, X. Wang, *Frontiers of Environmental Science Engineering* **2017**, *12*, 3.
- [35] B. Singh, F. Bux, Y. C. Sharma, *Chemical Industry and Chemical Engineering Quarterly* **2011**, *17*, 117–124.

- [36] E. Farnetti, R. Di Monte, J. Kašpar, *Inorganic and bioinorganic chemistry* **2009**, *2*, 50.
- [37] J. L. Margitfalvi, I. Borbáth, M. Hegedűs, E. Tfirst, S. Góbbölös, K. Lázár, *Journal of Catalysis* **2000**, *196*, 200–204.
- [38] B. Kucharczyk, *Environment Protection Engineering* **2008**, *34*, 69–74.
- [39] W. Daniell, N. Lloyd, C Bailey, P. Harrison, *Le Journal de Physique IV* **1997**, *7*, C2–963.
- [40] T. J. Huang, D.-H. Tsai, *Catalysis Letters* **2003**, *87*, 173–178.
- [41] C. A. Sierra-Pereira, E. A. Urquieta-González, *Fuel* **2014**, *118*, 137–147.
- [42] G. Centi, S. Perathoner, *Applied Catalysis A: General* **1995**, *132*, 179–259.
- [43] K.-H. Lin, S.-P. Ju, J.-Y. Li, H.-T. Chen, *Physical Chemistry Chemical Physics* **2016**, *18*, 3322–3330.
- [44] H.-L. Chen, S.-Y. Wu, H.-T. Chen, J.-G. Chang, S.-P. Ju, C. Tsai, L.-C. Hsu, *Langmuir* **2010**, *26*, 7157–7164.
- [45] S. Royer, D. Duprez, *ChemCatChem* **2011**, *3*, 24–65.
- [46] M. Li, X. Wu, Y. Cao, S. Liu, D. Weng, R. Ran, *Journal of colloid and interface science* **2013**, *408*, 157–163.
- [47] K. Bethke, H. H. Kung, *Journal of Catalysis* **1997**, *172*, 93–102.
- [48] B. K. Cho, B. H. Shank, J. E. Bailey, *Journal of Catalysis* **1989**, *115*, 486–499.
- [49] P. Bera, K. Patil, V Jayaram, G. Subbanna, M. Hegde, *Journal of Catalysis* **2000**, *196*, 293–301.
- [50] G. Spezzati, A. D. Benavidez, A. T. DeLaRiva, Y. Su, J. P. Hofmann, S. Asahina, E. J. Olivier, J. H. Neethling, J. T. Miller, A. K. Datye, et al., *Applied Catalysis B: Environmental* **2019**, *243*, 36–46.
- [51] F. Garin, *Applied Catalysis A: General* **2001**, *222*, 183–219.
- [52] R. Klein, A. Shih, *Surface Science* **1977**, *69*, 403–427.
- [53] S. M. McClure, T. S. Kim, J. D. Stiehl, P. L. Tanaka, C. B. Mullins, *The Journal of Physical Chemistry B* **2004**, *108*, 17952–17958.
- [54] R. B. Getman, W. F. Schneider, *The Journal of Physical Chemistry C* **2007**, *111*, 389–397.
- [55] M. Bartram, R. Windham, B. E. Koel, *Surface Science* **1987**, *184*, 57–74.
- [56] J. Segner, W. Vielhaber, G. Ertl, *Israel Journal of Chemistry* **1982**, *22*, 375–379.

- [57] W. Brown, P Gardner, D. King, *Surface science* **1995**, *330*, 41–47.
- [58] U. Schwalke, J. Parmeter, W. Weinberg, *The Journal of chemical physics* **1986**, *84*, 4036–4042.
- [59] J. Liu, X. Zhang, *Applied Surface Science* **2013**, *265*, 274–280.
- [60] J.-b. Li, Z.-q. Jiang, W.-x. Huang, *Chinese Journal of Chemical Physics* **2011**, *24*, 735.
- [61] G. Polzonetti, P. Alnot, C. Brundle, *Surface science* **1990**, *238*, 237–244.
- [62] S. Sato, T. Senga, M. Kawasaki, *The Journal of Physical Chemistry B* **1999**, *103*, 5063–5069.
- [63] A. Hellman, I. Panas, H. Grönbeck, *The Journal of chemical physics* **2008**, *128*, 104704.
- [64] H. Chon, C. D. Prater, *Discussions of the Faraday Society* **1966**, *41*, 380–393.
- [65] Y. Wang, M. Makkee, *Applied Catalysis B: Environmental* **2018**, *221*, 196–205.
- [66] Z. Zhou, M. P. Harold, D. Luss, *Applied Catalysis B: Environmental* **2019**, *240*, 79–91.
- [67] L. Liu, Z. Yao, Y. Deng, F. Gao, B. Liu, L. Dong, *ChemCatChem* **2011**, *3*, 978–989.
- [68] W.-L. Yim, T. Nowitzki, M. Necke, H. Schnars, P. Nickut, J. Biener, M. M. Biener, V. Zielasek, K. Al-Shamery, T. Klüner, et al., *The Journal of Physical Chemistry C* **2007**, *111*, 445–451.
- [69] J. Kim, E. Samano, B. E. Koel, *The Journal of Physical Chemistry B* **2006**, *110*, 17512–17517.
- [70] M. Haruta, T. Kobayashi, H. Sano, N. Yamada, *Chemistry Letters* **1987**, *16*, 405–408.
- [71] M. Haruta, N Yamada, T Kobayashi, S Iijima, *Journal of catalysis* **1989**, *115*, 301–309.
- [72] G. R. Bamwenda, S. Tsubota, T. Nakamura, M. Haruta, *Catalysis Letters* **1997**, *44*, 83–87.
- [73] M. Haruta, *Catalysis today* **1997**, *36*, 153–166.
- [74] M. Haruta, M. Daté, *Applied Catalysis A: General* **2001**, *222*, 427–437.
- [75] M. Haruta, *Cattech* **2002**, *6*, 102–115.
- [76] M. Haruta, *The chemical record* **2003**, *3*, 75–87.
- [77] M. Haruta, *Gold bulletin* **2004**, *37*, 27–36.

- [78] K. Okazaki, S. Ichikawa, Y. Maeda, M. Haruta, M. Kohyama, *Applied Catalysis A: General* **2005**, *291*, 45–54.
- [79] M. Khoudiakov, M. C. Gupta, S. Deevi, *Applied Catalysis A: General* **2005**, *291*, 151–161.
- [80] A. C. Gluhoi, H. S. Vreeburg, J. W. Bakker, B. E. Nieuwenhuys, *Applied Catalysis A: General* **2005**, *291*, 145–150.
- [81] C. C. Chusuei, X. Lai, K. Davis, E. Bowers, J. P. Fackler, D. Goodman, *Langmuir* **2001**, *17*, 4113–4117.
- [82] U. Heiz, A. Sanchez, S. Abbet, W.-D. Schneider, *The European Physical Journal D-Atomic Molecular Optical and Plasma Physics* **1999**, *9*, 35–39.
- [83] A. Sanchez, S. Abbet, U. Heiz, W.-D. Schneider, H. Häkkinen, R. Barnett, U. Landman, *The Journal of Physical Chemistry A* **1999**, *103*, 9573–9578.
- [84] J. Guzman, B. C. Gates, *Journal of the American Chemical Society* **2004**, *126*, 2672–2673.
- [85] D. Cox, R. Brickman, K. Creegan, A. Kaldor, *Zeitschrift für Physik D Atoms Molecules and Clusters* **1991**, *19*, 353–355.
- [86] T. H. Lee, K. M. Ervin, *The Journal of Physical Chemistry* **1994**, *98*, 10023–10031.
- [87] W. Huang, S. Bulusu, R. Pal, X. C. Zeng, L.-S. Wang, *The Journal of chemical physics* **2009**, *131*, 234305.
- [88] W. T. Wallace, R. L. Whetten, *Journal of the American Chemical Society* **2002**, *124*, 7499–7505.
- [89] X. Wu, L. Senapati, S. Nayak, A. Selloni, M. Hajaligol, *The Journal of chemical physics* **2002**, *117*, 4010–4015.
- [90] A. Shiga, M. Haruta, *Applied Catalysis A: General* **2005**, *291*, 6–12.
- [91] L. Molina, B. Hammer, *Applied Catalysis A: General* **2005**, *291*, 21–31.
- [92] T. Choudhary, D. Goodman, *Applied Catalysis A: General* **2005**, *291*, 32–36.
- [93] M. Okumura, Y. Kitagawa, M. Haruta, K. Yamaguchi, *Applied Catalysis A: General* **2005**, *291*, 37–44.
- [94] N. Lopez, J. K. Nørskov, *Journal of the American Chemical Society* **2002**, *124*, 11262–11263.
- [95] R. Coquet, K. L. Howard, D. J. Willock, *Chemical Society Reviews* **2008**, *37*, 2046–2076.

- [96] U. Burghaus, H. Conrad, *Surface science* **1997**, *370*, 17–31.
- [97] J. V. Barth, T. Zambelli, *Surface science* **2002**, *513*, 359–366.
- [98] T. M. Bernhardt, L. D. Socaciu-Siebert, J. Hagen, L. Wöste, *Applied Catalysis A: General* **2005**, *291*, 170–178.
- [99] L. Yu, Y. Shi, Z. Zhao, H. Yin, Y. Wei, J. Liu, W. Kang, T. Jiang, A. Wang, *Catalysis Communications* **2011**, *12*, 616–620.
- [100] L. Lian, P. A. Hackett, D. M. Rayner, *The Journal of chemical physics* **1993**, *99*, 2583–2590.
- [101] D. Tang, Z. Chen, J. Hu, G. Sun, S. Lu, C. Hu, *Physical Chemistry Chemical Physics* **2012**, *14*, 12829–12837.
- [102] H. Liu, D. Ma, R. A. Blackley, W. Zhou, X. Bao, *Chemical Communications* **2008**, 2677–2679.
- [103] D. TIAN, G. YONG, S. LIU, *SCIENTIA SINICA Chimica* **2011**, *41*, 828–833.
- [104] T. M. Bernhardt, J. Hagen, S. M. Lang, D. M. Popolan, L. D. Socaciu-Siebert, L. Wöste, *The Journal of Physical Chemistry A* **2009**, *113*, 2724–2733.
- [105] R. Leuchtner, A. Harms, A. Castleman Jr, *The Journal of chemical physics* **1990**, *92*, 6527–6537.
- [106] P. G. Harrison, I. K. Ball, W. Azelee, W. Daniell, D. Goldfarb, *Chemistry of materials* **2000**, *12*, 3715–3725.
- [107] D. Gamarra, C. Belver, M. Fernández-García, A. Martínez-Arias, *Journal of the American Chemical Society* **2007**, *129*, 12064–12065.
- [108] R. Prasad, P. Singh, *Catalysis Reviews* **2012**, *54*, 224–279.
- [109] D. Tang, J. Zhang, *RSC Advances* **2013**, *3*, 15225–15236.
- [110] Z. Chen, J. Yan, W. Zheng, Q. Jiang, *Scientific reports* **2015**, *5*, 11230.
- [111] M. A. Nygren, P. E. Siegbahn, *The Journal of Physical Chemistry* **1992**, *96*, 7579–7584.
- [112] H. Yu, *The Journal of Chemical Physics* **1978**, *69*, 1755–1763.
- [113] E. Song, Z. Wen, Q. Jiang, *The Journal of Physical Chemistry C* **2011**, *115*, 3678–3683.
- [114] V. Sadykov, S. Tikhov, *Journal of Catalysis* **1997**, *165*, 279–283.
- [115] B. Eren, C. Heine, H. Bluhm, G. A. Somorjai, M. Salmeron, *Journal of the American Chemical Society* **2015**, *137*, 11186–11190.

- [116] S. Sun, D. Mao, J. Yu, Z. Yang, G. Lu, Z. Ma, *Catalysis Science & Technology* **2015**, *5*, 3166–3181.
- [117] C. Vinod, J. N. Hans, B. Nieuwenhuys, *Applied Catalysis A: General* **2005**, *291*, 93–97.
- [118] A. Hussain, D. C. Ferré, J. Gracia, B. Nieuwenhuys, J. Niemantsverdriet, *Surface Science* **2009**, *603*, 2734–2741.
- [119] D. Torres, S. González, K. M. Neyman, F. Illas, *Chemical physics letters* **2006**, *422*, 412–416.
- [120] E. Rienks, G. Van Berkel, J. Bakker, B. Nieuwenhuys, *Surface science* **2004**, *571*, 187–193.
- [121] S. A. Carabineiro, B. E. Nieuwenhuys, *Gold Bulletin* **2009**, *42*, 288–301.
- [122] J. Gong, C. B. Mullins, *Accounts of chemical research* **2009**, *42*, 1063–1073.
- [123] T.-D. Chau, T. V. de Bocarmé, N. Kruse, *Catalysis letters* **2004**, *98*, 85–87.
- [124] J. L. Fajín, M. N. D. Cordeiro, J. R. Gomes, *The Journal of Physical Chemistry C* **2009**, *113*, 8864–8877.
- [125] X. Ding, Z. Li, J. Yang, J. Hou, Q. Zhu, *The Journal of chemical physics* **2004**, *121*, 2558–2562.
- [126] A. Citra, X. Wang, L. Andrews, *The Journal of Physical Chemistry A* **2002**, *106*, 3287–3293.
- [127] J. Lee, J. Schwank, *Journal of Catalysis* **1986**, *102*, 207–215.
- [128] M. Debeila, N. Coville, M. Scurrall, G. Hearne, *Catalysis today* **2002**, *72*, 79–87.
- [129] F. Solymosi, T. Bánsági, T. S. Zakar, *Catalysis letters* **2003**, *87*, 7–10.
- [130] F. Solymosi, T. Bánsági, T. S. Zakar, *Physical Chemistry Chemical Physics* **2003**, *5*, 4724–4730.
- [131] A. Endou, N. Ohashi, S. Takami, M. Kubo, A. Miyamoto, E. Broclawik, *Topics in Catalysis* **2000**, *11*, 271–278.
- [132] O. Olvera-Neria, V. Bertin, E. Poulain, *International Journal of Quantum Chemistry* **2011**, *111*, 2054–2063.
- [133] A. Beniya, Y. Ikuta, N. Isomura, H. Hirata, Y. Watanabe, *ACS Catalysis* **2017**, *7*, 1369–1377.
- [134] Y.-L. Teng, M. Kohyama, M. Haruta, Q. Xu, *The Journal of chemical physics* **2009**, *130*, 134511.

- [135] A. Fielicke, G. von Helden, G. Meijer, B. Simard, D. M. Rayner, *Physical Chemistry Chemical Physics* **2005**, *7*, 3906–3909.
- [136] X. Xing, B. Yoon, U. Landman, J. H. Parks, *Physical Review B* **2006**, *74*, 165423.
- [137] W. Zhang, Z. Li, Y. Luo, J. Yang, *The Journal of chemical physics* **2008**, *129*, 134708.
- [138] F. Meunier, J. Breen, V. Zuzaniuk, M. Olsson, J. Ross, *Journal of Catalysis* **1999**, *187*, 493–505.
- [139] H. He, Y. Yu, *Catalysis Today* **2005**, *100*, 37–47.
- [140] S. Satokawa, *Chemistry Letters* **2000**, *29*, 294–295.
- [141] J. P. Breen, R. Burch, C. Hardacre, C. J. Hill, *The Journal of Physical Chemistry B* **2005**, *109*, 4805–4807.
- [142] J. Ma, X. Cao, H. Liu, B. Yin, X. Xing, *Physical Chemistry Chemical Physics* **2016**, *18*, 12819–12827.
- [143] H. Kannisto, H. H. Ingelsten, M. Skoglundh, *Journal of Molecular Catalysis A: Chemical* **2009**, *302*, 86–96.
- [144] V. E. Matulis, D. M. Palagin, A. S. Mazheika, O. A. Ivashkevich, *Computational and Theoretical Chemistry* **2011**, *963*, 422–426.
- [145] H. Grönbeck, A. Hellman, A. Gavrin, *The Journal of Physical Chemistry A* **2007**, *111*, 6062–6067.
- [146] J. Hagen, L. D. Socaciu-Siebert, J. Le Roux, D. Popolan, S. Vajda, T. M. Bernhardt, L. Wöste, *International Journal of Mass Spectrometry* **2007**, *261*, 152–158.
- [147] F. Illas, J. Ricart, M. Fernández-García, *The Journal of chemical physics* **1996**, *104*, 5647–5656.
- [148] S. Haq, A. Carew, R. Raval, *Journal of Catalysis* **2004**, *221*, 204–212.
- [149] A. Balkenende, O. Gijzeman, J. Geus, *Applied surface science* **1989**, *37*, 189–200.
- [150] M.-Y. Yen, J.-J. Ho, *Chemical Physics* **2010**, *373*, 300–306.
- [151] S. González, C. Sousa, F. Illas, *Journal of Catalysis* **2006**, *239*, 431–440.
- [152] W. A. Brown, D. A. King, NO chemisorption and reactions on metal surfaces: a new perspective, **2000**.
- [153] J. Wendelken, *Applications of Surface Science* **1982**, *11*, 172–185.
- [154] P. Dumas, M. Suhren, Y. Chabal, C. Hirschmugl, G. Williams, *Surface science* **1997**, *371*, 200–212.

- [155] G. Gruzalski, D. Zehner, J. Wendelken, R. Hathcock, *Surface Science* **1985**, *151*, 430–446.
- [156] G. Gruzalski, D. Zehner, J. Wendelken, *Surface science* **1984**, *147*, L623–L629.
- [157] G. Gruzalski, D. Zehner, J. Wendelken, *Surface Science* **1985**, *159*, 353–368.
- [158] J. Wendelken, PhD thesis, AVS, **1982**.
- [159] S. Hirabayashi, M. Ichihashi, *The Journal of Physical Chemistry A* **2014**, *118*, 1761–1768.
- [160] L. Holmgren, M. Andersson, A. Rosén, *Chemical physics letters* **1998**, *296*, 167–172.
- [161] P. B. Balbuena, P. A. Derosa, J. M. Seminario, *The Journal of Physical Chemistry B* **1999**, *103*, 2830–2840.
- [162] C. Lacaze-Dufaure, C. Blanc, G. Mankowski, C. Mijoule, *Surface science* **2007**, *601*, 1544–1553.
- [163] M. Planck, *Annalen der Physik* **1901**, *309*, 553–563.
- [164] M. Born, W. Heisenberg, P. Jordan, *Zeitschrift für Physik* **1926**, *35*, 557–615.
- [165] E. Schrödinger, *Physical Review* **1926**, *28*, 1049–1070.
- [166] A. Szabo, N. Ostlund, *Modern Quantum Chemistry: Introduction to Advanced Electronic Structure Theory*, 1st, Dover Publication, INC., Mineola, New York, **1996**.
- [167] S. Chelkowski, T. Zuo, O. Atabek, A. D. Bandrauk, *Physical Review A* **1995**, *52*, 2977–2983.
- [168] M. Born, R. Oppenheimer, *Annalen der Physik* **1927**, *389*, 457–484.
- [169] J. C. Slater, *Physical Review* **1929**, *34*, 1293–1322.
- [170] V. Fock, *Zeitschrift für Physik* **1930**, *61*, 126–148.
- [171] I. Levine, *Quantum Chemistry*, 5th, Prentice Hall: Upper Saddle River, NJ, **2000**.
- [172] J. Kobus, *Advances in Quantum Chemistry, Vol. 28*, 1st, Academic Press, **1997**.
- [173] C. Roothaan, *Reviews of Modern Physics* **1951**, *23*, 69–89.
- [174] G. Hall, *Proceedings of the Royal Society A* **1951**, *205*, 541–552.
- [175] P. Löwdin, *Advances in Chemical Physics* **1959**, *2*, 207.
- [176] E. Schrödinger, *Annalen Der Physik* **1926**, *80*, 437–490.
- [177] C Møller, M. Plesset, *Physical Review* **1934**, *46*, 618–622.
- [178] J. Slater, *Physical Review* **1929**, *34*, 1293–1322.
- [179] E. Condon, *Physical Review* **1930**, *36*, 1121–1133.

- [180] O. Sinanoglu, *The Journal of Chemical Physics* **1962**, *36*, 706.
- [181] R. Nesbet, *Physical Review* **1968**, *175*, 2.
- [182] J. Čížek, *The Journal of Chemical Physics* **1966**, *45*, 4256–4266.
- [183] J. Čížek, J. Paldus, *International Journal of Quantum Chemistry* **1971**, *5*, 359–379.
- [184] J. Paldus, J. Čížek, *Physical Review A* **1972**, *5*, 50–67.
- [185] J. Paldus, J. Čížek, B. Jeziorski, *The Journal of Chemical Physics* **1989**, *90*, 4356–4362.
- [186] R. Bartlett, G. Purvis, *International Journal of Quantum Chemistry* **1978**, *14*, 561–581.
- [187] G. Purvis, R. Bartlett, *The Journal of Chemical Physics* **1982**, *76*, 1910–1918.
- [188] R. Bartlett, *The Journal of Physical Chemistry* **1989**, *93*, 1697–1708.
- [189] J. Pople, R. Krishnan, H. Schlegel, J. Binkley, *International Journal of Quantum Chemistry* **1978**, *14*, 545–560.
- [190] T. Helgaker, P. Jorgensen, J. Olsen, *Molecular Electronic-Structure Theory*, 1st, John Wiley Sons Ltd, Chichester, England, **2000**.
- [191] J. Noga, R. Bartlett, *The Journal of chemical physics* **1987**, *86*, 7041–7050.
- [192] G. E. Scuseria, H. F. Schaefer III, *Chemical physics letters* **1988**, *152*, 382–386.
- [193] L. Lee, S. Kucharski, R. Bartlett, *The Journal of chemical physics* **1984**, *81*, 5906–5912.
- [194] M. Urban, J. Noga, S. Cole, R. Bartlett, *The Journal of chemical physics* **1985**, *83*, 4041–4046.
- [195] J. Noga, R. Bartlett, M. Urban, *Chemical physics letters* **1987**, *134*, 126–132.
- [196] J. Noga, R. Bartlett, *The Journal of chemical physics* **1987**, *86*, 7041–7050.
- [197] K. Raghavachari, G. W. Trucks, J. A. Pople, M. Head-Gordon, *Chemical Physics Letters* **1989**, *157*, 479–483.
- [198] J. J. Eriksen, K. Kristensen, T. Kjærgaard, P. Jørgensen, J. Gauss, *The Journal of Chemical Physics* **2014**, *140*, 064108.
- [199] H.-J. Werner, P. J. Knowles, G. Knizia, F. R. Manby, M. Schütz, et al., MOLPRO, version 2019.2, a package of ab initio programs, see, **2019**.
- [200] T. H. Dunning Jr, *The Journal of chemical physics* **1989**, *90*, 1007–1023.
- [201] D. E. Woon, T. H. Dunning Jr, *The Journal of chemical physics* **1993**, *98*, 1358–1371.

- [202] A. J. Varandas, *Annual review of physical chemistry* **2018**, *69*, 177–203.
- [203] D. Figgen, G. Rauhut, M. Dolg, H. Stoll, *Chemical physics* **2005**, *311*, 227–244.
- [204] K. A. Peterson, C. Puzzarini, *Theoretical Chemistry Accounts* **2005**, *114*, 283–296.
- [205] B. Liu, A. McLean, *The Journal of Chemical Physics* **1973**, *59*, 4557–4558.
- [206] J. Van Lenthe, R. Vos, J. Van Duijneveldt-Van De Rijdt, F. Van Duijneveldt, *Chemical physics letters* **1988**, *143*, 435–438.
- [207] S. F. Boys, F. d. Bernardi, *Molecular Physics* **1970**, *19*, 553–566.
- [208] R. M. Richard, B. W. Bakr, C. D. Sherrill, *Journal of chemical theory and computation* **2018**, *14*, 2386–2400.
- [209] E. P. Wigner, E. E. Witmer.
- [210] K. Huber, G. Hertzberg, *Molecular Spectra and Molecular Structure IV. constants of Diatomic Molecules, Vol. 4*, **1979**, pp. 466–689.
- [211] J. C. Ehrhardt, S. P. Davis, *JOSA* **1971**, *61*, 1342–1349.
- [212] P. Pyykko, J. P. Desclaux, *Accounts of Chemical Research* **1979**, *12*, 276–281.
- [213] K. MacAdam, S. Dyubko, V. Efremov, V. Gerasimov, A. Kutsenko, *Journal of Physics B: Atomic Molecular and Optical Physics* **2009**, *42*, 165009.
- [214] H.-P. Looock, L. M. Beaty, B. Simard, *Physical Review A* **1999**, *59*, 873.
- [215] S. Dyubko, V. Efremov, V. Gerasimov, K. MacAdam, *Journal of Physics B: Atomic Molecular and Optical Physics* **2005**, *38*, 1107.
- [216] P. H. Krupenie, The band spectrum of carbon monoxide, tech. rep., NATIONAL STANDARD REFERENCE DATA SYSTEM, **1966**.
- [217] Y. Kim, K Stephan, E Märk, T. Märk, *The Journal of Chemical Physics* **1981**, *74*, 6771–6776.
- [218] H Hotop, R. Bennett, W. Lineberger, *The Journal of Chemical Physics* **1973**, *58*, 2373–2378.
- [219] J. C. Rienstra-Kiracofe, G. S. Tschumper, H. F. Schaefer, S. Nandi, G. B. Ellison, *Chemical reviews* **2002**, *102*, 231–282.
- [220] K. M. Refaey, J. Franklin, *International Journal of Mass Spectrometry and Ion Physics* **1976**, *20*, 19–32.
- [221] M. J. Travers, D. C. Cowles, G. B. Ellison, *Chemical physics letters* **1989**, *164*, 449–455.
- [222] N. Bartlett, *Gold Bulletin* **1998**, *31*, 22–25.

-
- [223] B. Simard, P. A. Hackett, A. M. James, P. R. Langridge-Smith, *Chemical physics letters* **1991**, *186*, 415–422.
- [224] G. Bistoni, S. Rampino, N. Scafuri, G. Ciancaleoni, D. Zuccaccia, L. Belpassi, F. Tarantelli, *Chemical science* **2016**, *7*, 1174–1184.